

The Developing of Scientific Advances of Liquid Lens use the Concept STEM Education

N. Limphaiboon^{*} and P. Asanithi

Department of Physics, Faculty of Science, King Mongkut's University of technology Thonburi,
126 Pracha-Uttid Road, Bangmod, Bangkok, 10140 Thailand

*E-mail: corresponding_netnapha.phy@mail.kmutt.ac.th

Abstract

The objective of this research was to developing of scientific advances of liquid lens use the concept STEM education. The samples of this research were 40 grade 11 students at Ratanaratbunrung School. In this research, students can learn about the liquid lens by demonstrations and design the experimental apparatus for study a contact angle, a focal length and a magnification of the lens witch STEM education is a curriculum based on the idea of educating students in four specific disciplines science, technology, engineering and mathematics. The measurement and evaluation is the test by scanning QR-code from Google Form program. This research found that the class average normalized gain was high gain and the learner can design base for placing this glass slide on the camera of a mobile phone, this will enhance the imaging ability of the camera to similar to an optical microscope. Furthermore, this research can integrated scientific knowledge of lens to solving problem in daily life.

Keywords : Liquid Lens, STEM education

Introduction

STEM is a curriculum based on the idea of educating students in four specific discipline-science, technology, engineering and mathematics and appropriated to student in 21st century skill to solving problem in daily life. [1] This research is to develop scientific idea and learning methods based on the STEM education to solve the problem of taking a photograph of tiny object with liquid lens. This research is continued research idea from glass lens to other lens it's made from liquid lens to study the relation between contact angle of droplet, magnification, focal length with droplet volume .Droplet is on glass slide (hydrophilic) and coated glasses with leather spray (hydrophobic). It could form to different liquid lens and took the highest

magnification lens to integrated mobile phone as a microscope. Evaluation is measured by Normalized gain by pretest and posttest.

Materials and Methods

The samples of this research were 40 students (grade 11) at Ratanaratbunrung School. They were participated for developing scientific idea about liquid lens based on the concept of STEM education, including science, technology, engineering and mathematics.

Science Literacy: to understand scientific content and having scientific skill

Mathematics Literacy: to able critical thinking and can using, applying mathematics method to construct, explain and predict phenomenon.

Technology Literacy: Understanding and ability to use, manage, and access to technology

Engineering Literacy: Engineering design process to solve creative design work. [2]

Strategy of learning is as follows

Teacher leads student to learn by scanning QR Code to answer the 5 questions (pre-test) from Google form application program. Then, students answer the questions and do activity learning.

Science: To observe liquid droplet on different surfaces of leaves, having different characteristic of droplet and the droplet can enlarge leaf structure to perform as a lens. Controlled different volume was constructed with micropipettes on two surfaces, one is hydrophilic surface and another spraying leather wax on the glass slide as hydrophobic surface. These glass slides were laid on the arrow pictures to study the lens property.

Technology: To study the relationship between contact angle, magnification and focal length on volume of droplet that drop on hydrophilic and hydrophobic surface by Image J Program.

Mathematics: To study the relationship with application of mathematics concepts to make equation of relationship between contact angle, the high and radius of droplet to compare with contact angle from Image J. Then, data to make chart of relation between contact angle, the high and radius of droplet.

Engineering: To choose glass surface which upper surface having highest magnification and placing this glass on the camera of a mobile phone, this will enhance the imaging ability of the camera to similar to an optical microscope. To construct basement and to solve shaking-hand problem when taking a photo.

When the students have learned completely 4 literacies, the student presented using the mobile phone as microscope and do the post-test to evaluate normalized gain [3] from the relation of equation.

$$\langle g \rangle = \frac{(\%Post - test) - (\%Pre - test)}{(100\%) - (\%Pre - test)}$$

$\langle g \rangle$ is Normalized gain

$\%Pre - test$ is final (posttest) class percentage averages.

$\%Post - test$ is initial (pretest) class percentage averages.

And divided the Normalized gain into three levels:

High gain at $\langle g \rangle \geq 0.7$

Medium gain at $0.7 < \langle g \rangle \leq 0.3$

Low gain at $\langle g \rangle < 0.3$

Results and Discussion

1. Scanning QR code to answer the 5 questions from Google form program



Figure 1 QR-Code of the pre-test

The pretest answer as followed

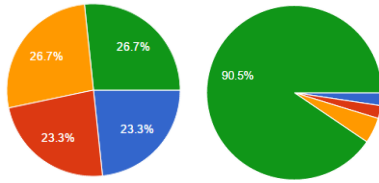
1. If students want to examine the hypothesis "The contact angle of water droplets on the surface" which choice is the best design experiments using surface leaves.

1) Drop the same volume on the same surface of the leaves. Observe the contact angle occurred.

2) Drop the different volumes of water droplets on the same surface of the leaves. Observe the contact angle occurred.

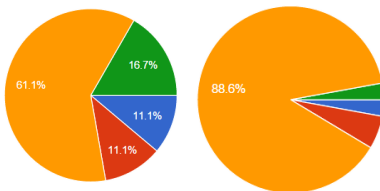
3) Drop the different volumes on the different surfaces of leaves. Observe the contact angle occurred.

4) Drop the same volume of water to different types of leaves surface. Observe the contact angle occurred.



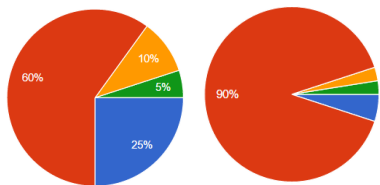
2. Consider the following statement which item is correct?

- 1) Contact angle on the surface of less than 90 degrees is called hydrophobic surface.
- 2) Contact angle on the surface of greater than 90 degrees is called hydrophilic surface.
- 3) Contact angle of lotus leaf surface, which is greater than 150 degrees, is called superhydrophobic surface
- 4) The surface leaves with zero contact angle is called amphiphilic surface.



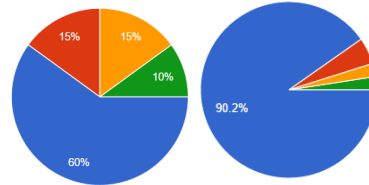
3. What is a kind of lens when dropping water onto any surface?

- 1) Convex lens
- 2) Plano convex lens
- 3) Concave lens
- 4) Plano concave lenses



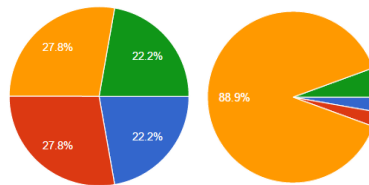
4. What is the image of an object, formed by a lens of water droplet?

- 1) Enlarged object size and the image is an upright virtual image
- 2) Enlarged object size and the image is an upright real image
- 3) Enlarged object size and the image is an inverted virtual image
- 4) Enlarged object size and the image is an inverted real image



5. When the volume is changed which choice indicate the relationship between contact angle, focal length and magnification of the lens?

- 1) Contact angle and focal length are increased but magnification is decreased
- 2) Contact angle, focal length and magnification are increased
- 3) Contact angle and magnification are decreased but focal length is increased.
- 4) Contact angle and focal length are decreased but magnification is increased



2. As science literacy activity, the student studied characteristic of droplet on different leaves. They can get the new knowledge of contact angle of droplet as table

Table 1 Possible contact angle on the surface. [4]

contact angle (θ) ° degree	Surface state
0	Super Hydrophilic
$0 < \theta < 90$	Hydrophilic
90	Amphiphilic
$90 < \theta < 150$	Hydrophobic
$\theta \geq 150$	Super Hydrophobic

The student can do development of scientific advances of convex lens and finding calculate magnification and focal length as equation.

$$M = \frac{y'}{y} \quad (1)$$

$$f = \frac{M}{M-1} S \quad (2)$$

- M is magnification of the image
- y is height of the object
- y' is height of the image
- f is focal length of the lens
- S is object distance

This result can be adapted to form of droplet on glass slide that was plano convex lens as picture. Contact angle, magnification and focal length can get by Image J on technology literacy (T)



Figure 1 The characteristics of droplets are plano convex surfaces on the hydrophilic and hydrophobic surfaces.

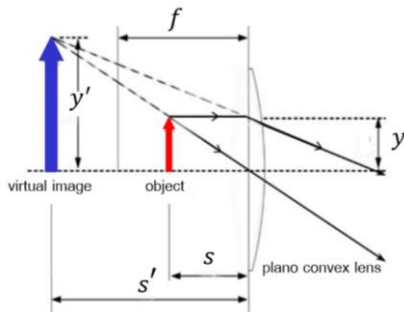
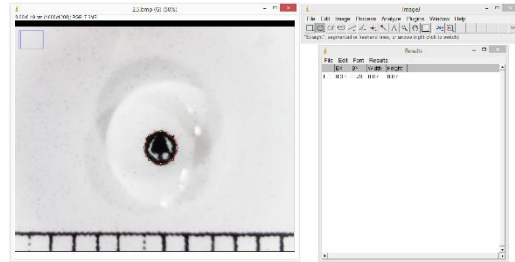
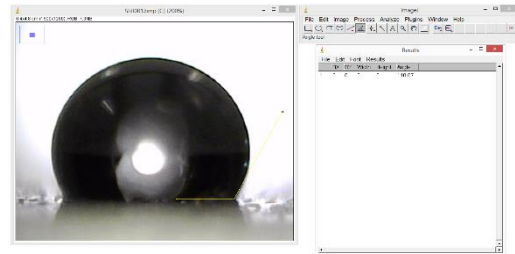


Figure 2 Optical path of the lens [5]

3. As Technology literacy activity, the student can use Image J to calculate contact angle, lens magnification as figure.



(A) Measure the size of the image.



(B) Measuring the contact angle of water droplets.

Figure 3 Using Image J program.

The contact angle of the glass slide is less than 90° is called hydrophilic surface and the contact angle of the glass sprayed by a water-repellent spray for a leather has a contact angle more than 90° called hydrophobic. The image magnification of hydrophobic glass surface is higher than that of the hydrophilic glass. On the other hand, the hydrophobic surface has a focal length less than hydrophilic surface.

4. As Mathematics literacy activity, the student can find the relationship of contact angle, the high droplet and radius of droplet as figure

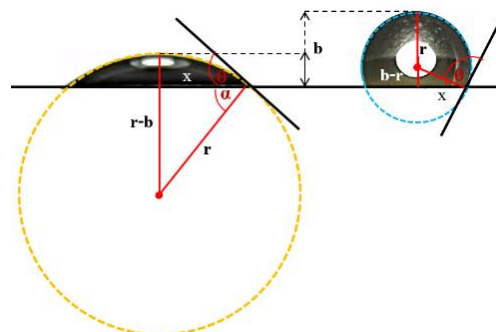


Figure 4 The relationship of contact angle,

The high droplet and radius of droplet

$$\theta = 90^\circ + \tan^{-1} \left(\frac{b-r}{\sqrt{2rb-b^2}} \right)$$

$$\theta = 90^\circ + \tan^{-1} \left(\frac{b-r}{\sqrt{2rb-b^2}} \right)$$

As program Image J plot graph to compare experimental and calculate as Figure 5.

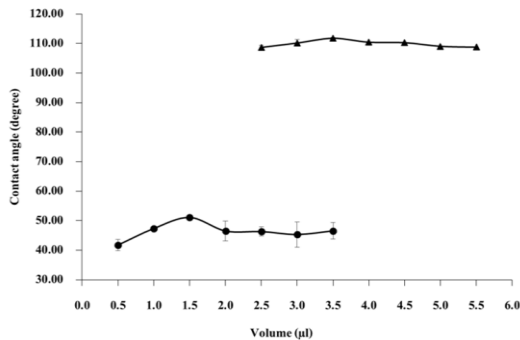


Figure 5 Contact angle of droplet

5. As Engineering literacy activity, Liquid lens on hydrophobic surface was take place on basement created by student that could be take a photo tiny object by choosing the highest magnification was 2.6x. This results found that the set of experimental can integrated with mobile phone and used as microscope.



Figure 6 The picture from the liquid lens by mobile phone.



Figure 7 Presentations using a liquid lens with a mobile phone on the base object to study.

Pretest and posttest showed normalized gain as in Figure 8. This research found that normalized gain was high and medium gain. This result showed that instruction can develop scientific thinking from liquid lens along with STEM education.

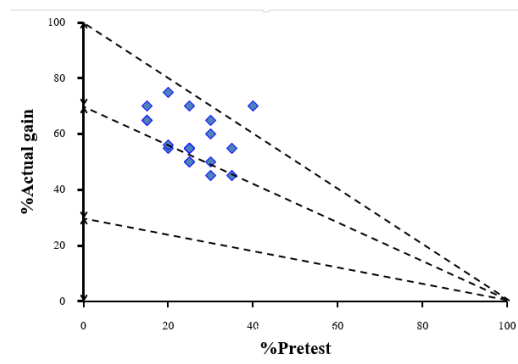


Figure 8 Normalized Gain

Conclusions

The development of scientific learning kits about liquid lens along with STEM has been successful. The students have been educated in four specific discipline-science, technology, engineering and mathematics. The students understand the concepts of liquid lens. This research showed that the students have high normalized gain and they could integrate these lens with a mobile phone and used as a microscope.

Acknowledgments

This researcher would like to thank the lecturers at the Department of Physics, Faculty of science, KMUTT, Thailand and thank the scholarship from the PSMT and IPST Thailand.

References

- [1] IPST, 2014. "STEM EDUCATION". **IPST Magazine**. Volume 186. 3-9.
- [2] IPST. "STEM EDUCATION: The 21st Century Learning". Available: www.stemedthailand.org [2016, May 24]
- [3] Hake, R.R., 2002, "Relationship of Individual Student Normalized Learning Gains in Mechanics with Gender, High-School Physics, and Pretest Scores on Mathematics and Spatial Visualization", Available : www.researchgate.net/publication/237457456. [2016, April 10].
- [4] Rupp, F., et al., 2014, "A Review on the Wettability of Dental Implant Surface I: Theoretical and Experimental Aspects", **Acta Biomaterialia**, [Electronic], Vol.10, pp. 2896-2898, Available : Elsevier / Science Direct [2015, April 20].
- [5] Liu, C-X., Park, J. and Choi, J-W., 2008, "A Planar Lens Based on the Electrowetting of Two Immiscible Liquids", **Journal of Micromechanics and Microengineering**, Vol.18, pp.7.

Elimination of Pinned Spiral Waves by on-off Formed Electric Field in Excitable Media

P. Suwannakrua*, N. Kumchaiseemak, J. Kanchanawarin, M. Sutthiopad and C. Luengviriya

Department of Physics, Kasetsart University, 50 Phaholyothin Road, Jatujak, Bangkok 10900, Thailand

E-mail: g5714401174@ku.ac.th

Abstract

We present numerical simulations on a release of spiral waves pinned to an unexcitable circular obstacle in a two-dimensional excitable medium using the Oregonator model. For a given obstacle, a constant electric field with amplitude stronger than a critical value E_{unpin} causes a pinned spiral wave to drift away from the obstacle. Our results show that the energy applied to unpin the spiral wave can be reduced by using a time varying electric field. For an on-off formed electric field with E_{unpin} and an appropriate on-off period, the applied energy is decreased to 35% of constant electric field.

Keywords: Two-dimensional obstacle, Unpinning by electrical field, On-off period

Introduction

Spiral waves evolve in various excitable media, e.g., during CO-oxidation on a platinum surface [1], cell aggregation in slime mold colonies[2], electrical wave propagation in cardiac tissues [3], and concentration waves in the Belousov-Zhabotinsky (BZ) reaction [4,5]. Such spiral patterns of electrical excitation in the heart are causing certain types of cardiac arrhythmia, which can lead to sudden cardiac death. Elimination of spiral waves can be done by an application of electric field to drift and hit the boundary of the medium. However, spiral waves in cardiac tissues are often stabilized by being pinned to obstacles (e.g., veins or scars) [3].

Dynamics of the spiral waves in excitable media are intensively studied by using the Oregonator model [6]. Application of a constant electric field can unpin the spiral waves [7]. The electric field must be sufficiently strong and applied for a long duration. This means that a high electrical energy is applied to the medium which is possibly damaged. In this study, we perform simulations on unpinning of spiral wave using

an alternating electric field to reduce the energy which is applied to the medium.

Materials and Methods

In our simulations, the Oregonator model is used to describe the dynamics of the activator u and the inhibitor v in excitable media. The advection terms for both u and v account for the electric field E applied in x -direction:

$$\frac{\partial u}{\partial t} = \frac{1}{\varepsilon} \left(u - u^2 - fv \frac{u-q}{u+q} \right) + D_u \nabla^2 u - M_u E \frac{\partial u}{\partial x} \quad (1),$$

$$\frac{\partial v}{\partial t} = u - v + D_v \nabla^2 v - M_v E \frac{\partial v}{\partial x} \quad (2)$$

The system supported a spiral wave rotating rigidly around a circular core when the parameters [8-9] were $\varepsilon = 0.01$, $q = 0.002$, $f = 1.4$, the diffusion coefficients $D_u = 1.0$ and $D_v = 0.6$, and the ionic mobilities $M_u = -1.0$ and $M_v = 2.0$. We use an explicit Euler method with a 9-point approximation of the two-

dimensional Laplacian operator and a centered-space approximation of the gradient term. The uniform grid space $\Delta x = \Delta y = 0.1$ system unit (s.u.) and the time step $\Delta t = 0.003$ time unit (t.u.) are chosen as required for numerical stability ($\Delta t \leq (3/8)(\Delta x)^2 [10]$). The dimensionless size of the system is 40×40 s.u. (400×400 grid points). A completely unexcitable circular area is put as the obstacle and the boundaries of both the obstacle and the medium have no-flux conditions. To create a spiral wave, we excite a planar wave by setting a 5-grid-point strip at an edge of the medium to an excited state (e.g., $u = 1.0$ and $v = 0$ for $0.0 \leq x \leq 0.5$) and the wave front is allowed to propagate into the middle of the medium, before half of the medium is reset to an excitable state (e.g., $u = 0$ and $v = 0$ for $0.0 \leq y \leq 10.0$) leading to a free-end wave front, which subsequently curls to form a rotating spiral wave. To apply alternating electric field, the parameter E is set on-off during the simulation.

Results and Discussion

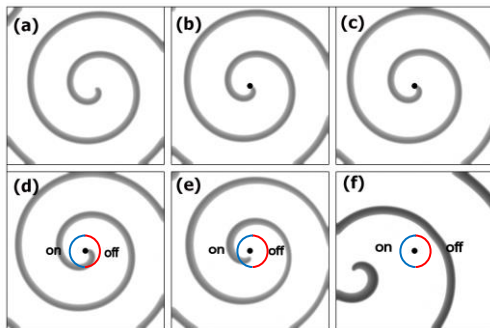


Figure 1 Spiral waves in the Oregonator model: (a) a free spiral wave (no obstacle, spiral core diameter s.u.) and spiral wave pinned to (b) a circle with diameter of 1.5 s.u., (c) pinned spiral wave adjusts itself to have longer wave length, (d) Turn off electrical current E_{unpin} and spiral wave is on the negative electrode, (e) apply electric field E_{unpin} and spiral tip is unpinned from obstacle, (f) released spiral wave move away from obstacle until it hit boundary.

Figure 1(a) shows a free spiral wave in this simulation. The obstacle with 1.5 s.u. diameter is added (Figure 1(b)) in the middle of the system so that the pinned spiral wave rotates around the obstacle and adapted to the obstacle (Figure 1(c)). The wave period of the pinned spiral wave is about 1.86 t.u.

Then we apply a constant electric field to unpin the spiral wave from the obstacle with minimal electric field (E_{unpin}). For the given circular obstacle, we get $E_{\text{unpin}} = 0.69$. We take this E_{unpin} as the appropriate amplitude of the alternating applied electric field in the next step.

To reduce the applied energy for unpinning the spiral wave, we use an on-off electric field with different percentages of on-off durations, for example 70-30 means turn on 70% and turn off 30%. We test electric field with 70-30, 65-35, 60-40, 55-45, 50-50, 45-55, 40-60, 35-65, 30-70. When electric field is on $\geq 35\%$ the spiral wave is successfully unpinned from the obstacle but the unpinning fails in the case of 30-70. Therefore, the lowest energy for unpinning is 35% of the constant electric field application.

Conclusion

We present a simulation study of unpinning spiral wave using an on-off formed electric field in the Oregonator model for reducing the applied energy. The minimal energy is reduced to 35% of the constant electric field. In the future, we will study unpinning of spiral in different situations, e.g., obstacle size and other forms of alternating electric field.

Acknowledgments

We thank the Department of Physics, Faculty of Science, the Research and Development Institute (KURDI), the Center for Advanced Studies of Industrial Technology, and the Graduate School, Kasetsart University; and the Office of the Higher Education Commission and King Mongkut's University

of Technology North Bangkok (contract no. KMUTNB-NRU-58-03) for financial support.

References

- [1] S. Nettesheim, A. von Oertzen, H. H. Rotermund, and G. Ertl, **J. Chem. Phys.**, 1993, 98, 9977.
- [2] F. Siegert and C.J. Weijer, **J. Cell Sci**, 1989, 93, 325.
- [3] J. M. Davidenko, A. M. Pertsov, R. Salomonz, W. Baxter, and J. Jalife, **Nature**, 1992, 335, 349.
- [4] A. T. Winfree, **Science**, 1972, 175, 634.
- [5] A. T. Winfree, **Science**, 1973, 181, 937.
- [6] J. Luengviriya, M. Sutthiopad, and M. Phantu.
“ Influence of excitability on unpinning and termination of spiral waves, **Phys. Rev. E** 90, 052919 (2014).
- [7] W. Jahnke, W.E. Skaggs, and A.T. “Winfree. Chemical vortex dynamics in the Belousov-Zhabotinsky reaction and in the two-variable Oregonator model, **J. Phys. Chem.**, 93:740-749, 1989.
- [8] B. Schmidt and S.C. Müller. “Forced parallel drift of spiral waves in the Belousov-Zhabotinsky reaction, **Phys. Rev. E**, 55:4390-4393, 1997.
- [9] M. Dowle, R. M. Mantel, and D. Barkley. “Fast simulations of waves in three-dimensional excitable media, **Int. J. Bif. Chaos**, 7:2529, 1997.
- [10] R.J. Field and R.M. Noyes. “Oscillations in chemical systems. IV. Limit cycle behavior in a model of a real chemical reaction, **J. Chem. Phys.**, 60:1877-1884, 1974.

Stimulation and Control of Wave Trains in the Belousov-Zhabotinsky Reaction

P. Srithamma¹, P. Wungmool¹, N. Kumchaiseemak¹, J. Luengviriya^{2,3} and C. Luengviriya^{1*}

¹Department of Physics, Kasetsart University, 50 Phaholyothin Road, Jatujak, Bangkok 10900, Thailand.

²Department of Industrial Physics and Medical Instrumentation, King Mongkut's University of Technology North Bangkok, 1518 Pibulsongkram Road, Bangkok 10800, Thailand.

³Lasers and Optics Research Group, King Mongkut's University of Technology North Bangkok, 1518 Pibulsongkram Road, Bangkok 10800, Thailand.

*E-mail: fscicyl@ku.ac.th

Abstract

Spiral waves are an origin of the most dangerous cardiac arrhythmia leading to fibrillation and sudden death. It is shown that a high-frequency wave train can induce a drift of free spiral waves until they annihilate at the boundary. Elimination of spiral waves by using wave train is also demonstrated in the Belousov-Zhabotinsky (BZ) reaction but lack of the control of the wave period. We present a method to generate and control a train of excitation waves in the BZ reaction. A droplet of 2.5M sulfuric acid (10 μ l) was used as the wave source while the wave period can be controlled by setting the local temperature at the source location. When the local temperature is increased from 22 to 37°C, the wave period decreases from 4.9 to 2.75 minutes when the bulk temperature is 22°C.

Keywords: Spiral wave, Wave train, Local temperature

Introduction

Spiral Waves are special propagating structures in excitable media, such as waves of action potential in cardiac tissues [1], spreading depression in chicken retina [2], cAMP-waves in a colony of the slime mold *Dictyostelium Discoideum* [3]. and concentration wave in the Belousov-Zhabotinsky (BZ) reaction [4,5].

Spiral waves in the heart tissues are the origin of ventricular tachycardia [6] and fibrillation which potentially leading to sudden cardiac death. Cardioversion shocks for eliminating spiral waves from the heart are applications of high electrical voltage. The above method results in damage of the cardiac tissues. To avoid this problem, many studies have been performed to eliminate the spiral waves with low voltage, e.g., applications of wave trains. It is found that high-

frequency wave trains induce drift of spiral waves to the boundary and the spiral waves are annihilated when the spiral hit the boundary [7,8,9].

Due to the convenience of its preparation, the BZ reaction is the most used medium for studying the propagation of spiral waves. Recently, elimination of spiral waves using wave trains have been studied extensively in simulations but rarely in the BZ experiments probably due to lack of controlling of wave train frequency in the BZ experiments [7,8,9]. In this article, we present a method for controlling the frequency of the wave trains.

Materials and Methods

Our BZ reaction is composed of NaBrO₃, malonic acid (MA), H₂SO₄, and ferroin, from Merck. We add a

surfactant, sodium dodecyl sulfate (SDS, from Fluka), to reduce the production of CO_2 bubbles, which disturb waves in the BZ reaction. We prepare stock solutions of NaBrO_3 (1 M), MA (1 M), and SDS (1 M) by dissolving powder in deionized water (conductivity of $\sim 0.056 \mu\text{Scm}^{-1}$), whereas stock solutions of H_2SO_4 (2.5 M) and ferroin (25 mM) are commercially available. Appropriate volumes of the stock solutions are mixed and diluted in deionized water to form BZ solutions with initial concentrations $[\text{NaBrO}_3] = 50 \text{ mM}$, $[\text{MA}] = 50 \text{ mM}$, $[\text{ferroin}] = 0.625 \text{ mM}$, and $[\text{SDS}] = 0.05 \text{ mM}$ and $[\text{H}_2\text{SO}_4] = 200 \text{ mM}$. To prevent hydrodynamic perturbations, 0.5% agar is added to the solutions.

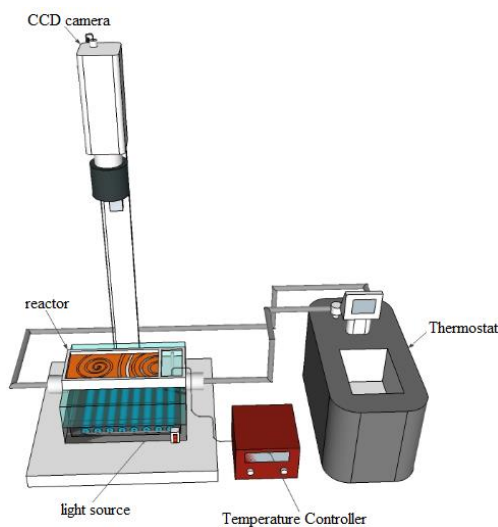


Figure 1 Experimental setup.

The experimental set up is shown in Figure 1. The dimensions of the reactor $100 \times 50 \times 10 \text{ mm}^3$ (the top plane area $100 \times 50 \text{ mm}^2$) and the bulk temperature is controlled by a thermostat at $22 \pm 1^\circ\text{C}$. The reactor is placed between the light source and the camera to record the images of the medium every second with a resolution of 10 pixelm^{-1} . We generate wave trains by dropping $10 \mu\text{l}$ of 2.5 M H_2SO_4 close to an inner wall (the right wall of the reactor). The wave period is controlled by setting the local temperature via a small water bath adjacent to the right wall of the reactor.

Results and Discussion

This Figure 2 shows an example of wave train generation for the local temperature of 30°C . After poured into the reactor, the BZ reaction is homogenous (Figure 2a). A few minutes after H_2SO_4 droplet is applied at the right wall, wave fronts emerge and propagate outward the source of excitation (figure 2b). Further wave fronts are periodically generated so that the medium is subsequently filled by the train of wave fronts within half an hour (figure 2c and 2d). The wave period is about 3.92 min.

We control the wave period via the local temperatures. As shown in Figure 3, the wave period monotonously decrease while the local temperature is increased. When the local temperatures is set at $22\text{--}37^\circ\text{C}$ the generated wave train has a period between 4.90–2.75 min. We have experimented at a higher local temperature of 40°C but the wave fronts breakup as shown in figure 4. The front breakup may be caused high spatial gradient of temperature around the wave source.

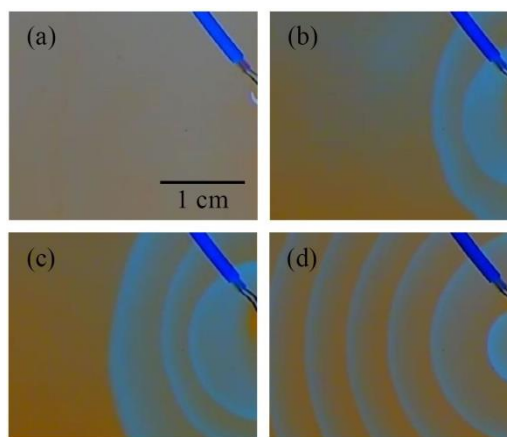


Figure 2 Propagating wave train in the BZ.

reaction. (a) The reaction is quiescent at the beginning, Curved wave fronts are periodically generated after an application of H_2SO_4 droplet (b) 7 min, (c) 14 min and (d) 24 min. The blue cable is a thermocouple added for local temperature measurement.

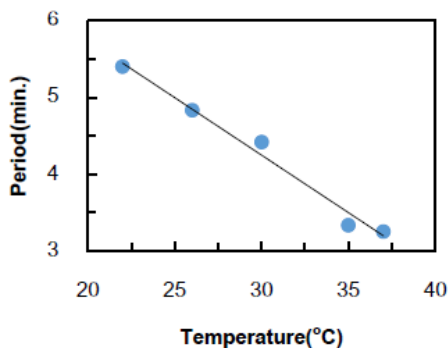


Figure 3 Period of the wave train vs. local temperature.

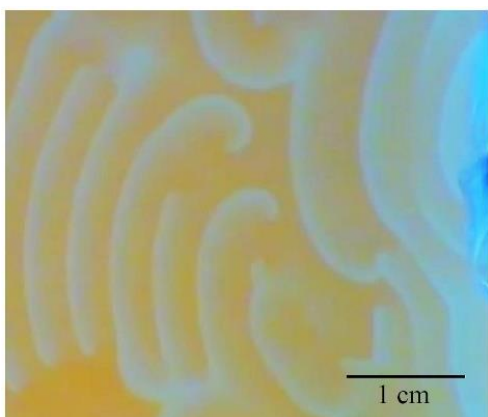


Figure 4 Breakup of wave fronts at local temperature of 40°C.

Conclusions

We have presented a method to generate wave train and control the wave period in the BZ reaction. While the bulk temperature is kept constant, the local temperature is increased and the wave period decreased. The generation of wave train is limited at the local temperature less than 40°C due to the wave front break up at high local temperature. The generating method presented here can be utilized in experiments of spiral wave elimination by wave train.

Acknowledgments

We thank the Department of Physics, Faculty of Science, the Research and Development Institute (KURDI), the Center for Advanced Studies of Industrial

Technology, and the Graduate School, Kasetsart University; and the Office of the Higher Education Commission and King Mongkut's University of Technology North Bangkok (contract no. KMUTNB-NRU-58-03) for financial support.

References

- [1] J.M. Davidenko, A.M. Pertsov, R. Salomonz, W. Baxter, and J. Jalife, 1992, Stationary and drifting spiral waves of excitation in isolated cardiac muscle, *Nature*, Vol. 355, pp. 349-351
- [2] M.A. Dahlem and S.C. Müller, 1997, Self-induced plitting of spiral-shaped spreading depression waves in chicken retina, *Exp Brain Res*, Vol. 115, pp. 319-324
- [3] F. Siegert and C.J. Weijer, 1989, Digital image processing of optical density wave propagation in *Dictyostelium discoideum* and analysis of the effects of caffeine and ammonia, *J. Cell Sci*, Vol. 93, pp. 325-335
- [4] A. T. Winfree, 1972, Spiral waves of chemical activity, *Science*, Vol. 175, pp. 634-636
- [5] S.C. Müller, T. Plesser and B. Hess, 1985, The structure of the core of spiral wave in the Belousov-Zhabotinsky reagent, *Science*, Vol. 230, pp. 661-663
- [6] E.M. Cherry and F.H. Fenton, 2008, Visualization of spiral and scroll waves in simulated and experimental cardiac tissue, *New J. Phys*, Vol. 10, pp. 125016
- [7] M. Tanaka, A. Isomura, M. Hörning, H. Kitahata and K. Agladze, 2009, Unpinning of a spiral wave anchored around a circular obstacle by an external wave train: Common aspects of a chemical reaction and cardiomyocyte tissue, *Chaos*, Vol. 19, pp. 043111-043115.
- [8] S. Dutta and O. Steinbock, 2011, Spiral defect drift in the wave fields of multiple excitation patterns, *Phys. Rev. E*, Vol. 83, pp. 0562131-0562138.
- [9] M. Tanaka, M. Hörning, H. Kitahata and K. Yoshikawa, 2015, Elimination of a spiral wave pinned at an obstacle by a train of plane waves: Effect of diffusion between obstacles and surrounding media, *Chaos*, Vol. 25, pp. 1031271-1031279

Design and Construction of a Thermoelectric Generator by Using Solar Thermal Energy

W. Piwbang, J. Laopaiboon and S. Pencharee*

Department of Physics, Faculty of Science, Ubon Ratchathani University, 34190, Ubon Ratchathani, Thailand

*E-mail: Somkid.p@ubu.ac.th

Abstract

This research aimed to design and construct a thermoelectric generator by using solar energy as a heat source, a parabolic dishes having diameter 1.5 m. with a focal length 0.5 m. is used to concentrate the solar radiation. Solar thermal energy is absorbed by a sheet of aluminum on focal zone. The hot side of thermoelectric generator (TEG) device was mounted on an aluminum sheet, heat sink with dimensions 120x200x50 mm. and cooling fan were installing on the cold side of TEG. Our experiment on 28th and 29th march 2016 at Department of Physics, Faculty of Science, Ubon Ratchathani University on the north east of Thailand. Perform collection of the data from 8:30 a.m. to 4:00 p.m. From the result of experiment, at 12:30 on 28th March maximum temperature from solar radiation heat on hot side of TEG is 515 K, when intensity of sun is 1092 w/m^2 and the maximum power output is 6.28 W.

Keywords: Thermoelectric generator, Parabolic dishes, Solar thermal energy

Introduction

Nowadays, electricity energy is important in everyday life. Currently, electricity energy are produced mostly from fossil fuels, but the uncertainty of the amount and reliability of the fossil fuel used in the production of energy. Researchers have developed a new kind of method for produce electricity. The production of electricity from alternative or renewable energy are the interesting way. Alternative energy is energy that occurs in nature, such as solar, wind, water and geothermal. Thailand has a relatively high solar intensity. Researcher has been conducted to bring solar energy utilization. The solar energy can be very practical, the production of electricity by solar cells, used for drying agricultural products, the production of hot water and etc. Collecting solar thermal energy used to generate electricity in a way that can be done.

The TEG are device which convert heat energy to electrical energy. [1-8] The Seebeck effect that a potential difference proportional to the temperature difference is set up across the two faces of TEG which are hot side and cold side. The heat from the solar are applied to hot side of thermoelectric module and heat sink added to the other side. A solar concentration such as parabolic dish, parabolic troughs and power tower are applied for increase temperature of solar heater [1,3]. In this work, parabolic dish, HZ-9 and aluminum heat sink were used for TEG module and performances were investigated.

Experimental Details

The temperature difference is achieved by placing the hot side of the TEG at the focus of a parabolic dish

while the other side is kept at a lower temperature with cold air fan passing over it.

It consists of a parabolic dish collector, a flat aluminum heat receiver plate attached with thermoelectric modules on its focal plane. Thermoelectric modules are connected electrically in series and thermally in parallel between the receiver plate and the bottom surface of the heat sink that acts as heat exchanger. The hot side of the thermoelectric module is the top surface of the receiver plate and its cold side is the bottom surface of the heat sink. The parabolic dish collector is tracked manually in the east-west direction to absorb the solar beam radiation on the bottom of the receiver system. The system schematic is shown in Figure 1.

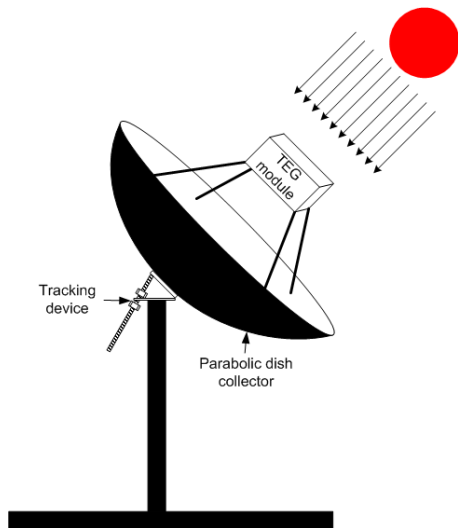


Figure 1 Arrangement of solar parabolic dish system

The reflector surface of parabolic dish concentration was made by 4x4 cm rectangle mirror tags to the parabolic dish. The mirror was used for reflect the solar radiation to focal zone. The diameter of open mouth of parabola and focal distance were 1.50 and 0.5 m, respectively, so that the concentrator surface area was 1.767 m².

The buildup of thermoelectric module, an aluminum plate with dimension 120x150x10 mm. were

coated with black paint was designed for radiation heat receiver from the sun and it was the heat source to drive thermoelectric generator. Four series connected HZ-9 thermoelectric module were used for generate DC electricity from differential temperature. The schematic diagram is shown in Figure 2.

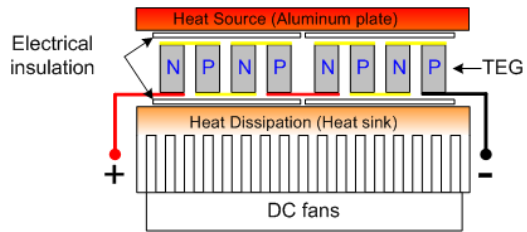


Figure 2 A design of convertor unit include heat source thermoelectric convertor and heat sink

Heat sink with dimensions 120x200x50 mm. were installed on cold side of TEG and cooling fan was mounted on heat sink.

Results and Discussion

The power convertor of the system are test under condition at heat source and heat sink temperature were 523 K and 343 K, respectively. The result is shown in Figure 3.

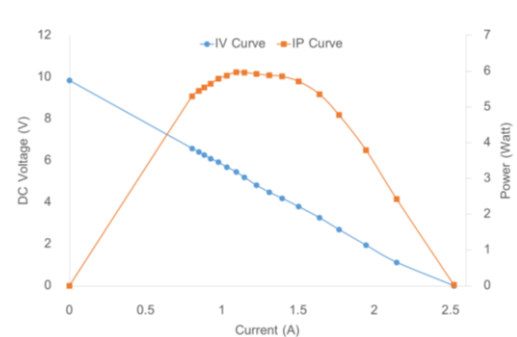


Figure 3 Power loading characteristic, which show the relationship between voltage and power of TEG module.

Table 1 Measured and calculated parameters on 28th march 2016

Time	Measured					Calculated			
	I_{sun}	T_h	T_c	V_m	I_m	P_m	ΔT	I_a	η_e
8:30	810	418	315	4.01	0.801	3.21	103	1377.0	0.23
8:45	865	429	318	4.33	0.865	3.75	111	1470.5	0.25
9:00	902	449	319	4.52	0.905	4.09	130	1533.4	0.27
9:15	931	458	320	4.71	0.943	4.44	138	1582.7	0.28
9:30	956	464	322	4.89	0.974	4.76	142	1625.2	0.29
9:45	971	468	323	4.92	0.985	4.85	145	1650.7	0.29
10:00	983	469	324	4.95	0.991	4.91	145	1671.1	0.29
10:15	1004	473	325	4.99	0.997	4.98	148	1706.8	0.29
10:30	1042	481	327	5.06	1.006	5.09	154	1771.4	0.29
10:45	1051	483	327	5.09	1.011	5.15	156	1786.7	0.29
11:00	1070	483	328	5.12	1.014	5.19	155	1819.0	0.29
11:15	1077	494	329	5.23	1.041	5.44	165	1830.9	0.30
11:30	1088	503	329	5.39	1.056	5.69	174	1849.6	0.31
11:45	1089	506	330	5.42	1.072	5.81	176	1851.3	0.31
12:00	1079	510	332	5.47	1.093	5.98	178	1834.3	0.33
12:15	1083	513	333	5.5	1.111	6.11	180	1841.1	0.33
12:30	1092	515	334	5.56	1.129	6.28	182	1856.4	0.34
12:45	1087	513	334	5.53	1.118	6.18	179	1847.9	0.33
13:00	1094	508	335	5.52	1.108	6.12	173	1859.8	0.33
13:15	1069	506	335	5.43	1.074	5.83	171	1817.3	0.32
13:30	1056	505	335	5.39	1.055	5.69	170	1795.2	0.32
13:45	1056	505	335	5.36	1.067	5.72	170	1795.2	0.32
14:00	1052	505	336	5.34	1.063	5.68	169	1788.4	0.32
14:15	1043	501	335	5.29	1.060	5.61	166	1773.1	0.32
14:30	1015	495	335	5.24	1.057	5.54	160	1725.5	0.32
14:45	985	474	333	5.1	0.999	5.09	141	1674.5	0.30
15:00	947	470	329	4.97	0.995	4.95	141	1609.9	0.31
15:15	853	446	325	4.16	0.830	3.45	121	1450.1	0.24
15:30	798	435	320	3.66	0.731	2.68	115	1356.6	0.20
15:45	778	425	317	3.23	0.645	2.08	108	1322.6	0.16
16:00	691	413	314	3.01	0.601	1.81	101	1174.7	0.15

Table 2 Measured and calculated parameters on 29th march 2016

Time	Measured					Calculated			
	I_{sun}	T_{hot}	T_{cold}	V_m	I_m	P_m	ΔT	I_{st}	η_e
8:30	815	433	324	3.59	0.717	2.57	109	1440.11	0.18
8:45	914	444	329	4.03	0.805	3.24	115	1615.04	0.20
9:00	921	445	332	4.11	0.821	3.37	113	1627.41	0.21
9:15	924	448	332	4.14	0.827	3.42	116	1632.71	0.21
9:30	951	454	333	4.19	0.837	3.51	121	1680.42	0.21
9:45	978	458	335	4.2	0.839	3.52	123	1728.13	0.20
10:00	1008	461	338	4.27	0.853	3.64	123	1781.14	0.20
10:15	1018	463	338	4.87	0.973	4.74	125	1798.81	0.26
10:30	1035	471	338	4.95	0.998	4.94	133	1828.85	0.27
10:45	1089	482	339	5.06	1.011	5.12	143	1924.26	0.27
11:00	1092	488	341	5.12	1.023	5.24	147	1929.56	0.27
11:15	1105	493	342	5.27	1.055	5.56	151	1952.54	0.28
11:30	1100	504	346	5.36	1.07	5.74	158	1943.70	0.30
11:45	1128	503	346	5.37	1.073	5.76	157	1993.18	0.29
12:00	1121	502	346	5.34	1.067	5.70	156	1980.81	0.29
12:15	1115	501	346	5.32	1.063	5.66	155	1970.21	0.29
12:30	1106	499	346	5.3	1.059	5.61	153	1954.30	0.29
12:45	1097	498	346	5.27	1.053	5.55	152	1938.40	0.29
13:00	1085	497	345	5.24	1.047	5.49	152	1917.20	0.29
13:15	1077	496	345	5.22	1.043	5.44	151	1903.06	0.29
13:30	1054	495	345	5.21	1.041	5.42	150	1862.42	0.29
13:45	1052	495	344	5.19	1.037	5.38	151	1858.88	0.29
14:00	1041	494	343	5.2	1.039	5.40	151	1839.45	0.29
14:15	1036	492	341	5.17	1.033	5.34	151	1830.61	0.29
14:30	1001	483	341	5.08	1.015	5.16	142	1768.77	0.29
14:45	980	473	341	4.96	0.991	4.92	132	1731.66	0.28
15:00	954	461	339	4.52	0.906	4.10	122	1685.72	0.24
15:15	873	447	339	4.15	0.829	3.44	108	1542.59	0.22
15:30	820	437	339	3.64	0.727	2.65	98	1448.94	0.18
15:45	741	425	338	3.21	0.641	2.06	87	1309.35	0.16
16:00	679	419	337	3.02	0.603	1.82	82	1199.79	0.15

Nomenclature I_{sun} local radiation intensity (W/m^2) T_h thermoelectric hot side temperature (K) T_c thermoelectric cold side temperature (K) V_m match load output voltage (V) I_m match load current (A) P_m maximum output power (W) ΔT temperature difference between hot and cold side of TEG (K) I_a radiation power on parabolic dish (W) η_e electrical efficiency (%)

Our experiment on 28th and 29th March 2016 at Department of Physics, Faculty of Science, Ubon Ratchathani University, collection all of the data from 8:30 a.m. to 4:00 p.m. solar radiation intensity, hot and cold side temperature of TEG module, match load voltage and current were measured every fifteen minutes.

The electricity are generated depend on differential temperature between hot side and cold side of thermoelectric module. Temperature of heat source increase because of the solar intensity is increase, cold side was cooled by heat sink and fan. The result of the power converter is shown in Figure 4.

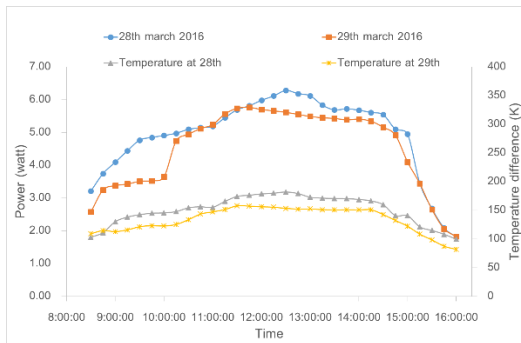


Figure 4 Show the power convertor of the system and temperature difference on both side of TEG versus time

From the result of the both experiment days, maximum power output obtained at the matched load, the electrical efficiency [1] of the TEG module can be computed by:

$$\eta_e = \frac{P_{max}}{I_a} \times 100 \quad (1)$$

$$I_a = I_{sun} \times \text{Area of parabolic dish} \quad (2)$$

The electrical efficiency of the system is shown in Figure 5.

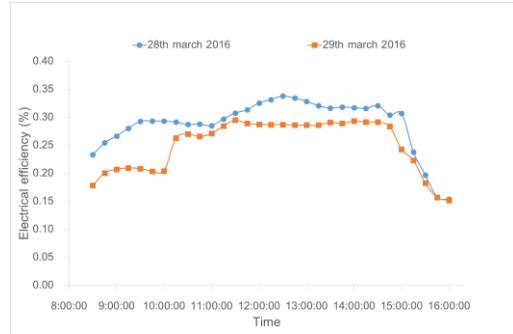


Figure 5 Plot of electrical efficiency versus time on both experiment days

Conclusions

The prototype of parabolic dish solar concentration for electrical power generator based on TEG modules was fabricated and tested. The differential temperature between hot side and cold side of module varies with intensity of solar radiation. Artifact was setup on 5th floor Department of Physics building, Faculty of Science, Ubon Ratchathani University on the north east of Thailand. Our experiment on 28th and 29th march 2016, collection of the data from 8:30 a.m. to 4:00 p.m. From the result of experiment, at 12:30 on 28th March maximum temperature from solar radiation heat on hot side of TEG is 515 K, when intensity of sun is 1092 w/m² and the maximum power output is 6.28 W.

Acknowledgments

The authors gratefully acknowledge Department of Physics, Faculty of Science, Ubon Ratchathani University for financial support.

References

- [1] Özdemir, A.E., et al. 2015. "The experimental design of solar heating thermoelectric generator with wind cooling chimney". **Energy conversion and management**. 98, 217-133.

- [2] Muthu, G., Shamugum, S. and Veeruppan, AR., 2014. "Solar parabolic dish thermoelectric generator with acrylic cover". **Energy Procedia**. 54, 2–10.
- [3] Hasan Nia, M., et al. 2014. "Cogeneration solar system using thermoelectric module and fresnel lens". **Energy Conversion and Management**. 84, 305–310.
- [4] Anh-Khoi Trinh, et al. 2014. "Solar thermal energy conversion to electrical power". **Applied Thermal Engineering**. 70, 675-686.
- [5] Alvaro Martinez, David Astrain and Antonio Rodriguez. 2014. "Zero – power - consumption thermoelectric system to prevent overheating in solar collectors". **Applied Thermal Engineering**. 73, 1103-1112.
- [6] Ning Zhu, et al. 2014. "Development of small solar power generation system based on thermoelectric generator". *Energy Procedia*. 52, 651-658.
- [7] Jin Zhang, Yimin Xuan and Lili Yang. 2014. "Performance estimation of photovoltaic-thermoelectric hybrid systems". **Energy**. 78, 895-903.
- [8] Chavez-Urbiola, E.A., Vorobiev, Yu.V, Bulat, L.P. 2012. "Solar hybrid systems with thermoelectric generators". **Solar Energy**. 86, 369–378.

The Development of Innovation of the Magnetic Force Exerting on a Current-Carrying Wire in Physics for Undergraduate Students

N. Wattanasupinyo^{*}

Physics Program, Faculty of Science, Bansomdejchaopraya Rajabhat University, 1061 Isaraphab Road, Dhonburi, Bangkok, 10600

*E-mail: nuntanut.bsru@hotmail.com

Abstract

The researcher is creating innovative learning kits about "The magnetic force exerting on a current-carrying wire" and activities for teaching the concepts of the magnetic force for pre-service physics science teacher course. The objectives of this research was to investigate the efficiency of innovative learning on pre-service teacher's achievement and satisfaction on the intervention. The participants were 63 second year students in pre-service science teacher course. The findings revealed that the magnetic force had efficiency higher than a defined criteria 95/85. The post-test is significantly higher than the pre-test scores at .01 level. The level of satisfaction in terms of student interest and knowledge understanding is 4.26 which is interpreted as good. Students remarked that the innovation is interesting, novelty, easy to use, comprehensible, inexpensive and conveniently available.

Keyword: Innovation, Magnetic field, Electric current

Introduction

Learning management in the present is emphasized in practical learning. Learner can think, analyze and practice with learning process that is managed by themselves. They found that the physics subject learning is the basis of science and technology. Physics has been the both logic and mathematic combination subject for technology development [1]. In Thailand, physics is one of the science subject group that contains the matter about nature phenomena, principles, law and fundamental theory of physics. However, the contents in general physics subject are applied for solving problem in class, students cannot use for the daily life problem solving because the teaching not be designed for real practice [2].

The practice-based sciences teaching can attract the interesting of children. Moreover, learner

can understand clearly by direct experiment. Cause of this, the efficiently teaching have to create or develop educational innovation for physics teaching and learning.

For general science program in faculty of education, the physics for science teacher II is fundamental subject for the secondary year of student in university. The subject is consisted of electric and magnetic theory as teaching 3 hours per week. From the behavior observation of students in the classroom is found that students not have enough interest, enthusiasm and concentrate for learning physics. These results show that the physics learning is boring and difficult to comprehend because of the only theory-base teaching cannot influence the imagination to student. Consequently, teachers have to design and produce the innovation for learning support [3].

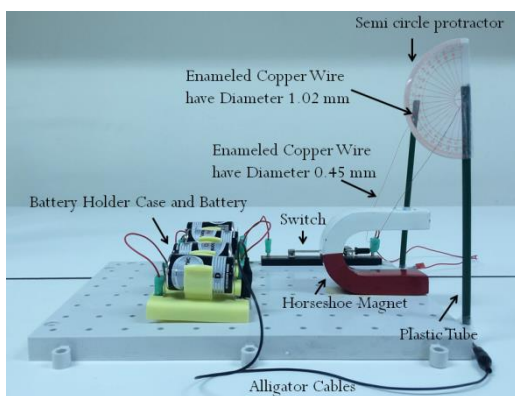
Therefore, we proceed to solve the problem by using innovation of learning about the magnetic force exerting on a current-carrying wire in subject of physics for science teacher II, general science program, Faculty of education at Bansomdejchaopraya Rajabhat University. The sample size of student is equal to 63 persons, we expect that students are more understanding and interesting in physics with our learning management.

Materials and Methods

The researcher has to creating innovative learning of "The magnetic force exerting on a current-carrying wire" for teaching and learning in Physics for Science Teachers 2 subject. The innovative learning should help students to understand the content and concept of the relationship between variables in equations. The magnetic force (F) on a length (L) of wire that carrying a current (I) through a magnetic field (B) is [4]

$$F = ILB\sin\theta \quad (1)$$

where θ (theta) is the angle between the wire and the magnetic field. The direction of the vector L is the same as the direction of the current through the wire.



(b)

Figure 1 Innovative learning of the magnetic force exerting on a current-carrying wire model.

The structures of the innovation consist of 4 PCs size battery holder case, battery 1.5 V 4 PCs, switch

1 piece, alligator cables 6 PCs, plastic tube 2 PCs, 2 size enamelled copper wire \varnothing 1.02 mm and \varnothing 0.45 mm, two size horseshoe magnets 103 x 83 x 30 mm and 83 x 83 x 20 mm and semi-circle protractor 1 piece. The model show as in Figure 1.

Methods

Innovative learning about the magnetic force exerting on a current-carrying wire was used in the lesson plan called "Learning Cycle 5 Step (5E)" as follows [5][6]:

Step 1 : Engagement Phase

1.1 Before proceeding with the learning activities, divide students in a group of 3-4 person according to the student order number then take the pre-test.

1.2 Investigate the student's prior knowledge by show the magnet in front of them and let them explain what they have learnt about magnets. Let them brainstorm what will happen if we take the wire that have electric current pass through near a magnet.

1.3 Check their schemata on magnetics, such as the direction of electric current and the direction of magnetic field so the teacher will know what should explain and be fulfilled to students.

Step 2 : Exploration Phase

Students in each group planned to conduct experiments by possible hypotheses setting and take the experiment about "Magnetic force exerting on a current-carrying wire" in Activity Sheet 1 then investigate and search for knowledge within a group. Write the conclusion and discussion of the experiment as follows:

2.1 Students use the Innovative learning for experiment about the magnetic force exerting on a current-carrying wire;

2.2 Students experiment as a group and follow the Activity Sheet 1 to answer the questions, as well as to collect data to answer the issues that they are interesting.

The method of Activity Sheet 1

The objective of this method is student can understand and explain the relation between direction of F, B and I variables. Students should comprehend the intensity of magnetic field and current affect to magnetic force. This method begin with students compose the materials to the learning model following the figure 1b and figure 2. Afterwards, follow the 3 parts of Activity Sheet 1 below.

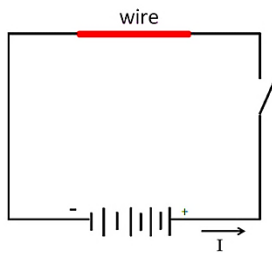


Figure 2 Circuit of innovation model.

Part 1:

This part will explain how the size and position of horseshoe magnet affect to magnetic field intensity. The student should perform the experiment as below.

1. Students have to place the metal clip to the 8 marked positions on both horseshoe magnets show as in the figure 3.
2. Students measure the intensity of magnetic field on every marked positions by hand feeling and record the result of the different force affect to student's hand in experimental table.
3. Students measure the intensity of magnetic field on every marked positions by teslameter and record the result in experimental table.

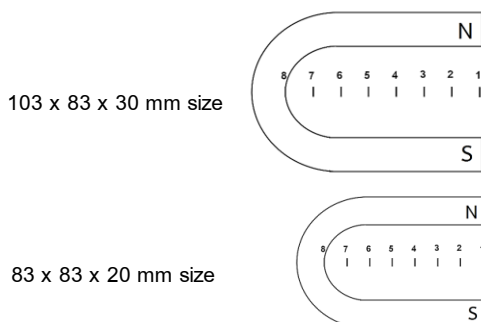


Figure 3 Show the marked positions on horseshoe magnets.

Part 2:

This part will explain the relation between direction of F, B and I variable. The student should perform the experiment as below.

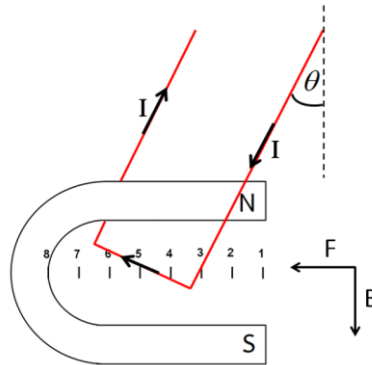


Figure 4 Show the angle value measurement after place the horseshoe magnet close to the current-carrying wire.

1. Students hold a large horseshoe magnet close to hanging current-carrying wire length L as the figure 4 and observe the direction of the magnetic force to a current-carrying wire. Afterwards, draw direction of F, B and I variable from observation.
2. Students slide the large horseshoe magnet closer to the hanging wire length L at every marked positions on magnet and record the angle value of wire that measure by semi-circle protractor in the experimental table.

Part 3:

The last part will explain the effect of current to force of magnetic field. The students should perform the experiment as below.

1. Students adjust the current by change the amount of batteries and fix the position of magnet from marked positions in part 1. The students record the angle value of the wire that read from a semi-circle protractor in the experimental table.

Step 3: Explanation Phase

- 3.1 Students of each group present their results in front of the class.

3.2 Students and teacher discuss together and conclude their experiment according to the Activity Sheet 1.

3.3 Teacher explains more details to students from the experiment by explain the relationship between the direction of electric current, the direction of magnetic field, the direction of force from magnetic field and the relationship of the density of magnetic field affecting force towards flowing electric current that influences force from magnetic field.

3.4 Students and teacher summarize what they have done together.

Step 4: Elaboration Phase

When students understand the problem, teacher asks students about right hand rule. If students have not enough understand clearly, the teacher should explain the relation between F, B and I parameter in right hand rule [7] and the experiment to the student for strengthen the knowledge.

Step 5: Evaluation Phase

5.1 Teachers test students understanding about the magnetic force exerting on a current-carrying wire by let them answer the following questions:

- What variables affect the direction of magnetic force exerting on a current-carrying wire?
- What is the effect of magnetic field intensity and current towards magnetic force?
- Can we apply this knowledge to the other work? If can, what task it work ?

5.2 Let the students speak about the new knowledge they have received whether it is more or less than before learning and what they can use this knowledge to comprehend the other learning.

5.3 Check the understanding of students by asking them to drawing mind mapping to summarize what they have been taught from the lesson.

5.4 Students take the post-test.

Results and Discussion

1. The efficiency of innovative learning with comparing the criteria 80/80

The testing results of innovative learning on "The magnetic force exerting on a current-carrying wire" with 63 second year students, we found that the achievement of exercise and activity sheet during learning mean score is 18.97 out of 20 points, which is 94.88 percent or efficiency value E1 = 95, and the testing achievement of post learning mean score is 8.50 out of 10 points, which is 85.00 percent or efficiency value E2 = 85. It is higher than the criterion 80/80, as shown in table 1:

Table 1 Results of the trial to determine the effectiveness of innovation.

Number of student (person)	During the lesson (Score 20 points)		After lesson (Score 10 points)	
	\bar{X}	E1 (%)	\bar{X}	E2 (%)
63	18.97	95.00	8.50	85.00

Table 1 shows the results of the trial, we found that the ratio E1 / E2 of Innovative Learning is 95/85, which is higher than the performance criterion defined 80/80. Such a result confirm that it is an efficient innovation.

2. The using of the innovative learning on "The magnetic force exerting on a current-carrying wire"

This analysis is the comparing between pre-test and post-test scores by using the statistics method, SPSS for Windows program, as shown in Table 2

Table 2 Show the comparison of total score of pre-test and post-test scores that indicate student's understanding and learning of "The magnetic field force exerting on a current-carrying wire" before and after using the innovative learning.

Resource	Number	\bar{X}	S.D	t	df	sig.
Pre-test	63	4.79	2.55			
Post-test	63	8.50	1.48			
				-9.682**	62	.00

** There is a statistically significant level of .01

The achievement from Table 2, the comparison between pre-test and post-test score, The post-test is significantly higher than the pre-test scores at .01 level.

3. The data analysis of satisfaction learning/ understanding levels, we found that the level of satisfaction in terms of interest and knowledge understanding of the students is 4.26, which is interpreted as good and standard deviation is 0.45. The suggestion of students to the innovation feature is has interesting, easy to use, easy to learn and understand. It has novelty, never seen before. It is uncomplicated and has the compact size which can be modified. It also conveniently available and use inexpensive material. It can generally help learner to understand the content more easily, they can clearly see the direction of the force and find the relation between variables and force. The teachers and students can use it as the learning tool in the future [8].

The instrument disadvantage is that it made from weak materials. Especially, the antenna may be easily damaged during use. The angle value is hardly measured because the wire does not quite match. It might be a cause of error measurement. The current in battery is decreased after the trial period, which can be a cause of error measurement.

Conclusions

The findings revealed that the "Magnetic force" had efficiency higher than a defined criteria 95/85. The post-test is significantly higher than the pre-test scores at .01 level. The level of satisfaction in terms of students interest and knowledge understanding is 4.26 which is interpreted as good.

Students remarked that the "Magnetic force" is interesting, novelty, easy to use, comprehensible, inexpensive and conveniently available.

Acknowledgments

The researcher would like to thanks colleague in Sciences (Physics) program, Faculty of science, Bansomdejchaopraya Rajabhat University.

References

- [1] Monchai Sitthichan. 2004. "The effects of practicing imagination in physics instruction on learning achievement and imagination abilities of mathayomsuksa five students". Master. Education (Science Education). Graduate School Bangkok (Thailand), Chulalongkom University.
- [2] Krirk Saksuparb. 2013. Development of an instructional model (PECA) with emphasis on Physics problems solving ability of upper secondary student. Ed.D (Science Education). Graduate School. Bangkok (Thailand). Srinakharinwirot University.
- [3] Bat-Sheva Eylon and Esther Bagno. 2006. Research-design model for professional development of teachers: Designing lessons with physics education research. Physical Review Special Topics – Physics Education Research 2. pp. 1.
- [4] David Halliday, Robert Resnick, Jearl Walker. 2011. Magnetic force on a current-carrying wire. John Wiley & Sons, Inc. pp. 750.
- [5] Arlington, VA: National Science Teachers Press. Eisenkraft, A. 2003. Expanding the 5E model. The Science Teacher, 70, pp. 56- 59.
- [6] Coe, M. A. 2001. Inquiry approach: The 5 E learning cycle. Retrieved 12 February 2010 from <http://faculty.mwsu.edu/west/maryann.coe/coe/inquire/inquiry.htm>.
- [7] David Halliday, Robert Resnick, Jearl Walker. 2011. Magnetic Fields. Fundamentals of Physics. John Wiley & Sons, Inc. pp 752.
- [8] Collins, A. 2002. How students learn and how teachers teach. In R. W. Bybee (ed.), Science educators' essay collection: Learning science and the science of learning .pp. 3-11.

Period Change of Binary System V1799 Orionis

P. Panpiboon*, R. Lakhom, and W. Choawanklarng

Program in Physics, Faculty of Science and Technology, Rajabhat Maha Sarakham University,
Maha Sarakham, 44000

*E-mail: ppanpiboon@gmail.com

Abstract

Period change of binary system V1799 Orionis in this work used 0.5 meter reflecting telescope with CCD photometric system in blue, visual and infrared bands. This research was observed at Thai National Observatory, Chiang Mai. A light curve of V1799 Orionis was analyzed using program MaxIm DL5 and its period change was also calculated. The results show that its orbital period and a continuous weak increase at a rate are 0.2903039 day and 6.43876 millisecond per year, respectively. Evolution of V1799 Orionis is corresponding to Thermal Relaxation Oscillation theory.

Keywords: Binary system, Period change, V1799 Orionis, Thermal relaxation oscillation

Introduction

V1799 Orionis or V1799 Orion or V1799 Ori or GSC 96-175 was found to be a variable star by Hanley & Shapley (1940) [1]. Period variations of V1799 Orionis have been studied by numerous authors (period shorter than 0.3 days). Akerlof et al. (2000) rediscovered it to be an eclipsing binary of W UMa type [2]. This system is a W-type, extremely shallow- contact binary presented by Samec et al. (2010) [3]. However, Liu et al. (2012) reported the long-term period increase, together with the exceptional low degree of contact, suggests that the binary may be at a critical stage which is predicted by the Thermal Relaxation Oscillation (TRO) theory [4].

This study presents CCD photometric system in blue, visual and infrared bands (BVI) observations for binary system V1799 Orionis and investigation on the orbital period change. An analysis for long-term period change is described the evolution of this system to become a semi-contact binary system in the future.

Materials and Methods

V1799 Orionis was observed at Thai National Observatory, Chiang Mai (longitude: 98°48'53" E, latitude: 18°57'25" N) on December 28-29, 2015 and January 8, 2016. The 0.5-m telescope, equipped with an Andor Tech 2048 × 2048 CCD, was used for BVI filter bands with an exposure time of 60 seconds. Data reduction and BVI differential magnitude measurements were made with MaxIm DL5 program. The stars GSC 96–299 and GSC 96–321 were used as comparison and check stars, respectively. Table 1 lists coordinates and magnitudes of V1799 Orionis and the comparison and check stars. We also collected the eclipsing binaries minimum time of CCD photometric system database and the values of O-C of residual of linear fit literatures at <https://www.aavso.org/bob-nelsons-o-c-files>. The data for V1799 Orionis were initially phased with ephemeris of Khruslove (2006):

$$\text{Min.}I (HJD) = 2451524.829 + 0^d.29031 \times E \quad (1)$$

where E stand for the epoch number [5].

Table 1 Coordinates and magnitudes of V1799 Orionis and the comparison and check stars.

Star	RA(2000)	Dec(2000)	Magnitude
V1799 Orionis	04 ^h 47 ^m 18 ^s .19	+06° 40' 56".1	12.9
comparison	04 ^h 47 ^m 25 ^s .83	+06° 45' 44".8	12.05
check	04 ^h 47 ^m 31 ^s .70	+06° 36' 51".6	12.06

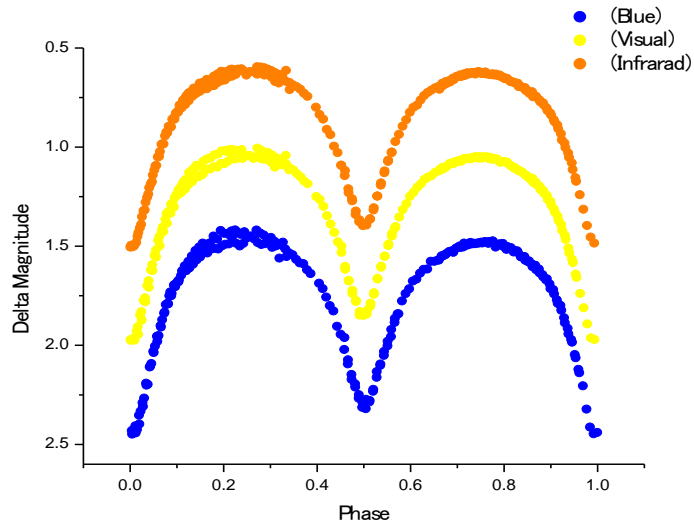


Figure 1 Observed light curves for V1799 Orionis in BVI bands.

Table 2 New minimum times of CCD photometric system in BVI bands.

Observed Time	Filter	HJD (2,400,000+)	Minimum Light
December 28 th , 2015	Blue	57,385.3385	II
	Visual	57,385.3377	II
	Infrared	57,385.3387	II
	BVI (average)	57,385.3383	II
December 29 th , 2015	Blue	57,386.0651	I
	Visual	57,386.0647	I
	Infrared	57,386.0651	I
	BVI (average)	57,386.0650	I
December 29 th , 2015	Blue	57,386.2089	II
	Visual	57,386.2093	II
	Infrared	57,386.2095	II
	BVI (average)	57,386.2093	II
January 8 th , 2016	Blue	57,396.2253	I
	Visual	57,396.2243	I
	Infrared	57,396.2249	I
	BVI (average)	57,396.2248	I

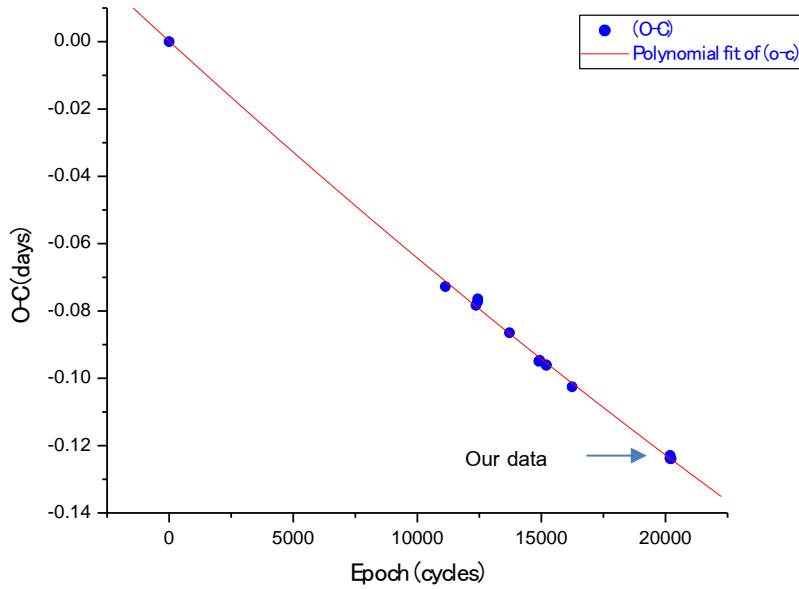


Figure 2 The O-C diagram for the minimum times of V1799 Orionis. The solid points represent the O-C, where the direction to solid point represent our data.

Table 3 The minimum times and their relevant parameters of V1799 Orionis.

HJD (2,400,000+)	Error	Epoch	(O-C)	Min.	References
51524.8290	±0.0000	0.0	0.00000	I	IBVS 5699 [5]
54756.9226	±0.0011	11133.5	-0.07278	II	IBVS 5871 [6]
55113.8532	±0.0005	12363.0	-0.07833	I	IBVS 5929 [11]
55135.7727	±0.0004	12438.5	-0.07723	II	IBVS 5920 [7]
55135.9187	±0.0005	12439.0	-0.07639	I	IBVS 5920 [7]
55506.9248	±0.0003	13717.0	-0.08647	I	IBVS 5960 [8]
55849.6273	±0.0002	14897.5	-0.09496	II	OEJV 0160 [12]
55859.4981	±0.0001	14931.5	-0.09467	II	IBVS 6070 [13]
55937.5900	±0.003	15200.5	-0.09615	II	IBVS 6029 [9]
55937.7353	±0.0008	15201.0	-0.09601	I	IBVS 6029 [9]
56237.9093	±0.0002	16235.0	-0.10255	I	IBVS 6042 [10]
57385.3383	±0.0003	20187.5	-0.12383	II	This study
57386.0650	±0.0007	20190.0	-0.12293	I	This study
57386.2093	±0.0005	20190.5	-0.12379	II	This study
57396.2248	±0.0004	20225.0	-0.12391	I	This study

Note: IBVS is Information Bulletin on Variable Stars and OEJV is Open European Journal on Variable Stars.

The linear ephemeris of V1799 Orionis was then monitored many times by several researchers such as Khruslove (2006), Diethelm (2009, 2010, 2011, 2012,

2013), Nelson (2010), Honkava et al. (2013) and Hubscher and Lehmann (2013) [5-13]. The linear ephemeris was obtained for V1799 Orionis by Diethelm,

(2013) as a revised it which indicates the times of minimum light [10].

$$Min.I (HJD) = 2456237.90927 + 0^d.2903036 \times E \quad (2)$$

Results and Discussion

The BVI magnitude light curves for V1799 Orionis are shown in Figure 1, along with the computed curves from photometric solution. The light curves will help us to derive more reliable parameters of the binary. Using a least-square method, the new minimum times of CCD photometric system in BVI bands were determined and are listed in Table 2. The O-C residuals for all the times of minimum light according to the linear and quadratic ephemerides were calculated and listed in Table 3. According to the quadratic ephemeris, we present the O-C diagram of the period analysis of V1799 Orionis in Figure 2. we amended the linear ephemeris of V1799 Orionis:

$$Min.I (HJD) = 2457396.2234 + 0^d.2903039 \times E \quad (3)$$

The quadratic term from Equation 3 denotes a continuous period increase at a rate of dP/dt which would impact the light curves and the general trend of O-C data which can be used as a preliminary prediction of times of light minimum with the orbital period increase indicates mass transfer from the more massive component to the less massive component. Thermal Relaxation Oscillation theory using predicted physical mechanisms including mass transfer between the components, presence of magnetic activities [14]. The result reveals that the orbital period of V1799 Orionis continuously increase with a rate of $dP/dE = 5.92313 \times 10^{-11}$ day per cycle or $dP/dt = 6.43876$ millisecond per year. The period increase can be explained shows orbital period change of V1799 Orionis which corresponding to the theory of TRO.

Conclusions

We presented new blue, visual and infrared bands for V1799 Orionis and discussed its period variation analysis and the photometric solutions of the

binary system. Based on research on the orbital period analysis of V1799 Orionis, we added some new times of minimum light, and derived the new linear and quadratic ephemeris the results shown that its orbital are 0.2903039 day. It turns out that the orbital period of the binary system is increases at a rate of $dP/dE = 5.92313 \times 10^{-11}$ day per cycle or $dP/dt = 6.43876$ millisecond per year. The period increase can be explained shows orbital period change of V1799 Orionis which corresponding to the Thermal Relaxation Oscillation theory.

Acknowledgments

This work was supported by Rajabhat Maha Sarakham University. Observations were obtained, using the 0.5-m telescope at Thai National Observatory, Chiang Mai. This research has made use of the SIMBAD online database, operated at CDS, Strasbourg, France.

References

- [1] Henley, C. M., and Shapley, H. 1940. **Harvard College Observatory Bulletin**. 913, 9.
- [2] Akerlof, C. et al. 2000. ROTSE all-sky surveys for variable stars. I. test fields. **The American Astronomical Society**. 119: 1901-1913.
- [3] Samec, R.G. et al. 2010. "The very-low-fill-out W-type binary V1799 Orionis". **The Observatory**. 130: 364-371.
- [4] Liu, N. P. Qian, S. B., Liao, W. P., He, J. J., Zhao, E. G., and Liu, L. 2012. "Photometric investigation of the K-type extreme-shallow contact binary V1799 Orion". **Research in Astronomy and Astrophysics**. 14: 1-14.
- [5] Khruslove, A. V. 2006. **Information Bulletin on Variable Stars**. 5699, 1.
- [6] Diethelm, R. 2009. **Information Bulletin on Variable Stars**. 5871, 1.
- [7] Diethelm, R. 2010. **Information Bulletin on Variable Stars**. 5920, 1.

- [8] Diethelm, R. 2011. **Information Bulletin on Variable Stars**. 5960, 1.
- [9] Diethelm, R. 2012. **Information Bulletin on Variable Stars**. 6029, 1.
- [10] Diethelm, R. 2013. **Information Bulletin on Variable Stars**. 6042, 1.
- [11] Nelson, R. H. 2010. **Information Bulletin on Variable Stars**. 5929, 1.
- [12] Honkava, K. et al. 2013. **Open European Journal on Variable Stars**. 0160, 1.
- [13] Hubscher, J. and Lehmann, P. B. 2013. **Information Bulletin on Variable Stars**. 5929, 1.
- [14] Wang, D., Zhang, L., Han, X. L., Agerer, F., Pi, Q., and Wang, S. 2015. "Photometric study of the short-period eclipsing binary V441 Lac". **New Astronomy**. 36: 32–36.

Time Uncertainty on Thai Lunar Calendar and Tropical Solar Calendar

A. Laphirattanakul*

Department of Physics and Materials Science, Faculty of Science, Chiang Mai University, Chiang Mai, Thailand.

*E-mail: alarthit@gmail.com

Abstract

The difference between Thai lunar calendar and tropical solar calendar was investigated in this study. Phases of the moon regarding to Thai Lunar calendar appear to be different from the tropical solar calendar in each 19-year cycle, which is called Metonic cycle. The periods of both calendars are nearly the same. The synodic period of the Moon and the sidereal period of Earth were used to estimate the uncertainty of the time prediction for lunar phases in the past. Accordingly there was a time shift of the same moon phases within Metonic cycle in Thai lunar calendar to be the function of wave-like form. The result will be further investigated for the correlation with the actual phases of the moon.

Keywords: Synodic period of Moon, Thai Lunar calendar, Tropical solar calendar, Metonic cycle

Introduction

Thai lunar calendar is based on cycles of the Moon phase, which is recognized to be the synodic period of the Moon. Approximately 29.530588 days [1]. However, it seems to keep changing because the orbit of the Moon is nearly on the ecliptic plane. Instead of the tropical solar calendar which is based on the position of Earth on its revolution around the Sun, sidereal period, the tropical solar calendar can accurately indicate the season on Earth if the position of Earth in its orbit around the Sun is reckoned with respect to the vernal equinox. Although the cycle of the Moon phase does not relate with the season on Earth, the Thai lunar calendar was systematically revised to conform with the cycle of season by distinguishing some special years to be Adhika Masa years, which must be attached the additional eighth month in certain lunar year. Nevertheless, every 19 years, 6,939 days, were nearly a common multiple of the synodic period and the sidereal tropical period, therefore the Moon phase in Thai lunar calendar will be nearly similar in 19-year Solar calendar later, which is called Metonic cycle [2]. This study would investigate the tiny difference in time between both calendars within the Metonic cycle.

Materials and Methods

a) Synodic period of Moon

The study about synodic period of the Moon was used to find the equatorial position of Moon during 2011 - 2030 by Ephemeris [3]. The 7,304 data of Julian dates for all

Moon's right ascensions were transformed to Greenwich sidereal time (GST) by equation [4];

$$GST = GST^* - D \quad (1)$$

Where $D = 24 \times INT(GST^*/24)$ and GST^* can be calculated;

$$LST^* = 6.6460556 + 2400.0512617 \cdot \frac{(JD - 2,451,544)}{36525} + 1.0027379 \cdot UT + \ell(\text{in hours}) \quad (2)$$

While JD is Julian date of each data, UT is universal time, and equals to 0 hour at Greenwich. ℓ is longitude in hours unit, and equals to 0 hour at Greenwich. Therefore $LST^* = GST^*$ at Greenwich.

In spherical astronomy, GST is the hour angle of vernal equinox for Greenwich's observer. It must be noted that angular distance until vernal equinox to the Moon, in clockwise direction, is the right ascension of Moon. Therefore the hour angle of the Moon in each day is represented by equation;

$$HA_{moon} = GST - RA_{moon} \quad (3)$$

The Moon's transit times (the point of time when the moon is at the Greenwich's meridian) in 7,304 day were estimated consequently and can be plotted with Julian date. The plot could show the 7,304-day of moon's transit time in the range of 0 - 24 hours. For example, Figure 1 presents part of the plot for the transit time in 2016.

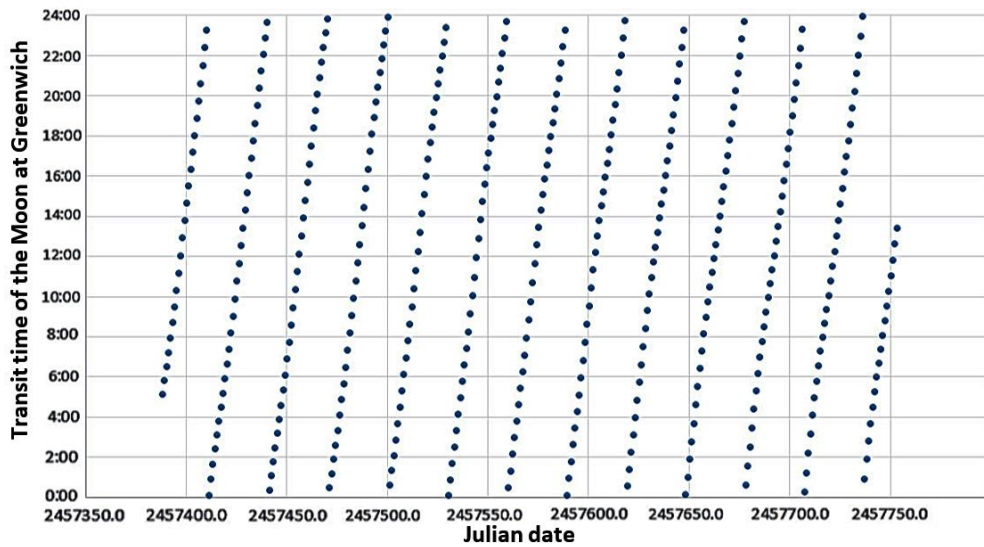


Figure 1 Transit time of the Moon as a function of local time at Greenwich (longitude = 0) in 2016

For next step, the equation of time in each day during 2011-2030 for Greenwich's observer was determined. In addition, the transit time of the Sun could be estimated by equation;

$$(Transit\ time)_{\odot} = 12:00:00 - EoT \quad (4)$$

Where EoT is the equation of time in minutes [3].

Furthermore the transit times of the Sun were plotted with Julian dates during 2011 - 2030 (7,304 data). The plot is presented in Figure 2, for example, in 2016.

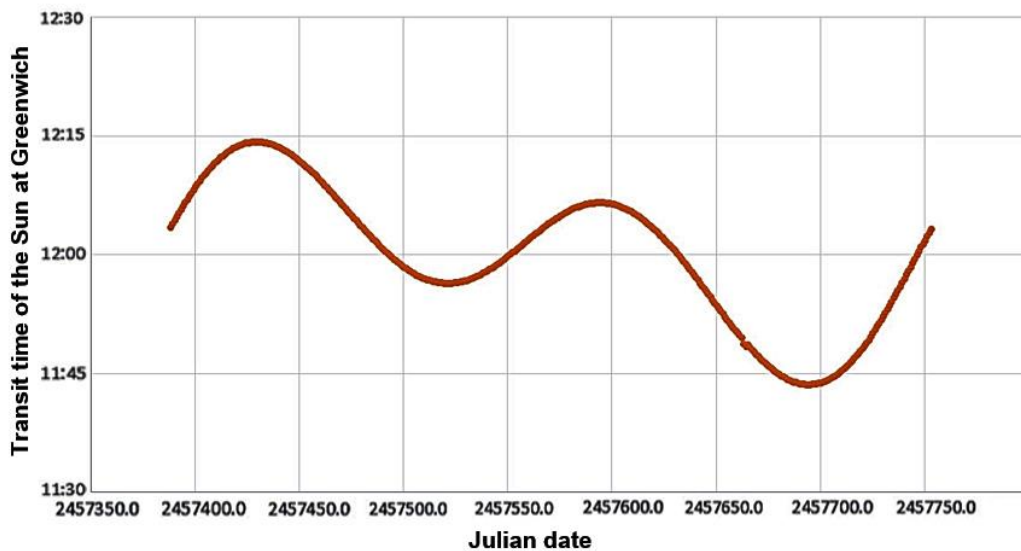


Figure 2 Transit time of the Sun in local time at Greenwich (longitude = 0) in 2016

Transit time of the Moon and the Sun were plotted together with the same Julian date, which are presented, as

example, for 54 days (22 May - 15 Jul 2016) in Figure 3.

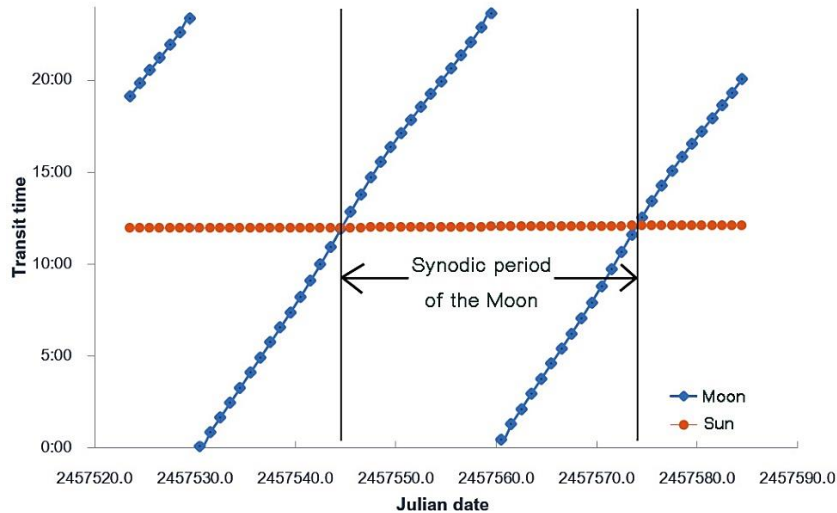


Figure 3 Transit times of the Moon (diamond) and the Sun (circle) with the same Julian dates during 22 May -15 Jul 2016 in local time at Greenwich (longitude = 0). The synodic period of the Moon at certain time can be analyzed by measuring the difference between two intersected points.

In Figure 3, the intersected points of the Moon and Sun's transit times were shown. The Moon and the Sun can be interpreted to locate at observer's meridian above Greenwich's sky. This event occurs when the Sun, the Moon and Earth are in the same alignment. This

phenomenon is called 'new moon'. Therefore the difference between two intersected points in Julian date is the period of certain new moon to the next. This period is called 'synodic period'. Finally the synodic periods from 2011 - 2030 were estimated. The part of list were shown in Table1.

Table 1 The synodic periods of the Moon during 2015 to 2016.

year	JD at new moon	synodic period	year	JD at new moon	synodic period
2015	2457043.12946	29.55890	2016	2457397.61797	29.71487
	2457072.57697	29.44750		2457427.17898	29.56101
	2457101.92589	29.34892		2457456.58448	29.40550
	2457131.24139	29.31550		2457485.90453	29.32005
	2457160.60811	29.36672		2457515.22130	29.31677
	2457190.07626	29.46815		2457544.58515	29.36384
	2457219.63034	29.55409		2457573.99682	29.41167
	2457249.22010	29.58976		2457603.42664	29.42982
	2457278.81245	29.59235		2457632.88794	29.46130
	2457308.43997	29.62752		2457662.42005	29.53211
	2457338.14099	29.70102		2457692.10052	29.68047
	2457367.90311	29.76211		2457721.93755	29.83703
		2457751.81326	29.87571		

It must be noted that the synodic periods of the Moon keep changing because the orbit of the Moon is closer to ecliptic plane than the orbit of Earth. However if we compare the

synodic period between 19-year interval such as between 2011 and 2030, due to fewer decimals of synodic periods, the synodic period tend to be similar, as shown in Table 2.

Table 2 Relation between synodic periods of the Moon between 19-year interval.

year	JD at new moon	Synodic period	year	JD at new moon	Synodic period	uncertainty
	2455920.26402	29.5		2462505.63853	29.5	0.015
2011	2455949.90249	29.6	2030 (19 years later)	2462535.27336	29.6	-0.004
	2455979.60333	29.7		2462564.94964	29.7	-0.025
	2456009.27839	29.7		2462594.58345	29.6	-0.041
	2456038.89325	29.6		2462624.17169	29.6	-0.027
	2456068.49939	29.6		2462653.77200	29.6	-0.006
	2456098.12602	29.6		2462683.41417	29.6	0.016
	2456127.75376	29.6		2462713.06020	29.6	0.018
	2456157.30254	29.5		2462742.61890	29.6	0.010
	2456186.73022	29.4		2462772.05293	29.4	0.006
	2456216.07465	29.3		2462801.41704	29.4	0.020
	2456245.42853	29.4		2462830.78795	29.4	0.017
	2456274.85706	29.4		2462860.24066	29.5	0.024

The uncertainty of synodic periods of the Moon in Table 2 is less than 0.025 day or 36 minutes. This uncertainty is regarded to be the same for 19 years period, which is called 'Metonic cycle'.

b) Sidereal tropical year

The study about sidereal tropical period of Earth was used to find the equatorial positions of the Sun at vernal equinox, at which sun's right ascension is equal to zero,

during 1992 - 2030 by Ephemeris [3]. Next, the point of time in their positions and estimated Julian date at these points were calculated. The difference between two points represents the time, which Earth takes to orbit the Sun in respect to vernal equinox or fixed star. These sidereal periods are shown in Table 3 in comparison with the other period between 19-year interval.

Table 3 Relation between sidereal tropical periods of Earth between 19-year interval.

year	JD at Vernal equinox	tropical year	year	JD at Vernal equinox	tropical year	uncertainty
1992	2448701.866981					
1993	2449067.111873	365.244892	2012	2456006.719178	365.246575	0.001684
1994	2449432.353883	365.242010	2013	2456371.961187	365.242009	-0.000001
1995	2449797.591744	365.237861	2014	2456737.207763	365.246575	0.008714
1996	2450162.834862	365.243119	2015	2457102.449772	365.242009	-0.001110
1997	2450528.079909	365.245047	2016	2457467.687215	365.237443	-0.007604
1998	2450893.331050	365.251141	2017	2457832.938356	365.251142	0.000000
1999	2451258.573059	365.242009	2018	2458198.177388	365.239032	-0.002977
2000	2451623.816514	365.243454	2019	2458563.415661	365.238273	-0.005182
2001	2451989.061644	365.245130	2020	2458928.659492	365.243831	-0.001299
2002	2452354.303653	365.242009	2021	2459293.901826	365.242335	0.000326
2003	2452719.541096	365.237443	2022	2459659.148402	365.246575	0.009132
2004	2453084.783105	365.242009	2023	2460024.391934	365.243532	0.001523
2005	2453450.022936	365.239831	2024	2460389.629487	365.237553	-0.002278
2006	2453815.267123	365.244187	2025	2460754.875983	365.246496	0.002309
2007	2454180.504566	365.237443	2026	2461120.115332	365.239349	0.001906
2008	2454545.742009	365.237443	2027	2461485.350482	365.235150	-0.002293
2009	2454910.988584	365.246575	2028	2461850.595201	365.244719	-0.001856
2010	2455276.230594	365.242009	2029	2462215.835603	365.240402	-0.001607
2011	2455641.472603	365.242009	2030	2462581.078613	365.243010	0.001001

In Table 3, the uncertainty of sidereal tropical periods of Earth in 19-year interval is less than 0.009132 day or only 13 minutes because the orbit of Earth is closer to circular plane than the Moon's orbit.

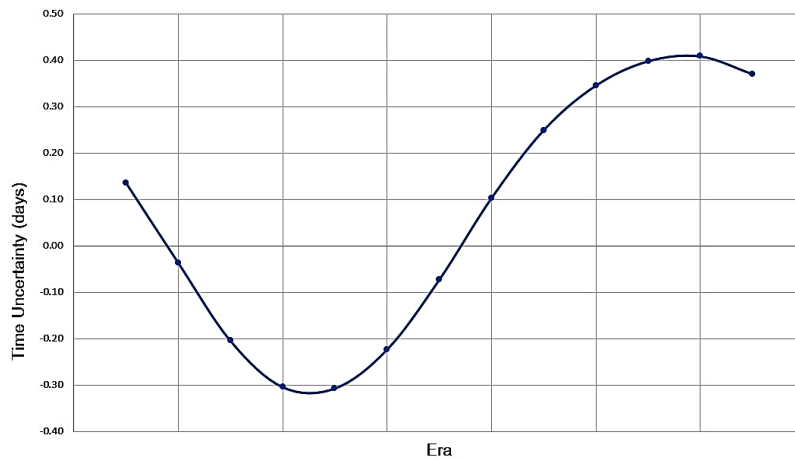
The data of the Moon's synodic period and the Earth's sidereal tropical period were used to compare Thai lunar calendar to tropical solar calendar and to investigate the time uncertainty between them during 19-year cycle or Metonic cycle of both periods in next session.

Results and Discussion

From table1, it was found that the synodic period of the Moon in each month keeps changing. It can be interpreted that the period of certain new moon to the next one, which is the synodic month in Thai lunar calendar keeps changing every month. While the sidereal tropical period of Earth in each year, which is the sidereal year in tropical solar calendar does not change much over time. In this study, the time uncertainty were revealed from investigating the difference between each calendar, as shown in Table 4.

Table 4 Number of days in lunar calendar in respect to tropical solar calendar during 2011 – 2030.

19-year New Moon to New Moon		Total days		Uncertainty (days)	Uncertainty (hours)
		Lunar Calendar	Tropical Solar calendar		
4-Jan-11	4-Jan-30	6939.74227	6939.60601	0.13626	+3h 16m 12.9s
3-Feb-11	2-Feb-30	6939.56999	6939.60601	-0.03602	-0h 51m 52.3s
5-Mar-11	4-Mar-30	6939.40171	6939.60601	-0.20430	-4h 54m 11.3s
3-Apr-11	3-Apr-30	6939.30190	6939.60601	-0.30411	-7h 17m 55.2s
3-May-11	2-May-30	6939.29895	6939.60601	-0.30706	-7h 22m 10.4s
1-Jun-11	1-Jun-30	6939.38259	6939.60601	-0.22342	-5h 21m 43.3s
1-Jul-11	30-Jun-30	6939.53303	6939.60601	-0.07298	-1h 45m 5.9s
30-Jul-11	30-Jul-30	6939.70908	6939.60601	0.10307	+2h 28m 25.5s
29-Aug-11	29-Aug-30	6939.85543	6939.60601	0.24942	+5h 59m 9.6s
27-Sep-11	27-Sep-30	6939.95171	6939.60601	0.34570	+8h 17m 48.2s
26-Oct-11	26-Oct-30	6940.00414	6939.60601	0.39813	+9h 33m 18.2s
25-Nov-11	25-Nov-30	6940.01471	6939.60601	0.40870	+9h 48m 31.7s
24-Dec-11	24-Dec-30	6939.97664	6939.60601	0.37063	+8h 53m 42.4s

**Figure 4** The time uncertainty from new moon to 19-year interval new moon.

In Table 4, the time uncertainty was calculated by the minus of 19-year total days from tropical solar calendar and Thai lunar calendar. The results were plotted and it seems that the time uncertainty is the function of wave-like form in Figure 4. If total days from tropical solar calendar are greater than lunar calendar, the uncertainty is negative values. In contrast, if total days from lunar calendar are greater than tropical solar calendar, the uncertainty is positive one. It could be interpreted between 3-Apr-11 and 3-Apr-30, the uncertainty is about -7h 17m 55s. If the Moon had 0% phase at 14:32:00 on 3 April 2011, it would that the similar moon phase on the same day of next 19 years will

happen with the wave-formed time shift. For example, be 0% phase at 7:14:05 on 3 April 2030. And the time shift is about -7h 22m 10s for next era, between 3-May-11 and 2-May-30.

Conclusions

The result was presented that it is almost similar in moon phase following by Metonic cycle. However, the time uncertainty between lunar calendar and tropical solar calendar keeps tiny changing and it seems that the time uncertainty will be estimated by the function of wave-like form.

Acknowledgement

I would like to take this occasion to thank Dr.Siwicha Wannawichian for her tremendous help in this work.

References

- [1] Chunpongtong, L. 2007. **Patithin Thai Chaeng Darasart Lae Kanitsart**. Bangkok: Rattaya Printing.
- [2] Eade, J.C. 1995. **The calendrical systems of mainland south-east Asia**. Netherlands: E.J. Brill, Leiden.
- [3] Espenak, F. 2015. **Ephemeris** Retrieved September 25, 2015 from <http://astropixels.com/ephemeris/ephemeris.html>
- [4] Henden, A. A. and Kaitchuck, H. R. 1982. **Astronomical Photometry**. New York :Van Nostrand Reinhold Company Inc.
- [5] Soonthornthum, B. 2006. "LANNA MAP OF LUNAR MANSIONS". **Proceedings of the Fifth International Conference on Oriental Astronomy, Chiang Mai, Chiang Mai University**. 5: 145-148.

Designing a Test to Diagnose the Misconception about Energy Conservation

C. Mongkholsiriwattana¹, M. Tanasittikosol¹ and M. Phaksanchai²

¹Department of Physics, Faculty of Science, King Mongkut's University of Technology Thonburi,
126 Pracha Uthit Road, Bang Mot, Thung Khru, Bangkok, 10140

²Faculty of Science, King Mongkut's University of Technology Thonburi,
126 Pracha Uthit Road, Bang Mot, Thung Khru, Bangkok, 10140

^{*}E-mail: apcentre@hotmail.com

Abstract

In this paper, the diagnostic test was designed and created in order to measure the misconception about the energy conservation of the Thai high school students. The design of the test was based on the learning theory in the cognitive domain from the revised Bloom's Taxonomy and the test was made to measure six aspects of learning outcomes. Each question was sub-divided into three tiers. The first tier is multiple-choice related to energy and energy conservation. Whereas, the second tier asks the student for the reason corresponds to the choice he or she chooses in the first tier. And the third tier asks about the confidence level in answering the question. The test had gone through the validation processes such as index of item objective congruence by experts. To complete the design, the test was tried out with twenty-four students to measure the reliability of the test itself. This test is planned to be used to measure the misconception of students participating in STEM-based activity in the future.

Keywords: Misconception test, Three tier test, STEM, Physics education, Conservation of energy

Introduction

The common problem which lecturers and teachers face today is how to diagnose students who have misconception in a particular topic. This is because, in Thailand, the test that has been used to measure the outcome is usually in the multiple-choice format. When students choose the wrong answer, there is no ways the teachers or the lecturers can differentiate those who are lack of knowledge from those who have misconception.

According to [1], students usually have prior knowledge or understanding which depend on their experience. This prior knowledge is called preconception. If this preconception is in conflict with the scientific view, then this preconception is determined as misconception. There are so many ways in which

this misconception can be developed with students. For example, the daily language can cause misconception or misconception can be developed after attending a class. In the research [1], the results revealed that misconception can penetrate deeply into students' minds. Thus to correct the misconception on a particular topic could be really hard.

In this paper, we described the procedure used to develop the misconception test about energy and energy conservation. As one might probably know, there are many reliable tests on different subjects such as force and motion (Force Concept Inventory) and electrical circuit (Electrical Circuit Inventory). However, there is little reliable test on energy and energy

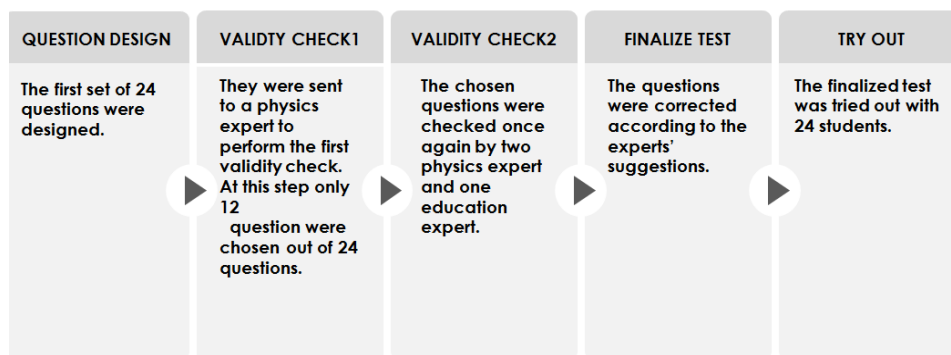


Figure 1 Five-step procedure which was used to create the misconception test about energy and energy conservation.

conservation. Moreover, we found out from the result of the pre-test on mechanics and thermodynamics tested on the students who was about to start their first year at King Mongkut University of Technology Thonburi (KMUTT). The result was most students did not get the correct answers on the topic of energy and energy conservation. Due to these reasons, we tried to develop both diagnostic test to measure the misconception of the student and the curriculum which aids correcting the misconception about energy and energy conservation.

In this paper we set off with the procedure used to create the test in section two. And we will conclude the result we obtained in section three.

Materials and Methods

In this section we discuss the procedure used to create the misconception test about energy and energy conservation. Figure 1 shows five steps procedure used to create the test. It starts with the question design. Afterwards, the test is validated twice by four experts. Then the test is corrected according to the suggestion from the experts. Finally the test is tried out with twenty-four high school students to check for the reliability of the test.

Questions design

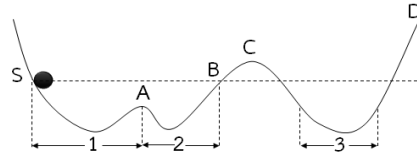
To design the questions, we first started by establishing the learning outcomes the students must achieve after learning about energy and energy conservation. One of the example of the learning outcome is that students are able to define and describe

the elastic potential energy, the gravitational potential energy and the kinetic energy of associated with a particle. These learning outcomes were set to make sure the test would really measure and in the scope of our interest. Then the twenty-four questions in the format of three-tier were developed. These twenty-four questions could be divided into two groups – the first group of the questions was adapted by adding in the second and the third tiers to the original question which served as the first tier [2] and the second group of the questions was newly created. Furthermore, the second group of the questions was developed such that each of the questions could be distinguished students' level of knowledge according to the revised Bloom's taxonomy [3]. The examples of the learning outcomes and the levels of knowledge the test could assess are shown in Table 1. For example question no. 4 can test the level of knowledge of understanding and analyzing and it is subjected to the learning outcome number 1.

The structure of each question is as follow. The first tier of the question is the physics-related question or situation about energy and energy conservation. It is in the four-multiple-choice format. The second tier of the question asks about the reason corresponding to the choice the student chooses from the first tier. The third tier asks for the confidence level of the students' answers – either sure, uncertain or guess. An example of the questions is shown in Figure 2.

9. If released the object position S prediction that an object will climb up. Where is the highest position. When the rails without air resistance, friction and power loss to the system.

- A. Position A B. Position B
 C. Position C D. Position D



Reason _____

Confidence level




 Sure  Uncertain  Guess

Figure 2 This figure shows an example of a question newly created by the author.

To differentiate students into misconception, understanding and lack of knowledge using this test, we use the guidance provided in ref. [3]. The students will have misconception if they answer “sure” in the third tier while they get the first two tiers wrong. The students will be defined as understanding when they correctly answer the first two tiers with “sure” in the third tier. Otherwise the students will be put into a group of lack of knowledge.

First validity check

Once we had the first twenty-four questions, the test was sent to a physics expert at KMUTT to have face validation. At this step the expert eliminated the redundant questions, namely, the questions which measured the same criteria as the other questions.

After performing the first validity check, the number of questions reduced to twelve. And we then moved on to the next step.

Second validity check

The twelve questions were sent to three experts – two physicists and one educationist. The three experts checked whether each question is in congruence with the learning outcomes and the levels of knowledge according to the revised Bloom’s taxonomy or not. This performance is known as Index of item objective congruence (IOC index). After we received the results from the experts, the IOC index was calculated for each question. We found that each question had the IOC index of 1.0

implying that all three experts agreed that each question could be used to assess the level of knowledge according to the revised Bloom’s taxonomy as the author claimed earlier. However, the experts made some correction about language usage in the context and editing the diagrams and charts for more clarity.

Finalizing the test

After checking for the IOC index, we made some correction to the test according to the experts’ advices. These corrections were shortening the sentence, adjusting the language to follow the revised Bloom’s taxonomy and editing diagrams and charts for clarity.

Try out

This was the last step of the procedure. Once we finalized the test. The test then was tried out with twenty-four high school students to measure the reliability of the test. To measure the reliability we used the Cronbach’s coefficient. This was done by calculating the Cronbach’s coefficients three times – each coefficient is for each tier across all twelve questions. The result is given in Table 2.

As a whole, the Cronbach’s coefficients implied that the twelve questions showed a good internal consistency, namely, how good the questions are related together as a group. This was measured against the rule by Sirichai (the coefficient must be greater than 0.5) [4]. When we observed the result of the second group of the questions which was newly created. The Cronbach’s

coefficient also showed a good internal consistency among six questions.

Table 1 This table shows an example of two learning outcomes we set to measure the students. Each question also shows the level of knowledge the test could measure according to Bloom's taxonomy.

Learning outcomes	Level of knowledge						Total
	Remembering	Understanding	Applying	Analyzing	Evaluating	Creating	
1. Definition and description of the elastic potential energy. The gravitational potential energy, kinetic energy	1	3	0	3	0	0	7
1	✓						1
2		✓		✓			2
3		✓					1
4		✓		✓			2
5				✓			1
2. Describes the energy accumulated in the various positions of the objects from the energy conservation law in everyday life.	2	4	2	3	1	0	12
6		✓					1
7			✓	✓			2
8	✓	✓					2
9		✓		✓			2
10				✓			1
11			✓		✓		2
12	✓	✓					2
Total	3	7	2	6	1	0	19

However, when we observed the first group of the questions which was adapted from AAAS. The first tier did not show the internal consistency. This might probably be due to the fact that we randomly selected some questions from a huge set of questions provided by the website.

Table 2 This table shows the Cronbach's coefficients for each tier.

Part of test	tier 1	tier 2	tier 3
1-5,12 adapted from AAAS	0.21	0.70	0.92
6-11 newly developed	0.68	0.50	0.94
1-12 all	0.70	0.77	0.91

Once the tryout had been done, the test was ready to be used to diagnose the students.

Results and Discussion

To check the quality of the test, the content validity and reliability were performed. The Cronbach's alpha coefficient was used to test against the reliability.

The content validity of the test showed the excellent validity of the test with IOC of 1.00 on all questions.

Each question contains three different parts, namely, the knowledge part (first tier), the reasoning part (second tier) and the confidence level of the answer (third tier). The result of the Cronbach's coefficient is shown in Table 2. Overall the reliability shows a good internal consistency of the test. However, if one looks at tier 1 on those question adapted from the AAAS, the internal consistency of this part is low. This might be because we only selected some of the questions out of the whole batch, which, in turn, affects its internal consistency.

Then we will use this test in our future educational research.

Conclusions

In this paper we summarise the procedure used to create a test to diagnose misconception about energy and energy conservation. Overall the test has a very good internal consistency according to the Cronbach's coefficient.

Acknowledgments

A special thanks to the experts in Physics Dr.Sikarin Yookong and Dr.Wittaya Kanchanapusakit, and the experts in education Dr.Panida Marungruang and other teachers undeclared to help facilitate data collection.

References

- [1] Driver, R. 1989. "Students' conceptions and the learning of science". **International Journal of Science Education**. Vol. 11, pp. 481-490.
- [2] Assessment.aaas.org [Internet]. New York: AAAS Science Assessment 2008 [update 2016 Feb 24; cited 2015 Nov 5]. Available from: [http:// Assessment.aaas.org/](http://Assessment.aaas.org/).
- [3] Anderson, L.W., Krathwohl, D.R., Airasian, P.W., Cruikshank, K.A., Mayer, R.E., Pintrich, P.R., Raths, J., Wittrock, M.C. 2001. "A Taxonomy for Learning, Teaching, and Assessing: A revision of Bloom's Taxonomy of Educational Objectives." **New York: Pearson**. Allyn & Bacon.
- [4] Kanajanawasi, S. 2013. "Classical Test Theory"

CU Publishing

Preparation of Glass-Ceramic Materials from Glass Powder Compacted

N. Kulrat¹, S. Dangtip^{1,2*}, and D. Bootkul³

¹Department of Physics, Faculty of Science, Mahidol University, Bangkok, 10400, Thailand

²NANOTEC Center of Excellence, Faculty of Science, Mahidol University, Bangkok 10400, Thailand

³Department of General Science, Faculty of Science, Srinakharinwirot University, Bangkok, 10110, Thailand

*E-mail: somsak.dan@mahidol.edu

Abstract

Glass-Ceramics is known to have very good mechanic properties while combining good properties from glass or ceramics which otherwise having them separately. Such good mechanic properties allow machining to any desirable shape or form, which is important for ornament and garnishment. In this work, soda lime glass powder (SLG), combining with other precursor such as SiO₂, TiO₂, and pigment oxide powders, was prepared. Weight composition of SLG-SiO₂-TiO₂-Pigment oxide, prepared by conventional melt-quenching technique, was investigated. The thermal profile of glass transition and crystallization were studied by differential scanning calorimetry (DSC). The crystal structure of the sintered glass-ceramics was carried out by X-ray diffraction (XRD). The results show that devitrification of this glass system leads to glass-ceramics material. Its application in artificial opal gemstone work is foreseen.

Keywords: Differential scanning calorimetry (DSC), Glass-ceramics, Soda lime Glass (SLG), X-ray diffraction (XRD)

Introduction

Nowadays, the majority of people on earth is using glass bottles in a rate in which the bottles themselves are not able to degrade fast enough thus, creating a hefty amount of unused and devalued glass bottles. There is also an increasing quantity of waste, which take long time to decompose and affects the pollution problem [1]. Most of glass bottles are collective called soda lime glass (SLG) because they have an amount of SiO₂ over 70%. Na⁺ terminate the network of SiO₂ glass as a result SLG has low softening point and easy to shaping at low temperature than the other glass type [2]. There are quite a few methods to reuse or recycle the SLG waste to have value added products.

Glass-ceramic (GC) materials are produced by controlling crystallization crystal on base glass; consisting of crystalline and amorphous phase. The GC

materials also retains good properties from glass and ceramics such as hardness, transparency, chemical durable, etc. Development of glass-ceramics by processing of silicate waste have been interesting since 50 years ago [3]. SLG has been employed as one candidate in this processing by adding some nucleating agent (e.g., Pt, Ag, TiO₂) for the precipitate nucleation process and control crystallization during sintering process.

Powder compacted method is one route of GC processing. Typically it works by mixing base glass powder as very small size and nucleating agent powder including other glass granule powder before compressing with high pressure for densification. The next step is to sinter for crystallization of glass at the pre-defined temperature, which was suggested by differential scanning calorimetry (DSC). This has been reported as a very useful method to investigate the

crystallization temperature of glassy material including the kinetic of non-isothermal parameter [4].

D. Bootkul et al [5] have carried out studies of glass-ceramic composite to synthesis artificial new type of Turquoise and Opal gemstone produced from SLG by powder compacted process, Their products have good mechanical, physical, and optical, which can lead to costume jewelry application and has feasibility to retain its natural counterpart look comparable real.

In this work, we aim to study the effect of sintering temperature on the crystallization process and to find an optimum condition for glass-ceramics production to serve the above mentioned perspective.

Materials and Methods

SLG powder was obtained by milling the glass bottle on the ball mill machine, the powder was sieved by a 44 μm mesh.

The simultaneous differential scanning calorimetry SC and thermal gravitational analysis (TGA) (SDT2960) were carried out using 12-15mg of SLG powder samples heated in alumina crucible in air from room temperature to 800°C with three heating rates ($\beta = 5, 10, 15 \text{ }^\circ\text{C}/\text{min}$). The data were analyzed by OriginPro 8.6 software to find peak position for determine peak crystallize temperature including draw the baseline for fitting Gaussian curve on exothermic peak.

The glass samples were prepared by mixing 60SLG-35SiO₂-2TiO₂-2ZnO-0.34CuO-0.33MnO₂-0.33FeO (by%weight) of these composition. Then the mixture powders were uniaxial pressed at 10 Tones for 10 minutes to obtain a cylindrical pellet with a diameter of 13 mm and of about 10 mm high. After that sintered samples at difference temperature at 711, 800, 850, 900, 950, and 1,000°C in electric furnace by a heating rate of 5°C/min. The samples were at sintering temperature for 2 hr. The samples were then left to quench in air.

The crystal structure was carried out by X-ray diffractometer (XRD, Bruker D8Advance) using CuK α

radiation as the X-ray source. Diffraction pattern was collected from 20°-80°.

Samples microstructure was investigated using a scanning electron microscope (SEM). The samples were coated with gold prior to SEM measurements.

Results and Discussion

DSC curve for heating rate $\beta = 5^\circ\text{C}\cdot\text{min}^{-1}$ is shown in Figure 1. An exothermic peak is clearly observed at $T_p=711.57^\circ\text{C}$. The exothermal peak at different temperature was also observed at the other heating rates as summarized in Table1. It is noted that the exothermic temperature increases with an increasing heating rate. Also shown in the same figure is the TGA and its derivative. There are two sudden drops in sample weight at 80°C and 418.08°C. the latter is understood as glass transition temperature (T_g)(~418.08°C). Before reaching the exothermic temperature the SLG glass has its structure fully in amorphous phase. When the temperature is greater than T_g , the mixture undergo a super cooled liquid state. At about the exothermic temperature T_p , the mixture is giving away its excessive energy to crystallize effectively. This temperature was then chosen for sintering process. Beyond the exothermic temperature, the mixture is gradually reaching its molten state at which point the mixture crystallinity becomes less and gradually decreasing with increasing temperature.

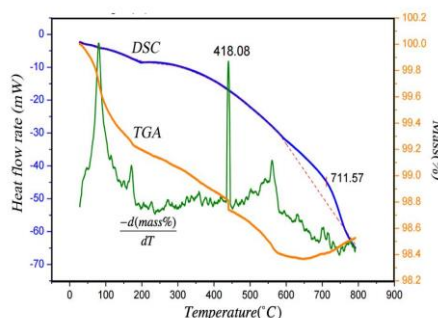


Figure1 DSC (blue curve) and TGA (brown curve) and TGA derivatives (green curve) of SLG with heating rate $\beta = 5^\circ\text{C}\cdot\text{min}^{-1}$

The XRD pattern of the sample before and after sintering at various sintering temperatures are shown in Figure 2. The sample is found in an α -SiO₂ phase coming mainly from SiO₂ in the mixture.

Table 1 Exothermic temperature observed different heating rates

B (°C.min ⁻¹)	T _p (°C)
5	711.57
10	727.07
15	737.13

The degree of crystallinity is decreasing with increasing sintering temperature. The β -SiO₂ started to be observe with the sintering temperature reaching 1000°C. This is in connection to the appearance of the glass-ceramics phase. Figure 3 compares the XRD pattern of the product before and after sintering at 1000 °C. In fact the dominance of the β -SiO₂ phase over the α -SiO₂ is clearly noted. Figure 4 shows the relative intensity of the (100) to the (101) planes ΔI_r of the α -SiO₂ phase (as blue line).

$$\Delta I_r = 1 - \frac{I_1}{I_0} \quad (1)$$

Plane (101) intensity becomes relatively less and less with the increasing sintering temperature. .

With XRD pattern one can also calculate mean crystalline size (L) with in the sample using the the highest intensity peak and Scherrer formula [6]

$$L = K\lambda/\alpha\cos\theta, \quad (2)$$

where K is constant, λ is the wavelength of X-ray, α is the full width at the half maximum and θ is diffraction angle. In average, the crystallize size become finer with increasing sintering temperature, the mean size drop by a factor of two after sintering at 1000°C compare to the un-sintered powder.

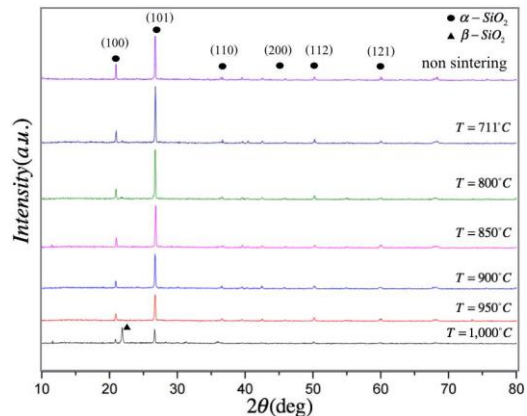


Figure 2 XRD pattern of product obtained with various sintering temperatures.

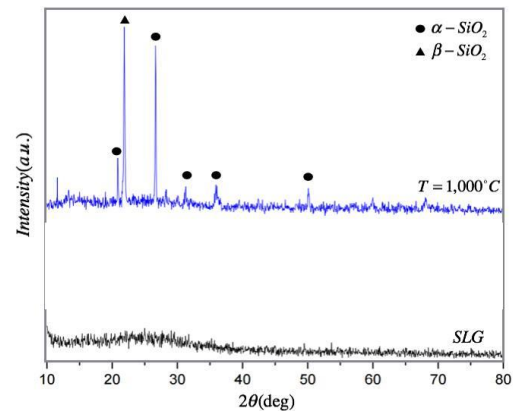


Figure 3 XRD pattern of the SLG and the 1000°C sintered samples.

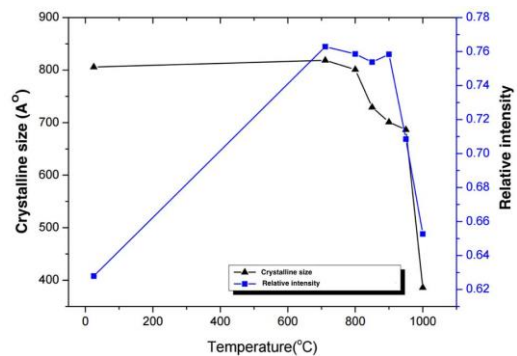


Figure 4 Crystalline size and relative intensity of the (100) to the (101) plane versus sintering temperature.

Conclusion

The thermal behavior of SLG was investigated by DSC. This is useful for the synthesis glass-ceramics. The crystal structure analysis by XRD technique have also confirmed the temperature where the glass-ceramics start to appear. In this work, glass-ceramics can be successfully produced from the recycled SLG.

Acknowledgment

The financial support for this project was provided by Development and promotion of science and technology talents project Scholarship (DPST).

References

- [1] S. Mishra¹ , D. Majid , B. Krishna and P. Tripathy 2013. "Impact of glass industries on renewable energy".International Journal of Environmental Science. Volume 4 No.3, 43-47.
- [2] C. Lyon 1974. "Prediction of the Viscosities of Soda-Lime Silica Glasses". A. Physics and Chemistry. Volume 78A, No.4, 497-524.
- [3] R.D. Rawlings, J.P. Wu and A.R. Boccaccini, 2006."Glass-ceramics: Their production from wastes-A review", J mater sci 41, 733-761.
- [4] M. Ghasemzadeh, A. Nemati, A. Nozad and Z. Hamnabard. 2011. "Crystallization kinetics of glass-ceramics by differential thermal analysis", Ceramics-Silikaty, Volume55 ,No.2, 188-194.
- [5] D. Bootkul P.Chaweewanpakdee, T. Tammapirom and P. Sawasdee. 2013. "A study of glass-ceramic composite to new type of turquoise jewelry".7thSrinakhalinvirot University international conference proceeding.
- [6] L. Alexander and H.P Klug. 1950. "Determination of crystallite size with X-Ray Spectrometer". Journal of Applied Physics. Volum21, No.137, 137-142.

Effect of Low Pressure Plasma on Brown Rice

W. Arworn¹, S. Khamrat², W. Chaiwat³, R. Wongsagonsup², M. Suphantharika⁴ and S. Dangtip^{1,5,*}

¹Department of Physics, Faculty of Science, Mahidol University, Bangkok, 10400

² Food Technology program, School of Interdisciplinary studies, Mahidol University, Kanchanaburi Campus, Kanchanaburi, 71150

³ Environmental Engineering and Disaster Management Program, School of Interdisciplinary studies, Mahidol University, Kanchanaburi Campus, Kanchanaburi, 71150

⁴Department of Biotechnology, Faculty of Science, Mahidol University, Bangkok, 10400

⁵ NANOTEC Center of Excellence, Faculty of Science, Mahidol University, Bangkok, 10400

*E-mail: somsak.dan@mahidol.edu

Abstract

Low pressure plasma is one of the most widely used mechanisms for processing materials especially to modify their surface properties. The application of low pressure plasma in agricultural sector has also been realized. In this research, low pressure plasma was generated at radio-frequency and about 2.0 mbar in a vertical plasma reactor. The reactor is to facilitate plasma treatment of very short plasma residence time (0.1 s). This low pressure plasma has then been applied to treat a whole grain of pigmented or brown rice. We have also studied this effect on white rice as a comparison. It has been found that low pressure plasma have significantly reduced an optimal cooking time, lowered moisture content and promoted water absorption. The rheological property, using rapid-visco analysis, has indicated further significant changes in peak viscosity, setback and enthalpy ΔH after plasma treatment. SEM images show the plasma treatment has caused the rice grain surface to be more porosity.

Keywords: Low pressure plasma, Brown rice: rapid-visco analysis, Texturing properties, Cooking times

Introduction

Radio-frequency discharge is one of the most widely used discharge types in various applications such as etching, deposition, surface modification, sterilization, etc. It allows us to produce a large volume of stable plasma [1]. In inductively coupled plasma (ICP), RF power is transferred to the working gas to generate plasma by inductively coupling associated with electromagnetic [2]. Such process to generate low pressure plasma processing technology in connection with the downer reactor for plasma surface treatment of material [3][4]. It removes material from the surfaces by chemical reactions and physical etching at the surface

[5]. This work introduces a plasma treatment of brown rice.

Rice (*Oryza sativa* L.) is the most widely consumed staple food for a large part of the world's human population. The whole grain rice consists of a hull, bran rice, germ and endosperm. Rice bran is a good source of protein, lipids, fiber and mineral. These layers were removed during the milling process [6]. This fact has widely been realized the higher nutritional value in brown rice. It is interesting that these layers affect the different properties after the plasma treatment [8].

In this work, we applied low pressure and inductive coupled plasma reactor at 13.56 MHz to rice

grain to investigate how different effects of low pressure plasma treatment on physical and cooking properties of untreated rice, vacuum treated rice and plasma treated rice for each type of rice (white rice and brown rice).

Materials and Methods

Rice sample

White rice (Kor Khor type 47) and Riceberry rice were gathered from Suan Dusit rice mill (Prachinburi, Thailand) in 2015, and Jasmine brown rice (Green Niche brand) from LH Rice International Co., Ltd. (Nakhonpathom, Thailand).

Exposure of rice to low pressure plasma

The low pressure plasma system that was shown in Figure 1 comprised the following parts. Plasma is generated in quartz tube with a diameter of 38 mm and length of 30 cm. A 10-turn spiral coil is mounted around the tube with a vertical coil length of

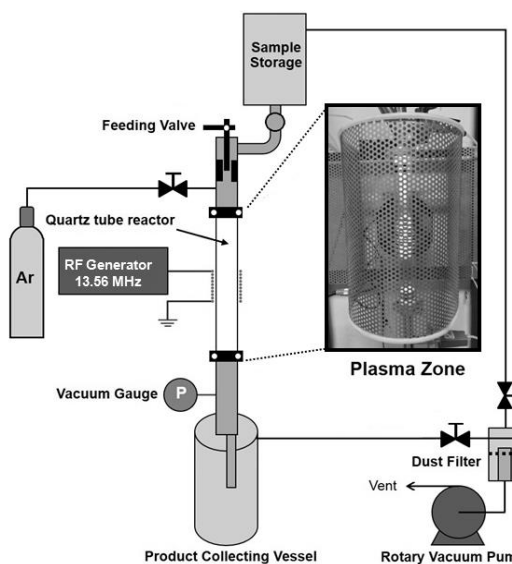


Figure 1 Schematic set up of plasma system

a RF generator at 13.56 MHz. The applied power was around 100 W. High purity argon was used to generate plasma with the flow rate of 15 sccm. The gas to generate plasma is high purity argon. Working pressure was 2-3 mbar. Rice samples (100g) were taken in

sample storage. Sample was allowed by feeding valve passed through the center of discharge tube to a product collecting vessel. The experiments were repeated from 1 and 5 times for white rice and brown rice, respectively. Henceforth, they were referred to plasma treated rice. Another set of rice grain were repeated but without igniting plasma. They were then referred to vacuum treated rice.

Cooking properties

Optimal cooking time

Rice samples (2g) were cooked. The cooking time was determined by removing at different time intervals during cooking and pressing them until no white core was left.

Water uptake ratio

Rice samples were cooked at the optimal cooking time. The samples were drained and weighed. The water uptake ratio was calculated.

Solid loss

Rice samples were cooked at the optimal cooking time. The samples were evaporated at 110°C until completely dry. The solids were weighed.

Expansion ratio

The total length, width and volume of cooked rice at the optimal cooking time was divided

Texture properties

Texture Profile Analysis (TPA) is a double compression test for determining the textural properties. The TPA test mimics the mouth's biting action.

Pasting properties

Pasting viscosity profiles were analyzed using a Rapid Visco Analyzer (RVA). Rice was ground into flour. The measurement was held at 50°C for 1.5 min, raised to 95°C at 10°C/min, held for 4.5 min, cooled to 50°C at 10°C/min and held for 10 min. The peak viscosity (PV), holding strength (HS) and final viscosity (FV) were recorded. The different between HS and PV or FV express as breakdown (BD) or setback (SB), respectively.

Thermal properties

The thermal properties of rice flour were measured using differential scanning calorimeter (DSC). Onset temperature (T_o), peak temperatures (T_p), conclusion temperatures (T_c) and enthalpies (ΔH) were determined.

Scanning electron micrograph (SEM)

To investigate effect of plasma on rice surface, we have used SEM for analysis. The samples were sputter coated with gold prior to the analysis. The results were investigated any effects on the rice surface. The images were taken at 1000x magnification.

Statistical analysis

The significant differences among were analyzed with the ANOVA by Duncan's multiple range test from SPSS software version 22. ($P < 0.05$)

Results and Discussion

Cooking properties

Brown rice has a longer optimal cooking time than white rice because of bran layer. Plasma treatment for WR, BR and RB significantly decreased the optimal cooking time to 19.5, 24.0 and 25.5 min, respectively (Table 1). There were not different between vacuum treatment and plasma treatment for WR because of bran layer, compared with BR and RB. The reduced optimal cooking time due to higher water uptake and surface area condition of the grain results in water diffusion and starch gelatinization. When the bran layer was cracked, moisture can penetrate to endosperm and reduce the optimal cooking time.

Texture properties

The texture of cooked rice was shown to determine by consumers when it is consumed. The hardness, adhesiveness and chewiness value of cooked rice were significantly decreasing after plasma treatment which is important parameter for the evaluation of cooked rice texture. But cohesiveness and springiness were not significantly different.

Table 1 Cooking properties and texture properties of brown rice

	Sample								
	WRunt	WRvac1	WRpm1	BRunt	BRvac5	BRpm5	RBunt	RBvac5	RBpm5
Moisture (%)	9.73±0.09 ^a	7.58±0.06 ^b	7.14±0.12 ^c	9.23±0.00 ^a	8.11±0.15 ^b	7.15±0.05 ^c	8.30±0.14 ^a	7.87±0.28 ^b	7.33±0.29 ^b
<i>Cooking properties</i>									
Cooking time (min)	19.50±0.70 ^a	16.00±0.00 ^b	16.00±0.00 ^b	27.00±0.00 ^a	26.50±0.70 ^a	24.00±0.00 ^b	29.00±0.00 ^a	29.00±0.00 ^a	25.50±0.70 ^b
Water uptake. (%)	189.63±6.93 ^c	242.14±0.91 ^b	262.03±3.29 ^a	125.87±4.22 ^b	161.04±0.49 ^b	158.21±0.29 ^a	124.18±5.20 ^b	138.65±1.63 ^a	129.68±2.57 ^{ab}
Solid loss (g)	4.21±0.32 ^a	5.74±0.37 ^a	4.47±0.69 ^a	3.48±0.00 ^a	4.22±0.37 ^a	4.24±0.34 ^a	4.99±0.72 ^a	4.99±0.02 ^a	4.49±0.72 ^a
Elongation ratio	-	-	-	1.11±0.04 ^b	1.14±0.00 ^b	1.09±0.04 ^a	1.07±0.03 ^b	1.11±0.02 ^a	1.08±0.00 ^a
Width expansion	-	-	-	1.77±0.03 ^a	1.79±0.03 ^a	1.84±0.09 ^a	1.66±0.07 ^a	1.79±0.02 ^a	1.78±0.02 ^a
Volume expansion	1.21±0.00 ^b	1.30±0.05 ^{ab}	1.32±0.021 ^a	1.12±0.00 ^c	1.18±0.04 ^a	1.15±0.00 ^b	1.15±0.021 ^a	1.18±0.00 ^a	1.15±0.021 ^a
<i>Texture properties</i>									
Hardness (g)	1233.10±36.57 ^a	780.36±49.46 ^b	644.44±23.19 ^c	963.30±32.81 ^a	830.37±43.36 ^b	664.73±36.33 ^c	913.63±34.13 ^a	752.43±30.10 ^b	590.53±35.60 ^c
Adhesiveness (g/s)	2.11±0.61 ^a	1.72±0.60 ^{ab}	1.02±0.31 ^b	2.17±0.18 ^a	2.20±0.18 ^a	1.61±0.23 ^b	5.53±1.81 ^a	2.32±1.59 ^{ab}	3.30±1.51 ^b
Cohesiveness	0.36±0.02 ^a	0.30±0.01 ^c	0.33±0.03 ^b	0.37±0.04 ^a	0.33±0.02 ^b	0.31±0.04 ^a	0.29±0.01 ^b	0.20±0.01 ^c	0.31±0.05 ^a
Springiness	0.74±0.03 ^a	0.75±0.10 ^a	0.75±0.05 ^a	0.64±0.15 ^a	0.50±0.05 ^a	0.58±0.86 ^a	0.53±0.03 ^a	0.54±0.02 ^a	0.52±0.02 ^a
Chewiness	329.74±20.78 ^a	174.54±29.81 ^b	160.07±79.11 ^b	229.88±36.75 ^a	137.85±18.55 ^b	118.86±16.17 ^b	116.46±9.43 ^a	87.34±6.00 ^b	79.41±14.85 ^b

Different letter for the same row indicate statistical difference ($P < 0.05$). All abbreviation is presented in table 1, WRunt; untreated white rice, WRvac1; 1 cycle vacuum treated white rice, WRpm1; 1 cycle plasma treated white rice, BRunt; untreated brown rice, BRvac5; 5 cycles vacuum treated brown rice, BR-plasma5; 5 cycles plasma treated brown rice, RBunt; untreated Riceberry, RBvac5; 5 cycles vacuum treated Riceberry, RBpm5; 5 cycles plasma treated Riceberry

Table 2 Pasting and thermal properties of rice flour

	Flour								
	WRunt	WRvac1	WRpm1	BRunt	BRvac5	BRpm5	RBunt	RBvac5	RBpm5
<i>Pasting properties</i>									
PV	40.17±0.71 ^b	42.46±1.47 ^b	48.38±0.53 ^a	77.91±0.12 ^b	87.04±1.47 ^a	89.17±0.94 ^a	42.96±1.24 ^b	45.92±0.83 ^a	46.00±0.00 ^a
HS	38.17±0.00 ^b	41.38±2.06 ^b	47.17±0.12 ^a	59.42±0.35 ^b	67.00±1.06 ^a	69.46±1.12 ^a	32.71±0.41 ^b	35.04±1.36 ^{ab}	35.79±0.60 ^a
BD	2.00±0.71 ^a	1.09±0.59 ^a	1.21±0.41 ^a	18.50±0.47 ^a	20.04±2.53 ^a	19.71±0.18 ^a	10.25±0.82 ^a	10.88±0.53 ^a	10.21±0.57 ^a
FV	74.75±0.47 ^c	78.09±0.12 ^b	87.29±0.30 ^a	150.75±0.95 ^b	167.05±2.30 ^a	165.63±0.88 ^a	91.00±0.24 ^b	95.21±2.18 ^a	95.03±3.66 ^a
SB	36.59±0.47 ^a	36.71±2.18 ^a	40.13±0.18 ^a	91.34±0.59 ^c	100.05±1.24 ^a	96.17±0.23 ^b	58.30±0.18 ^c	60.17±0.83 ^b	63.08±0.35 ^a
<i>Thermal properties</i>									
T_g (°C)	60.66±1.26 ^a	60.13±0.31 ^a	60.17±0.70 ^a	64.36±0.19 ^a	64.68±0.30 ^a	64.52±0.22 ^a	66.22±0.22 ^a	66.67±0.25 ^a	66.53±0.16 ^a
T_p (°C)	77.92±0.12 ^a	77.50±0.24 ^a	77.50±0.47 ^a	71.83±0.00 ^a	72.00±0.24 ^a	72.09±0.18 ^a	77.83±0.00 ^a	73.92±0.12 ^a	73.86±0.12 ^a
T_c (°C)	85.41±0.06 ^a	84.56±1.12 ^a	85.09±0.19 ^a	79.35±0.20 ^a	79.27±0.18 ^a	79.14±0.16 ^a	81.14±0.17 ^a	81.08±0.03 ^a	81.16±0.46 ^a
ΔH	10.88±0.06 ^a	10.90±0.03 ^a	10.44±0.00 ^b	10.74±0.03 ^a	10.82±0.08 ^a	9.98±0.08 ^b	10.10±0.03 ^a	10.16±0.06 ^a	9.10±0.03 ^b

Different letter for the same row indicate statistical difference ($P < 0.05$). All abbreviation is presented in table 2. PV; peak viscosity, HS; holding strength, BD; breakdown, FV; final viscosity, SB; setback.

Pasting properties

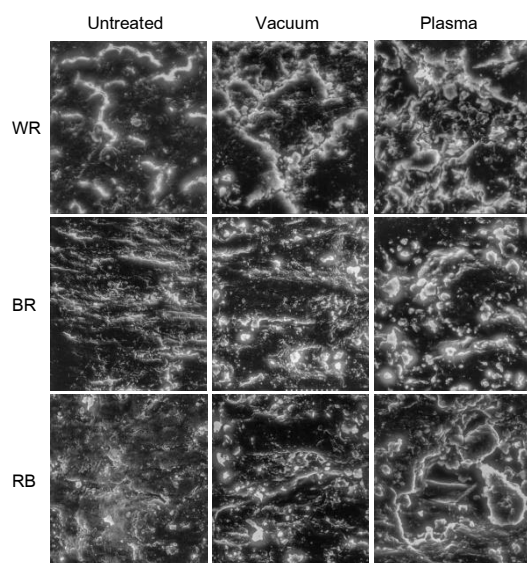
The pasting profile of rice flours were shown in Table 2. Vacuum and plasma treatment increase all RVA parameter, such as peak viscosity and setback, were significantly influenced by plasma treatment. With increasing heat treatment, the starch structure absorbs water and start to swell, cause the viscosity to increase. They might due to the partial destruction of fibrous materials by plasma treatment. The starch granules were then swollen easier.

Thermal properties

Thermal characteristics of rice flour are shown in Table 2. During gelatinization, all samples show similar T_g and T_p . ΔH (enthalpy change of gelatinization) were decrease after plasma treatment, the decreases indicated that less energy is required for partial gelatinization in rice flour.

Scanning electron microscope

SEM images of rice surface are shown in Figure 2 at 1000x magnification. After plasma treatment, the entire surface looks rough. This should support the lower optimal cooking time of the plasma treated rice.

**Figure 2** SEM images of rice grain

Conclusions

This work has shown that plasma treatment has effectively improved physical and cooking properties. The interactions of plasma treatment caused surface become cracked. After plasma treatment, the plasma treated rice absorbed water easier than the untreated rice. There is lower moisture content. The optimal cooking time was reduced by 3 min and the plasma treated cooked rice become softer. The significant difference in peak viscosity, setback and gelatinization enthalpy ΔH of rice flour were clearly observed. Changes in structure of outer layer demonstrated the effect of plasma treatment were clearly visible under SEM analysis.

Acknowledgments

The author would like to thank the Development and Promotion of Science and Technology Talents Project (DPST) and Mahidol University for financial support, and Suan Dusit Rice Mill for material support.

References

- [1] Hopwood, J. 1992. "Review of Inductively Coupled Plasma for Plasma Processing". **Plasma Source Sci. Technol.**1: 109-116.
- [2] Matsuharu, K. 2005. **Plasma Techniques for Film Deposition**. Alpha Science.
- [3] Arpagaus, C., Sonnenfeld, A. and Rudolf, P.H. 2005. "A Downer Reactor for Short-time Plasma Surface Modification of Polymer Powders". **Chem. Eng. Technol.**28: No. 1.
- [4] Arpagaus, C., Rossi, C. and Rudolf, P.H. 2005. "Short-time plasma surface modification of HDPE powder in a Plasma Downer Reactor- process, wettability improvement and ageing effect". **Applied surface science**.252: 1581-1595.
- [5] Chan, C. M., Ko, T. M. and Hiraoka, H. 1996. "Polymer surface modification by plasma and photons". **Surface Science Reports**.24: 1-54.
- [6] Saunders, J. Izydorczyk, M. and Levin, D. B. 2011. **Economic Effects of Biofuel Production**. InTech Public.
- [7] Christou, P. 1994. **Rice Biotechnology and Genetic Engineering**. Technomic Public.
- [8] Chen, H. H. 2014. "Investigation of Properties of Long-grain Brown Rice Treated by Low-pressure Plasma". **Food Bioprocess Technol.**7: 2484-2491.
- [9] Chen, H. H., Chen Y. K. and Chang, H. CH. 2012. "Evaluation of Physicochemical Properties of Plasma Treatment Brown Rice". **Food Chemistry**.135: 74-79.
- [10] Sarangapani, C., Devi, Y., Thirundas, R., Annapure, U. S. and Deshmukh, R. R. 2015. "Effect of low-pressure plasma on physico-chemical properties of parboiled rice". **Food Science and Technology**.63: 452-460.
- [11] Thirundas, R., Deshmukh, R. R. and Annapure, U. S. 2015. "Effect of low temperature plasma processing on physicochemical properties and cooking quality of basmati rice". **Innovative Food Science & Emerging Technologies**.31: 83-90.
- [12] Tuner, M. M., Lieberman, M. A. 1999. "Hysteresis and the E-to-H transition in radiofrequency inductive discharges". **Plasma Source Sci. Technol.**8: 313-324.
- [13] Lieberman, M. A., Lichtenberg, A. J. 1994. **Principle of Plasma Discharges and Material Processing**. New York: Wiley.

Characteristics of Daytime Penetration Electric Field in Equatorial Ionosphere during Recurrent Geomagnetic Storms

T. Yeeram¹, T. Laosuwan¹, P. Thammasaeng¹, and S. Aukkaravittayapun²

¹Department of Physics, Faculty of Science, Mahasarakham University, Kamreang, Kantarawichai, Maha Sarakham, 44150

²National Astronomical Research Institute of Thailand (Public organization)

*E-mail: thana.thana@hotmail.com

Abstract

Effects of recurrent geomagnetic storms (RGSs) induced by corotating interaction regions (CIRs) and high-speed solar wind streams (HSSs) on variations in daytime equatorial electric field (EEF) have been investigated. The EEF data as derived from magnetometer data together with the solar wind plasma data reveal events of striking long duration of short-lived prompt penetration electric fields (PPEFs) about 7-12 hours. The PPEFs exhibited different characteristics depending on the transient effects in CIRs and HSSs. The RGSs cause PPEF mainly in the main phase of storms and not all the RGS exhibited penetration of electric field into the ionosphere. Particularly, in some events, PPEF is terminated in the main phase at shocks in association with the depression of the solar wind pressure in CIRs. The turning of magnetic field B_z to the south in the main phase of the magnetic storms are associated with the PPEF in the dayside equatorial ionosphere and the fluctuations in IMF B_z are associated with transient PPEFs. Some HSSs cause High-Intensity Long-Duration Continuous AE Activity (HILDCAA) that can last for a few to 27 days. The major contribution to the AE increases are AL decreases due to westward electrojet intensifications in the HILDCAAs events that satisfy the overshielding condition.

Keywords: Geomagnetic storms, Penetration electric field, Shielding, Corotating interaction region

Introduction

During magnetic storms, magnetospheric electric fields at high-latitudes can propagate across magnetic field lines to reach the equatorial ionosphere almost simultaneously [1,2] which are known as prompt penetration electric fields (PPEFs). PPEFs cause a perturbation in the zonal electric field during storm main phases [3-9] as a result of the temporary failure of the so called shielding mechanism [10]. The mechanism is caused by temporary imbalance between higher latitude region 1 (R1) and lower latitude region 2 (R2) large-scale field align currents

(FACs) [11] lasts from a few minutes to several hours [6]. The PPEF communicates with the ionosphere through R1 FAC in the polar cap, while a shielding electric field communicates with R2 FAC. Under a steady state, the R2 FACs tend to minimize the electric field at low latitudes, producing the shielding electric field due to the charge accumulation (the polarized electric field) in the ring current or the Alfvén layers [12,13].

The terms “undershielding” and “overshielding” are defined when the convection electric field is larger and smaller than the shielding electric field,

respectively. When a rapid southward turning of the z -component of the interplanetary magnetic field (IMF B_z) impinges on the magnetosphere, the R1 FAC suddenly increases, while the R2 FAC has to spend a long time for the gradual charge accumulation to balance the enhanced R1 FAC. Therefore, the dawn-to-dusk (duskward) electric field has time to penetrate into the low latitude ionosphere as an eastward electric field on the dayside before the R2 FAC is fully developed, in the case of undershielding. In contrast, the overshielding results from a sudden weakening of the strong convection field during a transition from southward to northward of the IMF B_z , which causes a temporarily strong R2 FAC. The dusk-to-dawn electric field can penetrate to low latitudes, resulting in a westward electric field on the dayside [11] until the shielding layer and overall magnetospheric configuration readjust. The time scale for the shielding processes is typically less than 1 h [4,14], but it depends on magnetospheric conditions [12,15].

One of the most important topics in the study of low latitude storm electrodynamics is their complex spatial and temporal variability [16]. Complex perturbations with a broad range of time scales during geomagnetic storms often occur in the low-latitude ionospheric plasma drifts and currents that relate to the PPEF as a signature of magnetospheric - ionospheric coupling. In addition to the convection electric field, the solar wind pressure is another important factor that affects the magnetospheric reconfiguration and development of R2 FAC, which in turn affect the undershielding and overshielding processes. A distortion of the plasma sheet inner edge by magnetospheric compression is associated with the sudden commencement that temporarily disrupts the R2 FAC [17]. Enhancements of the solar wind pressures can drive coherent increases of the penetrated electric field in the dayside equatorial ionosphere during stable and southward IMF B_z [18,19]. In contrast, the large decrease of the ram pressure can drive magnetospheric reconfiguration

and overshielding [20,21]. However, the interplay of the solar wind pressure and the IMF B_z in driving of PPEFs is not completely understood.

Recurrent geomagnetic storms (RGSs) emerge from interaction of the magnetosphere with a complex stream structure that corotates with the Sun of about 27 days, in the interplanetary space. RGSs are the most important storms during the declining and rising phases of the solar sunspot cycle. The corotating stream structure comprises of high speed solar wind streams (HSSs) and corotating interaction regions (CIRs). When the expanding HSSs from coronal holes interact with slow-speed up streams, CIRs are formed near the ecliptic plane with intense magnetic field and plasma. When the relative speed gradients are sufficiently large, typically at 2-3 AU, the CIRs are bounded by a forward shock and a reverse shock.

CIRs and HSSs are responsible for weak-to-moderate geomagnetic activity/disturbance at Earth with a period of about synodic 27 days [22]. Increases in the solar wind ram pressure according to the high density plasma cause increases in Earth's magnetic field H (horizontal) component as detected by near-equatorial ground-based magnetometers, or storm initial phases prior to the storm main phases. Negative interplanetary magnetic field B_z components (IMF B_z) of large-amplitude (nonlinear) Alfvén waves within some HSSs lead to High-Intensity Long-Duration Continuous AE Activity" or HILDCAA that can last for a few to 27 days [23,24]. The HILDCAA is the most dramatic geomagnetic response to the HSSs. Kutiev et al. [25] provided a study of 27-day response of low-latitude ionosphere to the RGS in the recent solar minimum. A good brief of RGS and their ionospheric and thermospheric effects are provided [26]. The temporal and spatial dynamics of the PPEF in the equatorial ionosphere during RGSs are not completely understood because of the complex due to strong and fast variations of external drivers such as IMF, solar wind dynamic pressure, and intense particle precipitations in the magnetosphere that results in

strong variations of PPEF. Veenadhari et al. [27] investigated this type of magnetic storms on the equatorial and low-latitude ionosphere over Indian sector in 2006. They found PPEFs with lifetimes of 2–3 h and a correlation between variations of the equatorial electrojet (EEJ) and the sudden changes in the y -component of the interplanetary electric field (IEF E_y) around morning to noon hours. The purpose of this study is to examine characteristics of the penetration electric fields in the equatorial ionosphere during RGSSs. We used pairs of magnetometers in Peru and the solar wind plasma data to study the variability of the equatorial PPEF during the RGSSs and HILDCAA events. Particularly, results indicate that the daytime variability is significantly associated with the transient effects in the CIR/HSS-induced geomagnetic storms.

Materials and Methods

Observational data

The CIR-induced geomagnetic storms were characterized using 1-hr-averaged solar wind plasma parameters obtained from the Advanced Composition Explorer (ACE) spacecraft, positioned at about 224 RE. The time shifted-data of about 1 h (to account for the delay from the ACE location to the bow shock) adjusted for the ACE parameters to match the ground magnetic data. The coordinate system used here is the geocentric solar magnetic (GSM). In this system, \mathbf{x} points radially outward from the Earth toward the Sun, $\mathbf{y} = \boldsymbol{\Omega} \times \mathbf{y} = |\boldsymbol{\Omega} \times \mathbf{y}|$, where $\boldsymbol{\Omega}$ is the south magnetic pole of the Earth, and \mathbf{z} forms a right-hand system. The solar wind parameters are as follows: the solar wind ram pressure is $2 \times 10^{-6} N V^2$ nPa (N and V are the solar wind number density in cm^{-3} and solar wind speed in km s^{-1} , respectively) and the IEF $E_y = -V B_z$. In addition, the 1-min-averaged field/plasma data made accessible through the Omniweb interface, which were shifted to the Earth's bow shock nose (BSN) already, were also used to investigate details of the CIR-induced geomagnetic storms. An additional

16 min [9] was added for the solar wind to travel through the magnetosheath, which matches the IEF E_y to the ionospheric electric field. The symH, asyD, and asyH magnetic indices were used as indicators of the level of geomagnetic activity. They are derived from magnetometer from 6 mid-latitude stations, which are randomly selected from a station group of 10 low- and middle-latitude stations in which only 2 are from low latitudes and are measures of the symmetric (sym) and asymmetric (asy) components of the ring current. Note that the asyH and asyD indicate to the asymmetric (partial) ring current and the strength of the R2 FACs, respectively.

We employed daytime (0700–1700 LT) ΔH data from the difference of horizontal (H) geomagnetic fields measured at pairs of stations in Peru, Jicamarca (11.9 N, 76.8 W; magnetic dip 2 N) and Piura (5.2 S, 80 W; magnetic dip 6.8 N), to infer the equatorial vertical drift $\mathbf{V} = \mathbf{E} \times \mathbf{B}/B^2$ and ionospheric electric field [28–33] where \mathbf{B} is $\sim 2.40 \times 10^{-5}$ T, the magnetic field strength obtained from the IGRF model for the Jicamarca site at 150 km altitude. Note the subtraction can eliminate both the global Sq current system and the Dst ring current component in H , resulting in a ΔH value that is only related to the ionospheric electrojet current and hence the east-west electric field. This method provided F region $\mathbf{E} \times \mathbf{B}$ drifts data based on ΔH ground-based Jicamarca-Piura Magnetometers, which are in good agreement with the radar measured 150-km and F-region Jicamarca drifts. It is noted that in the F-region, as collisions are so rare, ions and electrons move mostly under $\mathbf{E} \times \mathbf{B}$ drift. Note also that the strength of the dawn-to-dusk electric field is $\sim 0.5 \text{ mV m}^{-1}$ and is responsible for the upward $\mathbf{E} \times \mathbf{B}$ drift velocities of $\sim 20 \text{ m s}^{-1}$ measured by the Jicamarca ISR. To infer the eastward electric field (EEF), we used the vertical drift through the relationship $E = V B$. The method is based on the linearity between ΔH and the strength of the EEJ, which is linearly related to the the zonal EEF.

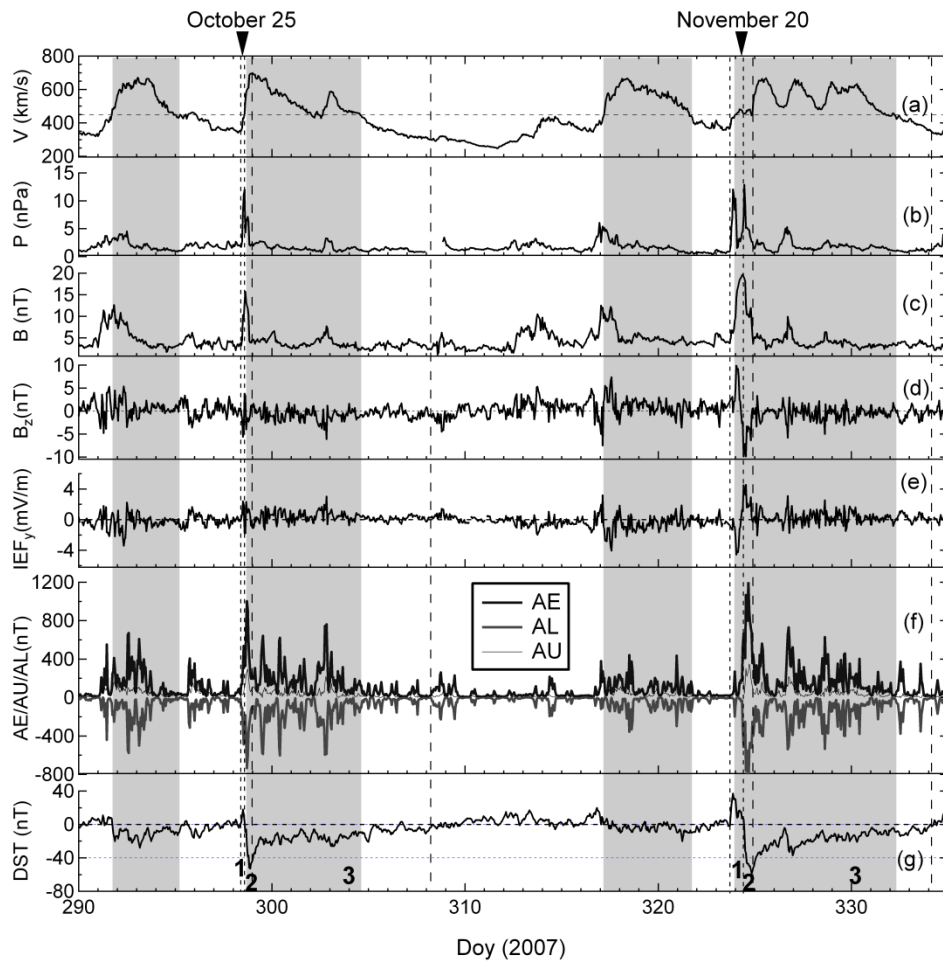


Figure 1 Recurrent geomagnetic storms associated with HSS-CIR in solar minimum condition during 2007 from 17 October to 1 December. (a) Solar wind speed. (b) Solar wind pressure. (c) Magnitude of magnetic field. (d) North/south magnetic field component. (e) Interplanetary electric field E_y component. (f) AE, AU, and AL indices. (g) Dst index. Shaded areas represent HSSs with solar wind speed $\geq 450 \text{ km s}^{-1}$. Numbers 1, 2, and 3 indicate the initial, main, and recovery phases of the storms, respectively.

Results and Discussion

Solar wind conditions and geomagnetic Responses

Here we provided a special case study of two CIR-induced geomagnetic storms as shown in Figure 1, to illustrate some characteristics of the magnetic storms. The two magnetic storms (indicated by the two arrows in the top) were recurrent as a result of the reappearance of a CIR. As will be described, a substantial penetration of electric field into the equatorial ionosphere occurred in the two storms

where interplanetary parameters highly fluctuated. The HSS regions (shading areas) lasted from six days to eight days with peaks of more than 600 km s^{-1} . Note another two CIRs/HSSs nearby exhibited low variations in the interplanetary parameters, which did not significantly disturb the geomagnetic activity.

The initial phases of the storms were located at the leading edges of the HSSs when the Dst index was positive (indicated by no. 1). The solar wind speed, pressure, and total IMF, IMF B_z , IEF E_y , and

Auroral Electrojet (AE), Auroral Upper (AU), and Auroral Lower (AL) indices suddenly increased. Note that peaks in the ram pressures corresponded to the rising of the Dst index. The IMF Bz exhibited large fluctuations with magnitudes more than 5 nT, especially in the November 25 event. The IEF Ey weakly fluctuated. The AE index increased and the Dst index moderately decreased. The features indicate that CIRs provided large bulks of pressure that induced abrupt increases in the geomagnetic responses. Note that the AE, AU, and AL indices used here are derived from geomagnetic variations in the H -component observed at selected (10-13) observatories along the auroral zone in the northern hemisphere. The AU and AL indices express the strongest current intensity of the eastward and westward auroral electrojets, respectively. The AE provides a global measure of auroral zone magnetic activity produced by enhanced ionospheric currents flowing below and within the aurora oval, the overall activity of the electrojets. The difference, AU minus AL, defines the AE index.

In the main phase, when the Dst index decreased to a minimum (indicated by no. 2), the solar wind speed, pressure, and total IMF, IMF Bz, IEF Ey as well as Dst indices maintained the high values. The features indicate that CIRs induced abrupt increases in the geomagnetic responses with weak to moderate levels. The main phases terminated after sudden drops in the parameters. Finally, in the long recovery phase when the Dst index increased (indicated by no. 3), the solar wind pressure and total IMF, IMF Bz, and IEF Ey in the HSS regions were low. The Dst indices increased to quiet levels in six to eight days. There were noticeable multiple pulses in the Dst index, which may correspond to the fluctuations in the IEF Ey. The AE index possessed high values and exhibited large variations in the HSS region as indicated by the shading. Note that the HSS regions also covered the main phases of the two storms.

Multiple short-lived electric field penetration: Case studies

The response in the EEF to the changes in the interplanetary plasma during the geomagnetic storms was examined by the identification of the PPEF through comparing the concurrent of the EEF with the IEF Ey during disturbed periods. The PPEF effects are strongest at the equatorial regions where the Earth's magnetic field is horizontal. Therefore, when the PPEFs are directed eastward, the $\mathbf{E} \times \mathbf{B}$ convection magnitudes are the largest [34] as well as the EEF. Near local noon, the variation in the background ionospheric electric field is assumed to be relatively small [35]. Therefore, the increment in the ionospheric electric field determines the PPEF. Though we have found many events of obvious signature in the short-lived penetration electric fields, two typical case studies that dayside EEFs possessed different characteristics and responses are presented here. The responses exhibited long-duration of oscillatory electric field penetration for more than 7 h to half a day. Although, the ionospheric EEF oscillated with the same period of ~ 0.5 to 2 h for the IMF Bz or IEF Ey, which is a typical event for IEF penetration to the low-latitude ionosphere [5,6,36], some cases exhibited remarkable complex spatial and temporal variabilities. The case studies are as follows:

- Case 1. October 25, 2007 event

During the daytime of October 25, the IEF Ey and EEF synchronously oscillated and had substantial variation from 1200 to 2000 UT (0700-1500 LT) in a HSS that covered the storm's initial, main, and recovery phases. The IMF Bz largely oscillated between the southward and northward with a period of ~ 1.5 h as shown in Figure 2. The time duration in the duskward IEF Ey was about 15 min to 1 h. The PPEFs can last only for ~ 30 min because of the shielding-overshielding effect. The short interval of < 1 h indicates that the R2 FACs do not have enough time to generate an effective shielding.

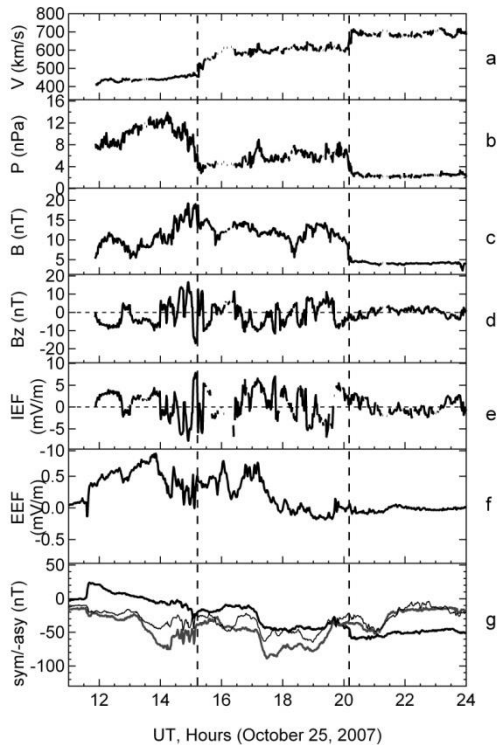


Figure 2 From top to bottom: (a) the solar wind speed, (b) ram pressure, (c) IMF magnitude, (d) IMF Bz, (e) dawn-duskward IEF Ey, (f) ionospheric electric field eastward (EEF) component, and (g) symH (thick black line) as well as the -asyH (thick gray line)/-asyD (thin black line). Two vertical dotted lines indicate the shocks in association with sudden drops in the ram pressure.

This case showed different aspect since there were two shocks and substantial fluctuation in the ram pressure in the main phase and between two shocks (indicated by dotted lines) at 1056 UT and 2000 UT, where the ram pressure tended to be anti-correlated with the EEF. Note that the solar wind pressure and IMF Bz were large, which is a typical profile in CIRs. The shocks were remarkable when the solar wind speed suddenly increased and the ram pressure and the IMF decreased. The pressure gradually decreased from 14 nPa to 3.5 nPa for the first shock, and suddenly decreased from 7 nPa to 2 nPa for the second shock. The first shock was associated with the

northward IMF Bz, while the second shock was associated with a decrease in southward IMF Bz. Moreover, both shocks were embedded in the main phase of the storm and in a CIR. The IMF Bz started to fluctuate adjacent to the CIR prior to the first shock that corresponded well with the sudden decrease in symH. The asyH was strongest at 1420 UT and 1730 UT suggesting the strong shielding there suppressed the PPEF. Note that the strong asyH occurred in the northward IMF Bz after the southward turnings of the IMF Bz by about 0.5-1 h. The EEF was suppressed close to a drop in the ram pressure between 1300-1500 UT prior to the first shock. The IMF Bz turned northward for 15 min at the first shock. It is noticeable that near first shock the PPEF was also suppressed, when the EEF was in an opposite direction to the IEF Ey for about an hour (see a consistency between the IMF Bz and the EEF as indicated by two vertical solid lines.) Moreover, the PPEF was strongly suppressed at the second shock in the evening. It is important to note that the second shock was associated with the reverse shock in the CIR, which is rarely identified near 1 AU. Behind the second shock, the fluctuations in the IMF Bz/IEF Ey were small and the signature of the PPEF disappeared. This suggests that the EEFs were affected not only by the fluctuation of the IMF Bz or IEF Ey, but also the variations in the ram pressure and the appearance of the shocks. The shock influenced the magnetospheric structure and reestablishment of the R2 FACs to shield the convection electric field.

- Case 2. November 20, 2007 event

As shown in Figure 3, this event included many fluctuations in the IMF Bz with amplitudes about 3-5 nT mostly in the south, which clearly associated with the high and rapid fluctuations of the Alfvén waves in the HSSs. The corresponding duskward IEF Ey was mainly in phase with the EEF during 1200 UT to 2200 UT. The IMF Bz oscillated with a period of ~0.5 h for more than 10 cycles. The solar wind speed and pressure were constant at about 480 km s⁻¹ and 4

nPa, respectively, during this interval. The PPEF was in the main phase with the minimum symH about -65 nT, a moderate storm. The asyH (R2 FAC) was strongest near the peak of the ram pressure and at the northward IMF Bz and then fluctuated to a lower value. This aspect occurred because the effects of IMF Bz were stronger than the low ram pressure. There were more significant fluctuations in the ram pressure in the initial phase than in the main phase of the storm. A small shock was observed at 2230 UT, as indicated by the dotted line. Behind the shock the fluctuations in the IMF Bz as well as the fluctuation in the IEF Ey were very small. The signature of the PPEF terminated behind the shock, where the Bz turned from the south to near zero. The peak of the solar wind pressure was low and the solar wind speed was nearly constant. Note that the solar wind pressure bulk was maintained for 2.5 h from 1000 UT to 1230 UT. The sudden drop in the ram pressure coincided with the small decrease in the EEF.

The results of this report are consistent with the shielding theory, when the short-lived pulses of the EEF exhibited PPEFs caused by the fluctuations in the IEF Ey/IMF Bz. The shielding electric field cannot cancel the PPEF because it (and the ring current) cannot fully develop during the short duration of the duskward IEF pulses. In other words, the ring current acts as a high pass filter of the IEF for periods less than a few hours [37]. We also observed PPEFs during initial and main phases of storms before the ring current was fully developed [6]. A fully developed, nearly symmetric storm-time ring current is more effective for shielding because the pressure gradient is associated with this well-developed hot pressure distribution in the inner magnetosphere. The injected particles can make a complete drift path around the Earth when the convection electric is reduced (small southward IMF Bz or IMF Bz northward turning that reduce energy flow).

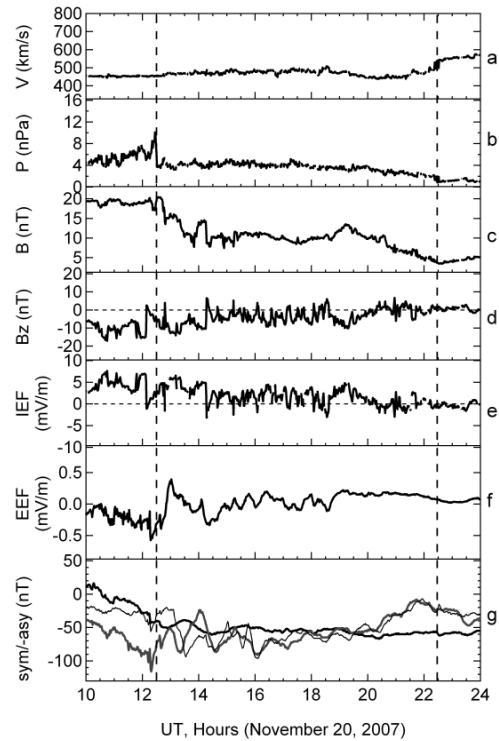


Figure 3 Same as Figure 2, but on 20 November 2007. Two vertical dotted lines indicate abrupt decreases in the solar wind pressure.

Since the partial ring current closes with the R2 FAC, when the partial ring current (asyH) was weak in the initial phase of CIR-induced magnetic storms, the R2 FAC was also weak during the compression of the magnetosphere. When the asyH increased in the main phase, in turn, the R2 FAC was expected to increase during the decompression of the magnetosphere. The increase of the R2 FAC (overshielding) generates the westward electric field; PPEF is suppressed. In general, the oscillating asyH was in trend with the asyD and exhibited a correlation with the EEF: when the EEF was increased (in southward IMF Bz), the asyH was reduced and when the EEF was decreased (in northward IMF Bz), the asyH was enhanced. The behaviors corresponded well to the shielding theory in relation to the R2 FACs. However, because of the low values of the asyH (the partial ring current) the R2 FAC was not strong enough to shield the convection

electric field effectively, Moreover, there were some departures from this aspect, mainly in the initial phases of the storms or the morning times, as seen in case 1 around 1200-1330 UT (0700-0830 LT). In this scenario, the EEF was enhanced when the asyH and asyD increased, suggesting that the EEF was

controlled by another factor, such as the ram pressure or dynamo effect. However, it is clear that increments in the EEF, which indicate the PPEFs, were very small in comparison with the enhanced asyH (R2 FACs).

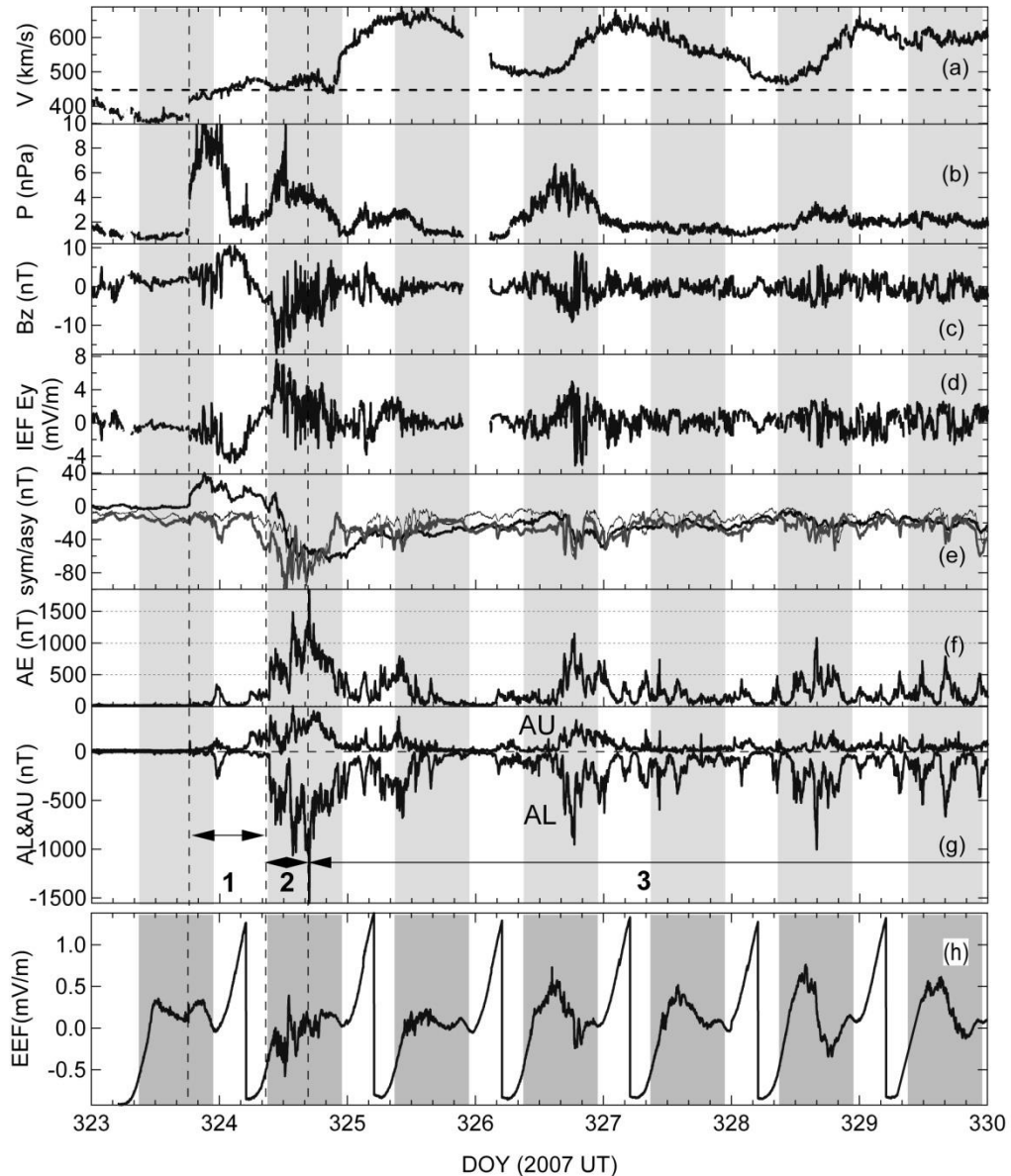


Figure 4 Multiple HILDCAA events from 19 to 26 November 2007. (a) Solar wind speed. (b) Solar wind ram pressure. (c) North/south magnetic field component. (d) Interplanetary electric field E_y component. (e) symH (thick black line) as well as the -asyH (thick gray line)/-asyD (thin black line). (f) AE index. (g) AL and AU. (g) Equatorial electric field. Horizontal dashed line indicates HSSs. Shaded areas represent daytime data.

Multiple HILDCAA event

An event as shown in Figure 4 was selected to study the variations of the PPEFs in the HILDCAA events in 2007. The requirements for the HILDCAA events are [23] (1) AE index should not range below 200 nT for more than 2 h, (2) AE should reach peaks over 1000 nT, and (3) it should occur outside the main phase of magnetic storms. In addition, the symH index is not less than -100 nT and there are HSS and high frequency fluctuations of IMF Bz about zero. As a result, this event exhibited a multiple HILDCAA event because there are two group of the AE index that exceeds 1000 nT.

Figure 4 showed that HSS comprised of three-subgroups that moved pass the ACE spacecraft. Each group corresponds to formation of the CIR with different sizes at the leading edge of each HSS. The dynamic pressure increased in the initial phase on DOY 323-324 then substantially decreased in the main and recovery phases of the storms. Numbers 1, 2, and 3 indicate the initial, main, and recovery phases of the storms, respectively. The IMF Bz/IEF Ey exhibited large fluctuations in the main phases of storms and substantial fluctuations in the recovery phase. The latter is associated with the Alfvén waves. The symH index, which is essentially the same as the Dst but with 1 min resolution, was positive in the initial phase which almost corresponded to the whole high pressure region in CIR. The asyH, asyD were high ~ 100 nT in the main phase and then decreased to ~ 40 nT in the recovery phase. The values of the asyH (the partial ring current) and asyD (strength of the R2 FAC) suggest that the R2 FAC still shield the convection electric field in the recovery phases.

The AU and AL indices simultaneously grew during the main and recovery phases with the peaks were 468 nT and -1553 nT, respectively. Note that the AL index mainly contributed to the AE index. Note that the AE index was high in the main phase when the IMF Bz largely fluctuated since the AE increases are caused by intermittent magnetic reconnection between

southward components of interplanetary Alfvén wave fluctuations and magnetopause magnetic fields [24]. It suggested that the convection electric field essentially penetrated to the polar ionosphere. PPEFs were allowed in the undershielding condition when rapid southward turning of the IMF Bz impinged on the magnetosphere. It should be noted in Figure 4 that the major contribution to the AE increases are AL decreases in the recovery phase. The AU index is a minor factor. This implies that HILDCAAs are due to westward electrojet intensifications [24] that satisfy the overshielding condition due to the sustained R2 FACs. The electrojets (DP2 current system), including a westward (AL) and an eastward electrojet (AU), significantly increased during the main phase. The DP2 current system could drive the AU and AL indices to a high level. As the HILDCAA event is not included in the main phase we found that the event started on DOY 326 and lasted more than 4 days. In addition, the AE is generally most intense near the leading edges of HSSs (where Alfvén waves have the largest amplitudes) and it decreases with decreasing wave amplitude.

The daytime EEF exhibited large variations, particularly during the main phase of storms. This indicated to the obvious PPEF in the equatorial ionosphere. It is interesting to note that the PPEFs were still being observed in many consecutive days during the recovery phase but with smaller amplitudes. The small amplitudes may deal with the R2 FACs that were active in recovery phase and deal with decreases in the IMF Bz that reduces the energy transfer to the magnetosphere. Despite ground based studies suggesting the development of the shielding (decrease in the intensity of the DP2 currents) during the end of the main phase despite the large negative southward IMF Bz [38] our results indicated that it can also happen in the recovery phase of the storm of the HILDCAA events.

Conclusions

The effects of RGSs on daytime penetration electric field to the equatorial ionosphere revealed striking and attractive results. Two case studies in 2007 suggested that PPEFs exhibited different characteristics depending on the transient effects in CIRs and HSSs. The RGSs cause PPEF mainly in the main phase of storms and not all the RGS exhibited penetration of electric field into the ionosphere. Particularly, PPEF was terminated in the main phase at shocks in association with the sudden depression of the solar wind pressure in CIRs. The turning of magnetic field B_z to the south in the main phase of the magnetic storms are associated with the PPEF and the fluctuations in IMF B_z are associated with transient PPEFs. Some HSSs cause High-Intensity Long-Duration Continuous AE Activity (HILDCAA) that can last for a few to 27 days. The major contribution to the AE increases are AL decreases due to westward electrojet intensifications in the HILDCAAs events that satisfy the overshielding condition. The values of the $asyH$ (the partial ring current) and $asyD$ (strength of the R2 FAC) suggest that the R2 FAC still shield the convection electric field in the recovery phases. The results may provide an important step to study the equatorial and low latitude ionospheric electrodynamics in the solar minimum conditions, in which the driving mechanism and penetration duration of the PPEF are crucial to be identified.

Acknowledgments

This work was supported by the National Astronomical Research Institute of Thailand (NARIT) under grant 08/2559. The author is grateful to the Jicamarca Radio Observatory for providing the vertical drift data. The Jicamarca Radio Observatory is a facility of the Instituto Geofisico del Peru operated with support from the NSF AGS-0905448 through Cornell University. The OMNI data were obtained from the GSFC/SPDF OMNIWeb interface at <http://omniweb.gsfc.nasa.gov>. The geomagnetic

activity data Dst are obtained from World Data Center for Geomagnetism, Kyoto University. The NOAA National Centers for Environmental Information (NCEI) geomagnetic calculator provide the geomagnetic field data. The ionospheric electric field data were partly prepared by Ponlawat Wannapan.

References

- [1] Nishida, A. 1968. "Coherence of geomagnetic DP 2 fluctuations with in-terplanetary magnetic variations". **J Geophys Res.** 73: 5549–5559.
- [2] Kikuchi, T., *et al.* 1996. "Direct penetration of the polar electric field to the equator during a DP 2 event as detected by the auroral and equatorial magnetometer chains and the EISCAT radar". **J Geophys Res.** 101:17161–17174.
- [3] Sastri, J. H. 2002. "Penetration electric fields at the nightside dip equator associated with the main impulse of the storm sudden commencement of 8 July 1991". **J Geophys Res.** 107: 1448-1158.
- [4] Kikuchi, T., *et al.* 2000. "Penetration of auroral electric fields to the equator during a substorm". **J Geophys Res.** 105: 23251–23262.
- [5] Kelley, M. C., *et al.* 2003. "Penetration of the solar wind electric field into the magnetosphere/ionosphere system". **Geophys. Res. Lett.** 30: 7–11.
- [6] Huang, C.-S., Foster, J. C., and Kelley, M. C. 2005. "Long-duration penetration of the interplanetary electric field to the low-latitude ionosphere during the main phase of magnetic storms". **J Geophys Res.** 110: A11309-A11318.
- [7] Spiro, R. W., Wolf, R. A., and Fejer, B. G. 1988. "Penetrating of high-latitude-electric-field effects

- to low latitudes during SUNDIAL 1984". **Ann Geophys.** 6: 39–49.
- [8] Abdu, M. A., Maruyama, T., Batista, I. S., Saito, S., and Nakamura, M. 2007. "Ionospheric responses to the October 2003 super-storm: Longitude/local time effects over equatorial low and middle latitudes". **J Geophys Res.** 112: A10306-A10315.
- [9] Manoj, C., Maus, S., Lühr, H., and Alken, P. 2008. "Penetration characteristics of the interplanetary electric field to the daytime equatorial ionosphere". **J Geophys Res.** 113: A12310.
- [10] Jaggi, R. K., and Wolf, R. A. 1973. "Self-consistent calculation of the motion of a sheet of ions in the magnetosphere". **J Geophys Res.** 78: 2852.
- [11] Kelley, M. C., Fejer, B. G., and Gonzales, C. A. 1979. "An explanation for anomalous equatorial ionospheric electric fields associated with a northward turning of the interplanetary magnetic field". **Geophys Res Lett.** 6: 301–304.
- [12] Senior, C., and Blanc, M. 1984. "On the control of magnetospheric convection by the spatial distribution of ionospheric conductivities". **J Geophys Res.** 89: 261–284.
- [13] Wolf, R. A., Spiro, R. W., Sazykin, S., and Toffoletto, F. R. 2007. "How the Earth's inner magnetosphere works: An evolving picture". **J Atm Sol Terr Phys.** 69: 288–302.
- [14] Peymirat, C., Richmond, A. D., and Koba, A. T. 2000. Electro-dynamic coupling of high and low latitudes: Simulations of shielding/overshielding effects **J Geophys Res.** 105: 22991– 23004.
- [15] Maruyama, N., *et al.* 2007. "Modeling storm-time electrodynamics of the low-latitude ionosphere thermosphere system: Can long lasting disturbance electric fields be accounted for?" **J Atm Sol Terr Phys.** 69: 1182–1199.
- [16] Fejer, B. G. 2011. "Low Latitude Ionospheric Electrodynamics". **Space Sci Rev.** 158: 145–166.
- [17] Wolf, R. A., *et al.* 1982. "Computer simulation of inner magnetospheric dynamics for the magnetic storm of July 29, 1977". **J Geophys Res.** 87: 5949–5962.
- [18] Yuan, Z., and Deng, X. 2007. "Effects of continuous solar wind pressure variations on the long-lasting penetration of the interplanetary electric field during southward interplanetary magnetic field". **Adv in Space Res.** 39: 1342–1346.
- [19] Zong, Q.-G., *et al.* 2010. "Dayside ionospheric response to the intense interplanetary shocks-solar wind discontinuities: Observations from the digisonde global ionospheric radio observatory". **J Geophys Res.** 115: A06304-A06310.
- [20] Fejer, B. G., *et al.* 1990. "Latitudinal variation of perturbation electric fields during magnetically disturbed periods -1986 Sundial observations and model results". **Ann Geophys.** 8: 441–454.
- [21] Wei, Y., *et al.* 2008. "Unusually long lasting multiple penetration of interplanetary electric field to equatorial ionosphere under oscillating IMF Bz". **Geophys. Res. Lett.** 35: L02102.
- [22] Tsurutani, B. T., *et al.* 1995. "Interplanetary origin of geomagnetic activity in the declining phase of the solar cycle". **J Geophys Res.** 100: 21717–21734.

- [23] Tsurutani, B. T. and Gonzalez, W. D. 1987. "The cause of high-intensity long-duration continuous AE activity (HILDCAAS) - Interplanetary Alfvén wave trains". **Plan Space Sci.** 35: 405-412.
- [24] Tsurutani, B. T., *et al.* 2004. "Are high-intensity long-duration continuous AE activity (HILDCAA) events substorm expansion events?" 2004. **J Atmos Sol Terr Phys.** 66: 167-176.
- [25] Kutiev, I., *et al.* 2013. "Solar activity impact on the Earth's upper atmosphere". **J Space Wea Space Clim.** 3: A06-A12.
- [26] Dmitriev, A. V., *et al.* 2013. "Longitudinal variations of positive dayside ionospheric storms related to recurrent geomagnetic storms". **J Geophys Res.** 118: 6806-6822.
- [27] Veenadhari, B., *et al.* 2012. "Corotating interaction region induced magnetic storms during solar minimum and their effects on low-latitude geomagnetic field and ionosphere". **Ind J of Radio & Space Phys.** 41: 306-315.
- [28] Anderson, D., *et al.* 2002. "Estimating daytime vertical ExB drift velocities in the equatorial F-region using ground-based magnetometer observations". **Geophys. Res. Lett.** 29: 37-41.
- [29] Anderson, D., *et al.* 2004. "Day-time vertical ExB drift velocities inferred from ground-based magnetometer observations at low latitudes". **Space Weather.** 2: S11001.
- [30] Anghel, A., *et al.* 2007. "Interplanetary electric fields and their relationship to low-latitude electric fields under disturbed conditions". **J Atmos Sol Terr Phys.** 69: 1147 - 1159.
- [31] Denardini, C., *et al.* 2011. "Daytime efficiency and characteristic time scale of interplanetary electric fields penetration to equatorial latitude ionosphere". **J Atmos Sol Terr Phys.** 73: 1555-1559.
- [32] Subhadra Devi, P. K., and Unnikrishnan, K. 2014. "Study of day-time vertical ExB drift velocities inferred from ground-based mag-760 netometer observations of ΔH , at low latitudes under geomagnetically disturbed conditions". **Adv Space Res.** 53: 752-762.
- [33] Yizengaw, E., *et al.* 2014. "The longitudinal variability of equatorial electrojet and vertical drift velocity in the african and american sectors". **Ann Geophys.** 32: 231-238.
- [34] Tsurutani, B. T., *et al.* 2008. "Prompt penetration electric fields and their ionospheric effects during the great magnetic storm of 3031 october 2003." **J Geophys Res.** 113: A05311.
- [35] Huang, C.-S., *et al.* 2007. "Penetration electric fields: Efficiency and characteristic time scale". **J Atmos Sol Terr Phys.** 69: 1135-1146.
- [36] Nicolls, M. J., *et al.* 2007. "The spectral properties of low latitude daytime electric fields inferred from magnetometer observations". **J Atmos Sol Terr Phys.** 69: 1160-1173.
- [37] Vasyliunas, V. M. 1970. **Particles and fields in the magnetosphere:** Proceedings of a symposium organized by the summer advanced study institute, calif. Dordrecht: Springer Netherlands.
- [38] Veenadhari, B. *et al.* 2010. "Penetration of magnetospheric electric fields to the equator and their effects on the low-latitude ionosphere during intense geomagnetic storms". **J Geophys Res.** 115: A03305.

Peer Instruction in Physics Recitation: A Case Study of Mechanics for Undergraduate Course

S. Tientongdee

General Science Program, Faculty of Education, Suan Sunandha Rajabhat University
Utong-Nok Rd., Dusit, Bangkok, 10300 Thailand

E-mail: sumalee.ti@ssru.ac.th

Abstract

This study was to study students' learning performance on mechanics recitation and to explore what students' opinions were toward mechanics recitation class as an undergraduate compulsory course taught by peer instruction. This case study was classroom research and quasi-experimental research design. The qualitative and quantitative research approach was used to collect the data in the fall semester of 2014 at University of North Texas, USA. Both descriptive and inferential statistics were used to analyze the quantitative data. Meanwhile, qualitative data were collected by conducting focus group and analyzed by using content analysis. The result showed that students' mechanics scores were statistically significant different between pre-test and post-test at 0.05 confident level. Their opinions were mostly positive toward class taught by peer instruction while comparing to tradition class.

Keywords: Peer instruction, Physics recitation

Introduction

According to Mazur (1997), Peer Instruction or PI is a pedagogical approach in which the instructor stops lecture periodically to pose a question to the students. These questions or Concept Tests are primarily multiple-choice, questions in which the answer options represent common student ideas and main concepts [7]. Peer instruction is considered as one of the primarily cooperative and interactive engagement teaching techniques. It was first used at the Harvard University in their large enrolment introductory physics courses teaching by Prof. Eric Mazur. Now it has been busing in many universities across the country especially now at University of Colorado at Boulder [2,6]. Most of educational research in PI was done mainly in physics and other subjects in STEM education [8].

Mostly common reports on PI researches have focused on measuring the improvement of students learning performance and problem solving skill [3]. In research literature relevant to PI also showed the impacts on three categories: impacts of PI on students' content knowledge, effects of PI on student peer discussion, effects of PI on problem solving skill. In this paper, however, it focused on students' learning performance and their opinions toward peer discussion and PI classroom. The process of using PI in class commonly consists of the following components [2,6,12].

Before class

Students are assigned to complete preparatory work or so called just in time teaching (often textbook reading, but this could include watching online lectures). The goal is to have students learn some of

the more basic items, concepts, or definitions before class, so that they do not have to be presented in class, thus creating time for student engagement more. To incentivize students to complete this work, a quiz or other assessment of some sort is given before each lecture.

During class

Students engage with questions designed to help them confront and also explore challenging concepts. Often these questions are posed as multiple-choice and students will gain credit for answering these questions with a clicker. Specifically, the algorithm of a clicker question epics in class should be:

A. Pose a question, students answer individually (generally, results not displayed for class).

B. Small group discussion (2-3 students) where students discuss their thinking and share their analyses with each other.

C. Students all answer a second time, perhaps changing their answer based on group discussion.

D. Class-wide discussion facilitated by the instructor is preferably led by first asking students to share the explanations and discussions they had in their group.

After class

The instructor provides clarification of how the question can be analyzed. The correct answer is clearly indicated.

Therefore in this study, the research used PI as a teaching technique to teach physics recitation by focusing on the hypothesis that it would help to improve student performance in mechanics. Also to explore what were their opinion toward PI and toward tradition class.

Materials and Methods

This study was used quasi-experimental research design [1]. The quantitative and qualitative data were collected to fulfill all phenomena in the

classrooms. Pre-test and post-test were given to one class as taught by PI for 50 students before and after fall semester of 2014 at University of North Texas. Other two classes taught by tradition or lecture and doing homework consisted of 50 and 60 students respectively but no pre-test and post-test given. To collect the quantitative data the test was selected from test bank of mastering-physics blackboard online program (instructor size). The problems were selected for 30 mechanic problems by using criteria as medium to high level difficulty identified in mastering physics program on blackboard. Students were asked to take the test for 30 minutes long before and after the semester in PI class. The class was taught as compulsory course but no grade. This recitation was mainly to help students improving their understanding on solving physics problems and to ask questions that they could not do in the main lecture. The steps of PI class were as following:

- 1) Students were divided into a group of 4-5 depending on where they sat in class.
- 2) The instructor explained main concept of the topic.
- 3) The instructor posted the physics question from low to high level of difficulty related to that topic.
- 4) Students were asked to think individually first and answered by showing the numbers of their fingers according to their best answer.
- 5) Students discussed and argued within their group on their answer.
- 6) Students then again answered the last time (they could change their answer if they were convinced by friends).
- 7) The instructor explained the solution on that problem.
- 8) If there were many questions on that problem, the instructor would give more problems.

In other two tradition classes, the main lectures were taught by giving main concept briefly and then solving homework problems on the blackboard. The instructor let students working by their own first and then showed them the solution. There was not much

of peer discussion happening like in PI class in these two classes.

For qualitative data collection, the focus group technique was used to an interview. The research selected 8 groups, 4 groups for each traditional class according to their learning achievement on mechanics test as low, medium, and high at the end of semester. Similarly, criteria were used to select 8 groups of students in PI class.

Data Analysis

There were two groups of data, quantitative and qualitative data. SPSS program version. 20 was used to analyze quantitative data. Descriptive statistics were reported and inferential statistic, paired-sample t-test, was used to test hypothesis on students' mechanics scores comparison from one group pre-test and post-test. Meanwhile to analyze qualitative data, the content analysis was used. The data were coded then grouping them in to category.

Results and Discussion

The results are divided into three main parts, first students' mechanics scores from pre-test and post-test. Secondly, it shows main students' opinions and the last one it shows some students' opinions on traditional classes.

Table 1 The comparison of students' mechanics scores

G	Pre		Post		P
	M	SD	M	SD	
1	16.90	4.92	23.64	4.49	.00
2	14.40	5.67	21.25	5.21	.00
3	18.22	4.77	24.06	4.52	.00

$P < 0.05$

According to Table 1, it shows that all groups 1-3 have shown significantly different between pre-test and post-test scores at 0.05 confident level. However,

group 1 which is PI group has shown the slightly higher scores on the post-test scores when compare with the pre-test among other groups.

Table 2 Students' opinion toward the class taught by PI

S	students' opinions	
	PI	
1	"It helps us to solve the problems faster by working with friends than working alone"	
2	"PI is useful for discussion and work together"	
3	"Less stress while working with friends and share what we know"	
4	"It's good but it should have more time for discussion and solve the problems"	
5	"PI is helping us to cooperate but if someone doesn't prepare to discuss, he will get lost"	
6	"It makes us see more on what we have done wrong when we argue and discuss within group and in class"	

From Table 2 after grouping 8 groups discussion into 6 items it shows that mostly students who were taught by PI think it is useful for them. Nevertheless, it shows some concerns on time consuming and among group members who do not prepare to discuss and to solve the problems.

Table 3 Students' opinions toward traditional class.

S	students' opinion
	tradition/lecture
1	<i>"It is very stress and difficult"</i>
2	<i>"Physics is hard, I like the lecture but don't like solving the problems"</i>
3	<i>"I can follow and solve the problems but not all"</i>
4	<i>"Lecture is fine, but I should prepare well before coming to the class to solve the problems"</i>
5	<i>"I am lost most of the time"</i>
6	<i>"We like how TA explain the solution but we can't solve the problem in the exam"</i>
7	<i>"The lecture should give us some more time to solve the problems"</i>

According to table 3 after coding the data and grouping all 8 groups discussion into 7 items, the results show that the students think traditional style or lecturing is fine, but the physics problems itself is hard. They feel very stress and have very hard time solving the problems. They need to more time to practice in class.

As shown in the results there are some similarity to prior research results for example as showed in Tolga Gok (2013) who studied students' performance and problem solving skills. In his study he focused on comparison of students' performance, skill and confidence with peer instruction and formal education for two-year college classroom. There were 98 students from two groups enrolled in a physics course in his study. The research results indicated that PI helped increasing students' performance and students' problem solving skills. The result of this study also repeated what Nathaniel Lasry, Eric Mazur, and

Jessica Watkins (2008) had found on their research that PI-taught students demonstrate better conceptual learning and similar problem-solving abilities than traditionally taught students. Also the result shows students positive opinion toward PI and peer discussion is the same as prior research conducted by Mark C. James (2006) but this study was done in electronic classroom.

One of the main limitations of this study was that it was only a small case study. To make higher impact on larger circumstance it should be repeated in the larger sample size. This was quasi-experimental design because of equality issue so if it can be experimental design that may give more accurate and reliable result. There are many research suggestions on trying PI in different subjects and areas. Therefore, in the future if the researchers want to use PI to improve students' performance, it can be in different circumstances such as in both high school level and higher education as well as in subject outside STEM.

Conclusions

This study was to compare students' performance from pre-test and post-test score on mechanics in PI recitation class. The result showed that there was a significantly difference between them at .05 confident level. It also focused on what students' opinions toward PI and toward traditional class. The results of this part indicated that their opinions were mostly positive toward PI class. They suggested that PI class needed more time for students to discuss and argue though. In addition, it helped students to share and learn more from each other. In the result of students' opinions on tradition or lecturing classes it showed that students felt more stress and thought physics was very hard for them which were not shown in PI class.

Acknowledgement

I would like to give special thanks to University of North Texas for giving me this opportunity to work with excellent students and also to all my wonderful students who were willing and participated in this study.

References

- [1] Campbell, D.T., and Stanley, J.C. (1963). *Experimental and quasi experimental designs for research: A handbook for research on interaction*. Boston, MA: Houghton Mifflin
- [2] Crouch, C.H., and Mazur, E. Peer instruction: Ten years of experience and results. *American J. of Physics* 69, 2001.
- [3] Freeman S, O' Connor E, Parks JW, Cunningham M, Hurley D, et al. Prescribed active learning increases performance in introductory biology. *CBE-Life Science Education*. 6:132-39. 2007.
- [4] Gok, T. "The impact of peer instruction on college students' beliefs about physics and conceptual learning and motivation. *Asia-Pacific Forum on Science Learning and Teaching*, 13(1), 1-17, 2012.
- [5] Gok, T. "A Comparison of Students' Performance, Skill and Confidence with Peer Instruction and Formal Education". *Journal of Baltic Science Education*, 12(6), 2013.
- [6] Lasry, N., Mazur, E., and Watkins, J. "Peer instruction: From Harvard to the two-year college", *Am. J. Phys.* 76(11), 1066-1069, 2008.
- [7] Mark, C.J. "The effect of grading incentive on student discourse in peer instruction". *Am. J. Phys.* 74, 689, 2006.
- [8] Mazur, E. *Peer Instruction: A User's Manual* (Prentice Hall, Upper Saddle River, NJ, 1997).
- [9] *Prepare and Inspire: K-12 Education in Science, Technology, Engineering, and Math (STEM) for America's Future*. Executive Office of the President, Washington, D.C., 2010.
- [10] Porter, L., Bailey-Lee, C. Siman, B., Zingaro, D. Peer instruction: Do Students Really Learn from Peer Discussion? *In Proc. 7th ICER*, 2011.
- [11] Smith, M.K., Wood, W.B., Adams, W.K., Wieman, C., Knight, J.K., Guild, N., and Su, T.T. "Why peer discussion improves student performance on in-class concept questions". *Science*, 323, 122-124, 2009.
- [12] Smith, M.K., Wood, W.B., Krauter, K., and Knight, J.K. "Combining peer discussion with instructor explanation increases learning from in-class concept questions. *CBE-Life Science Education*, 10, 55-63, 2011.
- [13] Turpen, C., and Finkelstein, N.D. "Not all interactive engagement is the same: Variations in physics professor' implementation of Peer Instruction". *Phys. Rev. ST Phys. Edu Res.* 5,020101 (2009).

Improving Hydrophobicity of Alumina Sheet Using Plasma Treatment

P. Champathet¹, S. Dangtip^{1,2*}, V. Ervithayasuporn³ and T. Osotchan^{1,2}

¹Department of Physics, Faculty of Science, Mahidol University, Bangkok 10400, Thailand

²NANOTEC Center of Excellence, Faculty of Science, Mahidol University, Bangkok 10400, Thailand

³Department of Chemistry, Faculty of Science, Mahidol University, Bangkok 10400, Thailand

*E-mail: somsak.dan@mahidol.edu

Abstract

Alumina operating in open field environment suffers harsher condition which may lead to lifetime shortening. Such problem can be remedied by improving the surface hydrophobicity. Coating hydrophobic layer can help prolonging the device lifetime. In this study, 25×25 mm alumina sheets were used as substrate. The alumina surface was activated using plasma treatment. The sheets were then spin-coated with UV-curable thiol-ene resin; consisting of (3-Mercaptopropyl)trimethoxysilane, Heptadecafluorodecyl methacrylate (HDFDMA), 2,4,6,8-tetramethyl-2,4,6,8-tetravinylcyclotetrasiloxane (TMTVSi), and Pentaerythritoltetrakis(3-mercaptopropionate) (PETMP). The hydrophobic TMTVSi and HDFDMA thin films were activated through Thiol-ene Click reaction. The wettability test of coated alumina was carried out. The contact angle analysis has shown that thin film between HDFDMA and PETMP to be hydrophobic with water contact angle greater than 120°.

Keywords: Plasma surface treatment, Hydrophobic, Alumina, Thiol-ene click reaction

Introduction

Alumina, as a very excellent insulator and dielectric, is useful in various applications, for example, in the electric circuit. The power grid and transport power line also utilize alumina as an electric insulator. For such application, glazing is applied for alumina finishing. The problem is in some area where the normal glaze cannot protect the electric insulator; resulting in reduction in the life time. Those are as typically include corrosive environments, such as on the coastal area. One way to get around this problem is coated with new layer of with superhydrophobicity. Hydrophobic can reduce the resident time of salty water droplet on alumina surface; thus reducing the interacting time or retaining the clean alumina surface. Two major approaches for enhancing superhydrophobic surface; one is to apply hydrophobic molecules

like fluoro-group on the surface by means of coating [7,8] and the other is to modify surface geometric texturing by means of creating micro- or nano-roughness as known as lotus effect or rose effect. The former approach may be achieved by chemical and physical deposition, for example, spray-deposition hydrophobic silica nanoparticles [1], and plasma polymerization combined with nanoparticles [5], and fluorinated polyhedral oligomeric silsesquioxanes [8]. However, this approach generally focuses to promote the strong bonding and hardness which may be achieved by using plasma surface treatment. The main effect plasma surface treatment is increase adhesive [3,6], receptiveness, and cleaning [4]. Plasma also consider as a green process as no chemical involved. Europe was starting to prefer this

method to the conventional cleaning and modification by chemical process [4].

Materials and Methods

Materials: Alumina sheet (Al_2O_3) substrates (of 96% purity) were purchased from Kyocera corporation, Japan. The alumina sheet was cut to have dimension of $25.0 \times 25.0 \times 0.635 \text{ mm}^3$. The substrates were ultrasonic-cleaned by in dish washing soap for 15 minute, acetone 15 minute, ethanol 15 minute, and water 15 minute. All of reagents were of research grade. (3-Mercaptopropyl)trimethoxysilane (MPTS), 2,4,6,8-tetramethyl-2,4,6,8-tetravinylcyclotetrasiloxane (TMTVSi), Pentaerythritoltetrakis(3-mercaptopropionate) (PETMP) and 2,2-dimethoxy-2-phenylacetophenone methacrylate (as photoinitiator) were obtained from Sigma-Aldrich. Heptadecafluorodecylmethacrylate (HDFDMA) was obtained from Wako Chemicals Japan.

Plasma Surface Treatment: The dielectric barrier discharge uses alternating current in RF frequency to generate plasma discharge between gaps of the electrode. The alumina surface was then treated by the dielectric barrier discharge plasma for 5 minute. The alumina sheet was placed on the center of the gap. The argon was fed at 1 litre/minute into the chamber prior to the process. The dielectric barrier discharge was conducted at RF power of 34 W. After plasma treatment the alumina sheet was then immediately transferred for further coating.

Film Preparation: (3-Mercaptopropyl) trimethoxysilane (MPTS), Heptadecafluorodecyl methacrylate (HDFDMA), 2,4,6,8-tetramethyl-2,4,6,8-tetravinylcyclotetrasiloxane (TMTVSi), and Pentaerythritoltetrakis(3-mercaptopropionate) (PETMP) Thiol-ene coating chemicals (MPTS, HDFDMA, TMTVSi and PETMP) were synthesized via thiol-ene click reaction by weighing alkene (TMTVSi, HDFDMA), thiol (MPTS, PETMP) into a brown bottle. The stoichiometric ratio of alkene to thiol was varied. For simple alkene and thiol functionalized such as HDFMA and

MPTS the ratio maintain at 1:1, in case of full-functionalized the ratio was 4:2:2:1 (MPTS:TMTVSi:HDFDMA:PETMP). Photoinitiator was then added 2% by weight. Acetone was selected as a solvent of the thiol-ene corrosion test and the ratio maintaining 15:1 to thiol-ene by weight. Coating material was mixed by ultrasonication for 30 minute. The films of functionalized thiol-ene were coated by spin-coating technique. The thickness of the thiol-ene films was varied through the rotation speed. For the range of rotation speed in this experiments were setting at 500-2000rpm. Time duration for spin-coating fixed at 30 sec. After spin-coated films on the alumina surface, the next process is photopolymerization (Thiol-ene click reaction). This process require UV light in spectrum 368 nm to create bonding between alkene and thiol group for 3 minute under the UV lamp, then annealing film at 45° for 2 hours in order to dry acetone from the sample.

Characterization: The measurements of static contact angle were measured by taking photograph of dropping A3 de-ionized water on 5 different positions (randomly chosen). ImageJ as plug-in drop analysis was use to analyze a contact angle from the picture. Volume of water in this method was 0.26 ml estimate from the programs. Paints and varnishes "Cross-cut test" was a method to characterize the adherence of the film to the substrates. ISO 2409:2013 was selecting as a standard method for this experiment. The result of cross-cut test can be obtained by counting part of films stuck on the tape after pulling from the surface. There are 6 classifications (0-5) of the resistance of paint coatings as following; Class (0) means the edges of the cuts are completely smooth; none of the squares of the lattice is detached. Class (1) means detachment of small flakes of the coating at the intersections of the cuts. A cross-cut is not greater than 5%. Class (2) means not greater than 15%. Class (3) means not greater than 35% and Class (4) means not greater than 65%, and Class (5) means anything more than 65%.

Results and Discussion

The first experiment conducted to study the effect of plasma surface treatment on the alumina sheets. MPTS solution was selected to coat on alumina to check uniformity. This layer was a buffer interface between the surface of alumina sheet and thiol-ene films.

The alumina sheet was grouped to two groups; no plasma treatment (normal group) and plasma-treated group. Figure 1a and 1b show the water contact angle of the MPTS film was spin-coated on normal alumina sheet. The water contact angle was increasing with increasing concentration of MPTS solution. Figure 1c and 1d show the water contact angle of the MPTS film spin-coated on plasma-treated alumina sheet. MPTS film on plasma surface treatment gives slightly higher contact angle of water for the same concentration in comparison of the normal (control) group. Furthermore MPTS films on plasma-treated alumina shows less deviation; indicating smoother film.

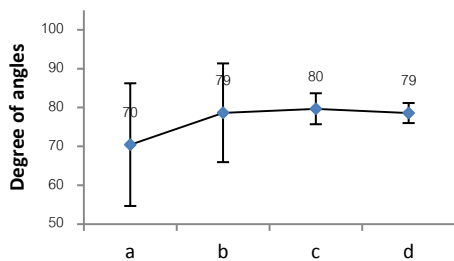


Figure 1 Water contact angle of MPTS films on non-plasma surface treatment at concentration of (a) 0.5 mol, (b) 1 mol and on plasma surface treatment of (c) 0.5mol (d) 1mol.

The next experiment was to investigate the effect of the films thickness. The coating solutions were HDFDMA+MPTS as the first simple layer of thiol-ene films and PETMP+TMTVSi+HDFDMA+MPTS films as more complex crosslink thiol-ene films. Both solutions were coating on alumina sheet in the same concentration.

Figure 2 shows the water contact angle of HDFDMA+MPTS film on alumina sheet. The coatings were done with two methods; dripping (Figure 2a) and spin-coating (Figure 2b-2e). In this case, plasma treated film has given a comparable effect on contact angle but slightly better uniform films than the drip coated ones; which agree with the before mentioned experiment. The plasma treated films was then studied for their thickness correlation by varying speed in spin-coating, as shown in Figure 2b-2e. There is no significant different in contact angel. Similar effects were also observed in the case of PETMP+TMTVSi+HDFDMA+MPTS film as shown in Figure 3.

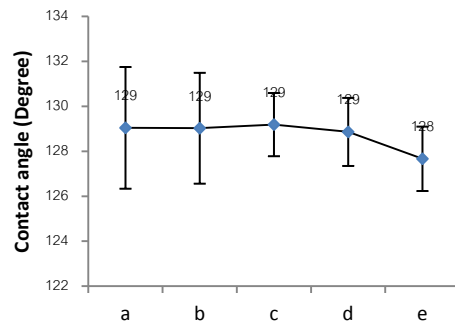


Figure 2 Water contact angle on HDFDMA+MPTS films. (a) Plasma surface treatment drip coated, Plasma surface spin-coated with different rotational speed (b) 500 rpm (c) 800rpm (d) 1000 rpm (e) 1500 rpm

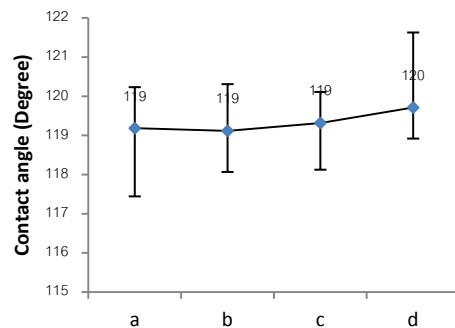


Figure 3 Water contact angle on PETMP+TMTVSi+HDFDMA+MPTS films. (a) Plasma surface treatment drip coated, Plasma surface spin-coated with different rotational speed (b) 1000 rpm (c) 1500rpm (d) 2000 rpm

Due to a rather complex compositions or chemicals, an investigation of different composition was also carried out. Figure 4 compares the water contact angle of films with of different composition with respect to the bare alumina. The highest contact angle of water was HDFDMA+MPTS films following by PETMP+TMTVSi+HDFDMA+MPTS films.

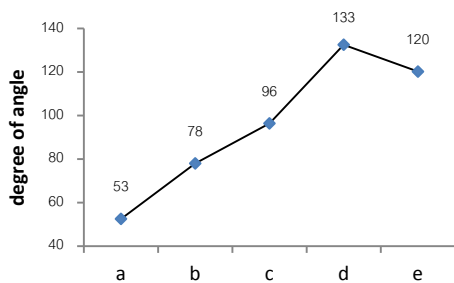


Figure 4 Contact angle on (a) bare alumina sheet, alumina sheet coated with (b) MPTS film, (c) TMTVSi+MPTS film, (d) HDFDMA+MPTS film, and (e) PETMP+TMTVSi+HDFDMA+MPTS film.

The last experiment about contact angle is the solvent resistivity. This experiment was conducting to simulation the corrosive environments in order to determined capability to withstand those conditions for use real situation.

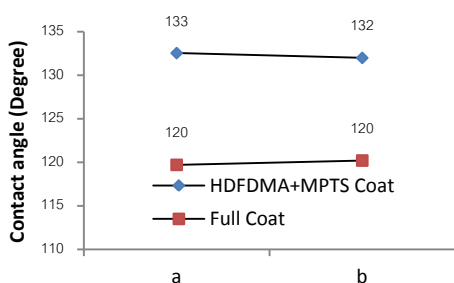


Figure 5 Water contact angle on alumina coated with HDFDMA+MPTS and PETMP+TMTVSi +HDFDMA+MPTS (a) before and (b) after soaking in acetone for 30 minute.

Another test on films resistance to corrosion, the alumina sheets with coating were left soaking in

acetone for 30 minutes before carrying contact angle measurement. Two types of film compositions were tested, i.e., HDFDMA+MPTS and PETMP+TMTVSi +HDFDMA+MPTS. Figure 5 shows the results. Water contact angle on both films have not changed after the test; indicating their excellent for anti-corrosive environment.

Another test on film bonding strength and hardness was measured by "Paints and varnishes Cross-cut test" with ISO 2409:2013 and using multi-blade cutting tool. The result was summarized in Table 1. HDFDMA+MPTS films was the lowest bonding strength with class 4 due to it has only one MPTS molecule to form a bonding with alumina surface, in the other hand TMTVSi+MPTS and PETMP+TMTVSi+HDFDMA+MPTS showed similar higher strength with Class 0.

Table 1 Comparison of bonding strength of three films compositions.

Films	Tools	Classification
TMTVSi+MPTS	multi-blade cutting tool	0
HDFDMA+MPTS	multi-blade cutting tool	4
PETMP+TMTVSi+HDFDMA+MPTS	multi-blade cutting tool	0

Conclusion

Plasma surface treatment plays the important rule in active surface receptiveness, increases adhesive between alumina surface and MPTS-layer and uniformness of the film. Another advantage of plasma treatment is the contact angle of plasma treated surface varies very little on concentrate. Plasma treated surface has given higher contact angle than the untreated surface. HDFDMA+MPTS offers the highest water contact angle; while the MPTS:TMTVSi:HDFDMA:PETMP give hydrophobic film with lower water contact angle but offer good resistivity. From these properties, MPTS:TMTVSi:HDFDMA:PETMP films was the most proper choice to coat on alumina insulator.

Acknowledgments

One of the authors(PC) would like to thank NANOTEC Center of Excellence, Faculty of Science, Mahidol University for financial and material support.

References

- [1] Bradley, J. S., Ethan F. T., Li X, James T. G., and Derek L. P. 2013. "Superhydrophobic Hybrid Inorganic–Organic Thiol-ene Surfaces Fabricated via Spray-Deposition and Photopolymerization". **ACS Appl. Mater. Interfaces**,5 (5), pp 1811–1817.
- [2] Alexander, K., Tucker, S., Richard, A. F., and Robin, L. G. 2011. "Thiol–ene Click Reaction as a General Route to Functional Trialkoxysilanes for Surface Coating Applications". **J. Am. Chem. Soc.**,133 (29);pp 11026-11029.
- [3] Ju, D. L., Pui M. L., Danniell M. W. R., Kam C. L., Zhong C. 2015. "Effect of surface treatment on adhesion strength between magnetron sputtered copper thin films and alumina substrate". **Applied Surface Science**.355, pp 509-551.
- [4] Lecia, B., Anna, Z., Dusan, K., Dusan, K., Miroslav, Z., Matej, M., and Mirko, C. 2015. "Atmospheric pressure plasma treatment of flat aluminum surface". **Applied Surface Science**. 355, pp 79-86.
- [5] Anna K., Artem S, Ondrej K, Martin P, Jir K., Pavel S., and Hynek B. 2014. "From super-hydrophilic to super hydrophobic surfaces using plasma polymerization combined with gas aggregation source of nanoparticles". **Vacuum**.110,pp 58-61.
- [6] Dick, H., Herwing, B., Christian, O. 2003. "Plasma treatment of polymers for surface and adhesion improvement". **Nuclear Instruments and Methods in Physics Research**.208, ppt 281-286.
- [7] Jianwei, X., Xu, L., Ching, M. C., Cher, L. T., Lu, S., Khine, Y. M., Xuehong, L., and Chaobin, H. 2009. "Polyhedral oligomeric silsesquioxanes tethered with perfluoroalkylthioether corner

groups: Facile synthesis and enhancement of hydrophobicity of their polymer blends". **Journal of Materials Chemistry**.19, pp 4740-4745.

- [8] Hongxia, W., Yuhua, X., Jie, D., Lianfang, F., Xungai, W., and Tong, L. 2009. "Durable, Self-Healing Superhydrophobic and Superoleophobic Surfaces from Fluorinated-Decyl Polyhedral Oligomeric Silsesquioxane and Hydrolyzed Fluorinated Alkyl Silane". **Angew. Chem. Int.**50, ppt 11433–11436.